CWP-676
October 2010

"Virtual source" methods for diffusive fields

Yuanzhong Fan

Applications of interferometry and synthetic aperture to controlled source electromagnetics (CSEM)

— Doctoral Thesis —
Geophysics

Defended on October 22, 2010

Committee Chair:	Committee members:
Dr. David Wu	Dr. Paul Sava
Advisor:	Dr. André Revil
Dr. Roel Snieder	Dr. James MacNeil
	Dr. Tim Ohno

Center for Wave Phenomena
Colorado School of Mines
Golden, Colorado 80401
(1) 303 384-2178

Abstract

The phrase *virtual source* refers to two different techniques in this dissertation. In the first half of the dissertation, it refers to *interferometry* and in the second half it uses the concept of the synthetic aperture technique. In interferometry, a receiver is converted to a "virtual source". In the synthetic aperture technique, a large "virtual source" is constructed by adding small sources.

Interferometry has been popularly used in the seismology community since the beginning of this century. The wave propagation between two receivers can be reconstructed by cross correlating the wave fields excited by uncorrelated sources on a closed surface surrounding two receivers, providing the medium is enclosed by sources. Cross-correlation interferometry is also proven to be applicable to diffusive fields. In this thesis, I pursue the application of interferometry to low frequency diffusive electromagnetic fields used in Controlled Source Electromagnetics (CSEM). For such diffusive fields, interferometry requires a volume distribution of sources to reconstruct the diffusion response between receivers. In practice, finding the optimal distribution of sources for interferometry is critical because there are only a finite number of sources. I study the required source distribution in cross-correlation interferometry for both wave propagation and diffusion. Although it is possible to apply interferometry to diffusive fields using a finite number of sources, sources close to the receivers have the largest contribution in the reconstruction. Therefore, there is no obvious advantage to apply interferometry to diffusive fields.

I also investigate the feasibility of applying multi-dimensional-deconvolution interferometry to low frequency diffusive electromagnetic fields. I show that the imprint of reservoirs significantly increases after applying multi-dimensional-deconvolution interferometry

to CSEM data. Although it does not require sources throughout the volume, this new approach of interferometry requires densely distributed receivers. The receiver spacing used in actual CSEM surveys is far sparser than what I used in the numerical example. To reduce the required sampling of receivers, I introduce the synthetic aperture concept to CSEM survey. The basic idea is that a large synthetic aperture source can be constructed by adding small sources. In the context of this dissertation, I use the synthetic aperture source as the second type of "virtual source". With a large synthetic source, I increase the required receiver spacing in the inline direction for multi-dimensional-deconvolution interferometry from 50 m to 1 km, which is a realistic receiver spacing. The synthetic aperture construction in the crossline direction needs further investigation.

Although the synthetic aperture concept has been popularly used for waves, it is the first time this technique is used for diffusive fields. I investigate the feasibility of steering and focusing diffusive fields. The similarities between diffusion and wave propagation allows one to steer and focus diffusive fields both in the frequency domain and time domain. The detectability of reservoirs using CSEM has significantly increased when the diffusive electromagnetic fields are steered. I analyzed the mechanism of the increased reservoir imprint in measured fields and show that the detectability of hydrocarbon reservoirs increases by both numerical and field data. Based on the increased detectability, I also propose new acquisition systems for CSEM. These new acquisition systems reduce the cost of CSEM surveys and provide more receiver positions, which can also help applications of multi-dimensional-deconvolution interferometry to CSEM data. The vertical dipole source is more sensitive the presence of horizontal extended reservoirs. The implementation of a vertical source, however, is challenging in field experiments. Using the concept of synthetic aperture, I show that the radiation pattern of a vertical source can be obtained by synthetically adding orthogonal dipole pairs.

Table of Contents

Abstract i

Acknowledgments vii

Chapter 1 Introduction 1

Chapter 2 Required source distribution for interferometry of waves and diffusive fields 7

2.1 Summary 7

2.2 Introduction 8

2.3 Model and Results 11

2.3.1 Waves in Homogeneous Media 11

2.3.2 Waves in Heterogeneous Media 24

2.3.3 Diffusion 26

2.4 Discussion 31

2.4.1 Waves in Homogeneous Media 31

2.4.2 Waves in Heterogeneous Media 38

2.4.3 Diffusion 43

2.5 Conclusion 47

Chapter 3 3-D Controlled Source Electromagnetic (CSEM) interferometry by multidimensional deconvolution 49

3.1 Summary 49

3.2 Basic Theory and History of Virtual Source Technique 49

3.3 Why Apply Interferometry in Marine CSEM? 54
3.4 Synthetic Example for a 3-D Reservoir in Shallow Water 56
3.5 Reducing the Required Receiver Spacing Using Synthetic Aperture 63
3.6 Discussion and Conclusions 70

Chapter 4 Can diffusive fields be steered and focused? 73
4.1 Summary 73
4.2 Introduction 73
4.3 Similarities Between Diffusion and Waves 74
4.4 Numerical Examples 75
4.4.1 Frequency Domain 76
4.4.2 Time Domain 79
4.5 Conclusion 81

Chapter 5 Increasing the sensitivity of controlled source electromagnetics with synthetic aperture 83
5.1 Summary 83
5.2 Introduction 84
5.3 Field Steering 86
5.3.1 Shallow Target 89
5.3.2 Deep Target 95
5.3.3 Shallow Sources and Ocean Bottom Receivers 97
5.3.4 Shallow Sources and Receivers 100
5.3.5 Real Data Example 102
5.4 Synthetic Vertical Source 104
5.5 Discussion and Conclusion 111

Chapter 6 Discussion and future work 113

6.1 Summary of Improvements in CSEM when Using the "Virtual Source" Techniques. 113
6.2 Key Contributions of This Dissertation to Interferometry and Controlled Source Electromagnetics 115
6.3 Future Work and Suggestions 116

References 119

Acknowledgments

This thesis and my Ph.D. study would not have been possible without the support from the following people.

It is difficult to overstate my gratitude to my advisor Prof. Roel Snieder. With his enthusiasm, his inspiration, his encouragement, his guidance and his personal examples, he taught me not only interferometry and CSEM but also how to be an independent researcher and communicator. He is a great advisor, a supportive colleague and a good friend in my life. There are so many unforgettable memories which make it hard to imagine having a better advisor and mentor for my Ph.D. study. Here are some examples. In the first week of my study in CWP, Roel told me a same three-minute-long joke three times. Once was in the restroom. I thought this was really a fun professor to work with. He insisted for me to call him Roel instead of "Sir." It makes it possible that one day I can think of him as my colleague instead of "my boss." This really helps a student like me from an Asian country. In the first semester, it drove me crazy when he kept asking me "what are the questions?" every time during our weekly meeting. He always says "If you ask the right questions, you know the answers." His insistence made me understand how important asking questions is to become a researcher who can find new research directions and define projects. I still remember how excited Roel was when I disagreed with him in research for the first time. He said "Fan, this is a moment that you are becoming an independent researcher." I had many trips with Roel and every trip was a fun and a learning experience for me. He introduced me to so many wonderful people who later became my colleagues and friends. His continuous encouragement has realized many of my potentials which I didn't have. He was the first who told me "Fan, you are really a good presenter." That encouragement made me able

to present my research in front of a large audience comfortably today. He was the first one who told me "You are really good at working with people." Because of that, I started to explore how to better work with other colleagues and got involved more in social events in the department. I also appreciate the positive criticism he gave when I really need them. For a period of time, I was kind of lazy and did not concentrate on my research. During our weekly meeting, Roel told me "Fan, I understand you have many things on your plate, but you are not moving very fast in the research." Without that reminder, I could have not finished my research within four years. There are just too many things I would like to share here but it will make my thesis non-technical. Thanks Roel for being my advisor, great colleague and dear friend.

There are many other individuals I would like to thank. Without them, I could have never made the progress in my research and finished this thesis. The collaboration with my colleagues Evert Slob, Jürg Hunziker and Kees Wapenaar from TUDelft, the Netherlands is such a wonderful experience both on the research and personal level. During my stay in TUDelft and the collaboration after that, they are extremely supportive and provided me with many suggestions in research.

Johannes Singer, Jon Sheiman and Kurang Mehta from Shell guided my research during my two summer internships with Shell. Most examples in this thesis were produced in these two internships. Johannes was my advisor during the internships. He had so many new research ideas which inspired much progress in my research. He also helped me to extend my geophysics experience by taking me away from my computer to the field. He also took me to many delicious restaurants in Houston, which made my stay in Houston so enjoyable. Jon Sheiman was a super busy person in Shell, but he managed to have weekly meetings with me during my internships. It always took me one week to realize what great suggestions he gave. Kurang Mehta, a former CWP student who works in Shell, always dropped by my desk and discussed my research. He worked in a different research group, but he came to my desk almost every day. The EM team in Shell provided me extreme support during my Ph.D.

study and my internships. Mark Rosenquist, Liam O Suilleabhain and Jeffrey Johnson patiently explained to me what CSEM was when I was new in this field and taught me how to use CSEM modeling code. All the numerical examples on CSEM in this dissertation were produced by their modeling code. The EM team in Shell allowed me work on my thesis project while I was interning in their group. They also provided me the field data in Chapter 5. I would also like to thank the Shell GameChanger Program for providing research funding over the last four years. Our contact person in GameChanger, Lori Glassgold Gibson, was always supportive in our research. She organized a two-day workshop on synthetic aperture CSEM after my second internship. That workshop generated many new research projects, which also led to a new GameChanger project with Shell. Most of the progress in my research did not happen when I sat in front of my computer but during the conversations with these colleagues.

I feel very lucky to be a student in the Geophysics Department in CSM. The faculty and staff in the department were very supportive during my study. I thank Dr. Terry Young for the continuous support and advice in my Ph.D. study. His door was always open to students and I found it was helpful and comfortable every time I walked out of his office. I thank Michelle Szobody and Dawn Umpleby for their support during my study. Without them my study in this department would not be as smooth and enjoyable as it was. The Geophysics faculty are not only excellent in their own specialty, but also are very open to advise students from different groups and provide great suggestions. Special thanks to Prof. Misac N. Nabighian for introducing various geophysical techniques to me. I really thank the CWP faculty for their support and training over the last few years. I took my first seismology class from Prof. Ilya Tsvankin and learned the real world was anisotropic. Prof. Paul Sava taught me what seismic migration was so that I started to understand seismic seminars. I learned that signal processing can be so fun and the efficiency can be achieved by simple math after I took Prof. Dave Hale's class. I thank Dr. Norm Bleistein and Dr. Ken Larner for the support and training on oral presentations during our sponsor meetings.

I still remember I almost fainted when I did a public presentation during my Master's study in Canada. The CWP training made me confident to give talks in front of large audience. I would like to thank Barbara McLenon and Pam Kraus for their support during my study in CWP and for making the office so joyful. Barbara was the best 'student' in our writing workshops and she helped me a lot in English writing. Pam could get any paperwork done faster than you could imagine. John Stockwell taught me mathematics that I should have known in his math clinic. He also helped me to start using Linux machines. I normally took the same bus with John in the morning and always enjoyed the Captain Cook stories from a history book he was reading. I really appreciate CWP for providing students help in English writing, especially for us international students. It was a great learning experience working with Diane Witters. She not only taught me what should be the correct way to write English, but also encouraged me to recognize my own mistakes in writing. In this way, I had a better manuscript and also really learned how to improve my writing. It was always fun to discuss the mysterious articles "a, an, the" with her. I thank all my fellow CWP and geophysics students for their encouragement and help during my study. I cannot list everyone's name here because there are so many. They helped me in my courses, gave suggestions on my presentations, proofread my manuscripts and had a lot of fun with me. I am grateful to know so many intelligent students in this department.

I would like to thank my committee for their continuous support and advice over the last four years. Prof. Paul Sava, Prof. André Revil and Prof. David Wu have supported me from my first comprehensive project to my Ph.D. thesis. Prof. John Scales served on my committee for my first comprehensive project. The discussion with him made my Chapter 1 much stronger than its earlier version. I thank Prof. James MacNeil for serving on my committee before his retirement. Special thanks to Prof. Tim Ohno for agreeing to be on my committee on such short notice.

During the last four years, my brothers and sisters in CCAID Chinese Christian Church continuously support my family. I thank my American friendship family, Helen and Hale

Lees, for their love and care. I had my unforgettable Christmas Eve with their family. They gave us great support when my daughter was born ten months ago.

Last but not the least, I want to thank my family for their unconditional love and support over my Ph.D. study and all previous school years. My parents always gave me comfort and encouragement every time I called them. My little brother never doubted his brother's ability to finish the Ph.D. study. I am so grateful for my wife Jing Zhang. Her gentleness and love gave me strength and peace to concentrate on my research and study. When I made progress at school, she was the one who was happier than I was. When I struggled in my study, she encouraged me and believed in me. She taught me how to communicate with other people. She taught me how to see other people's strength. Without her love and company, I would never have been able to finish my Ph.D. and become the person I am today. My beloved daughter Jessica Fan, thanks for being such a kind baby to let your Dad sleep at night. One magic smile from her can sweep away all my stress and tiredness from school. She gave me unlimited strength to finish my thesis in this time frame.

I am not a very intelligent person. The only reason that I can finish my Ph.D. is because I am surrounded by these wonderful people. Because of them, 2006 to 2010 have been the best four years I have ever had in my life.

Chapter 1

Introduction

The "*virtual source*" method has been used in exploration seismic community to find the seismic response between receivers (Bakulin & Calvert, 2004; Calvert *et al.*, 2004; Bakulin & Calvert, 2006; Mehta *et al.*, 2007). In a more general sense, it is also referred to as *seismic interferometry* (Wapenaar, 2004; Snieder, 2004, 2007; Wapenaar *et al.*, 2005; Campillo & Paul, 2003; Shapiro *et al.*, 2005) and *Green's function reconstruction* (Lobkis & Weaver, 2001; Weaver & Lobkis, 2001; Malcolm *et al.*, 2004). In this dissertation I use these three phrases interchangeably. The fundamental concept of interferometry is the following: the wave propagation between two receivers can be reconstructed by cross-correlating received wavefields at these two locations, providing that the two receivers are enclosed by uncorrelated sources. The reconstructed wavefield is equivalent to the received wavefield at one receiver as if the other receiver became a source. In this way, a receiver is converted to a virtual source. The history of interferometry, applications to various physical science and more complete reference work are presented in the introduction sections of Chapter 2 and Chapter 3.

There are many advantages to use a virtual source. Because it is easier to place a receiver in the subsurface than to locate an active source, the virtual source is able to illuminate targets that are difficult to image with active sources. Beside, the complex overburden above the receivers can be removed by using seismic interferometry. Interferometry also has the ability to create passive imaging without using an active source. These advantages

of using interferometry has inspired research on both seismic interferometry theory and its applications for the last ten years. For example, media in which interferometry can be applied are extended from lossless and time invariant to more general media (Godin, 2006; Wapenaar, 2006b; Wapenaar *et al.*, 2006; Snieder *et al.*, 2007; Weaver, 2008).. More mathematical operators are available to use in interferometry besides cross-correlation, such as deconvolution (Snieder & Şafak, 2006; Vasconcelos & Snieder, 2008a,b), multi-dimensional deconvolution (Wapenaar *et al.*, 2008) and cross-coherence.

One extension of interferometry theory is its application to diffusive fields by Snieder (2006b). The application of interferometry to diffusive fields allows one to create diffusive virtual sources. One important diffusive field in exploration geophysics is the low frequency electromagnetic fields in the conductive subsurface used by Controlled Source Electromagnetics (CSEM). CSEM provides the resistivity of the subsurface and therefore it is useful to distinguish the content of fluids in porous rocks (e.g. oil and brine). Although the theory of diffusion interferometry of Snieder (2006b) is interesting, the source distribution for applying interferometry in diffusive fields is unpractical. Instead of sources on a closed surface that are required for seismic interferometry, diffusion interferometry requires to have sources throughout the volume. In other words, one needs sources everywhere to apply interferometry to diffusive fields.

In Chapter 2, I describe the required source distribution in cross-correlation interferometry for both wave propagation and diffusion. Although interferometry for wave propagation has been intensely used, the required source distribution is not always fulfilled. This leads to the spurious events in the reconstructed wavefields. I observe that the angle distribution of sources is a critical parameter in Green's function reconstruction. I also find that for strongly heterogeneous media, the common belief that one single source is sufficient to reconstruct the full Green's function is not correct. In fact, a denser source distribution is required to apply interferometry in strongly heterogeneous media than for homogeneous media. For diffusion, I find that it is possible to use a finite number of sources

to apply interferometry. Sources close to the receivers, however, are crucial in the Green's function reconstruction for diffusive fields. This source distribution requirement makes it unattractive to apply cross-correlation interferometry to diffusive fields. The purpose of the interferometry technique is to use a receiver as a virtual source. If real sources close to the receivers are required to do this, then one could just as well place a physical source at the receiver position.

Later, Wapenaar *et al.* (2008) showed another approach of interferometry using multi-dimensional deconvolution. This approach of interferometry is applicable to both wave propagation and diffusion. Unlike the cross-correlation interferometry, the source distribution is less important but the receiver distribution in multi-dimensional-deconvolution interferometry is critical. Wapenaar *et al.* (2008) show a 2-D synthetic example of using multi-dimensional-deconvolution interferometry in diffusive electromagnetic fields. The detailed description of multi-dimensional-deconvolution interferometry is presented in Chapter 3. I studied the feasibility of applying this new approach of interferometry to 3-D diffusive fields and have applied it to a synthetic 3-D CSEM survey. The imprint of reservoirs has been significantly increased when interferometry is used. However, the required receiver distribution in my numerical example is unrealistic. A 2-D receiver array with a receiver spacing of 50 m is required while in a real survey there is normally only one line of receivers with a spacing of 1 km. In order to solve this requirement of a dense 2-D receiver array, I introduce the synthetic aperture concept at the end of chapter 3. It shows that the receiver spacing can be extended to 1 km with a constructed large synthetic source.

The synthetic aperture technique, as described in Chapters 4 and 5, is a wave-based concept and has been widely used in radar and sonar community (Barber, 1985; Ralston *et al.*, 2007; Zhou *et al.*, 2009; Cutrona, 1975; Riyait *et al.*, 1995; Bellettini & Pinto, 2002). However, the use of this technique in diffusive fields is new. So the question is: can one apply the synthetic aperture technique to diffusive fields? In particular, I studied steering and focusing of diffusive electromagnetic fields. In Chapter 4, I use the similarities of wave

propagation and diffusion to show that diffusive fields can indeed be steered and focused both in the frequency domain and the time domain.

Applying synthetic aperture to diffusive fields has potential of opening new research in various fields such as subsurface exploration using low frequency electromagnetics, submarine communications and medical imaging using diffusive light. In this dissertation, I concentrate on applications of the synthetic aperture technique to CSEM surveys. In Chapter 5 I show that the detectability of hydrocarbon reservoirs significantly increases by applying field steering on both numerical examples and field data. Consequently, deeper reservoirs are visible to CSEM and better acquisition systems become applicable. I also investigate the synthetic vertical source in Chapter 5. A similar radiation pattern of a vertical dipole source can be constructed by adding orthogonal horizontal dipole pairs. This new radiation pattern is more sensitive to the subsurface reservoirs than that from a traditional horizontal dipole.

The work in this dissertation yields the following publications:

Chapter 2:

Fan, Y. and R. Snieder, 2009, Required source distribution for interferometry of waves and diffusive fields: *Geophys. J. Int.*, **179**, 1232-1244.

Chapter 3:

Fan, Y., R. Snieder, E. Slob, J. Hunziker and J. Singer, 2010, 3-D controlled source electromagnetic (CSEM) interferometry by multi-dimensional deconvolution: to be submitted to *Geophysics*.

Chapter 4:

Fan, Y., R. Snieder, E. Slob, J. Hunziker, and J. Singer, 2010, Can diffusive fields be steered and focused? : *Phys. Rev. Lett.*, in revision.

Chapter 5:

Fan, Y., R. Snieder, E. Slob, J. Hunziker, J. Singer, J. Sheiman and M. Rosenquist, 2010, Synthetic aperture controlled source electromagnetics: *Geophys. Res. Lett.*, **37**, L13305.

Fan, Y., R. Snieder, E. Slob, J. Hunziker, J. Singer, J. Sheiman and M. Rosenquist, 2010, Increasing the sensitivity of controlled source electromagnetics with synthetic aperture: to be submitted to *Geophysics*.

Besides the publications above, I contributed to other research as shown below.

Snieder, R. and Fan, Y. and Slob, E. and Wapenaar, K., 2010, Equipartitioning is not sufficient for Green's function extraction: *Earthquake Science*, in press

Hunziker, J., Fan, Y., Slob, E., Wapenaar, K., and Snieder, R., 2010, Solving Spatial Sampling Problems in 2D-CSEM Interferometry using Elongated Sources, 72nd EAGE annual meeting, Barcelona, Spain.

Hunziker, J., van der Neut, J., Slob, E., Wapenaar, K., Fan Y., and Snieder, R., 2010, Controlled Source Electromagnetic interferometry: the point spread function: 80 SEG annual meeting, Denver, USA

Hunziker, J., Slob, E., Fan, Y., Snieder, R. and Wapenaar, K., 2010, Two-dimensional Controlled-Source Electromagnetic Interferometry by multidimensional deconvolution: spatial sampling aspects: *Geophysical Prospecting* (submitted)

Hunziker, J., Slob, E., Fan, Y., Snieder, R. and Wapenaar, K., 2010, Time-lapse Controlled Source Electromagnetics using interferometry: *The Leading Edge* to be submitted

Chapter 2

Required source distribution for interferometry of waves and diffusive fields

2.1 Summary

The Green's function that describes wave propagation between two receivers can be reconstructed by cross-correlation provided that the receivers are surrounded by sources on a closed surface. This technique is referred to as "interferometry" in exploration seismology. The same technique for Green's function extraction can be applied to the solution of the diffusion equation if there are sources throughout in the volume. In practice, one has only a finite number of active sources. The issues of the required source distribution is investigated, as is the feasibility of reconstructing the Green's function of the diffusion equation using a limited number of sources within a finite volume. We study these questions for homogeneous and heterogeneous media for wave propagation and homogeneous media for diffusion using numerical simulations. These simulations show that for the used model, the angular distribution of sources is critical in wave problems in homogeneous media. In heterogeneous media, the position and size of the heterogeneous area with respect to the sources determine the required source distribution. For diffusion, the sensitivity to the sources decays from the midpoint between the two receivers. The required width of the source distribution decreases with frequency, with the result that the required source distribution for early-time and late-time reconstruction is different. The derived source distribution criterion for diffusion suggests that the cross-correlation-based interferometry

is difficult to apply in field condition.

2.2 Introduction

The term interferometry generally refers to the study of the interference of two signals as a measure of the difference between them (Curtis *et al.*, 2006). The term also refers to the technique used in seismology to extract the response which describes the wave propagating between two receivers, as if one of the receivers were an active source (Lobkis & Weaver, 2001; Derode *et al.*, 2003; Weaver & Lobkis, 2004; Wapenaar, 2004; Snieder, 2004, 2007; Wapenaar *et al.*, 2005). This technique has been applied in ultrasound (Weaver & Lobkis, 2001; Malcolm *et al.*, 2004; van Wijk, 2006; Larose *et al.*, 2006), crustal seismology (Campillo & Paul, 2003; Shapiro *et al.*, 2005; Roux *et al.*, 2005; Sabra *et al.*, 2005a,b), exploration seismology (Bakulin & Calvert, 2004; Calvert *et al.*, 2004; Bakulin & Calvert, 2006; Mehta & Snieder, 2008), helioseismology (Rickett & Claerbout, 1999), structural engineering (Snieder & Şafak, 2006; Snieder *et al.*, 2006), and numerical modeling (van Manen *et al.*, 2005). Seismic interferometry was first applied to wave propagation in non-attenuating and time-reversal invariant media (Lobkis & Weaver, 2001; Derode *et al.*, 2003; Weaver & Lobkis, 2004; Wapenaar, 2004; Snieder, 2004). Later, it was shown that interferometry can not only be applied to wavefields, but also to diffusive fields (Snieder, 2006b). Recent proofs have been given showing that the Green's function can be extracted for a wide class of linear systems including those that are attenuating, as well as those that may not be invariant for time-reversal because of flow (Godin, 2006; Wapenaar, 2006b; Wapenaar *et al.*, 2006; Snieder *et al.*, 2007; Weaver, 2008).

Seismic interferometry in the exploration geophysics community is also referred to as the *virtual source method* (Bakulin & Calvert, 2004; Calvert *et al.*, 2004; Bakulin & Calvert, 2006), and has been applied to imaging (Mehta *et al.*, 2007; Vasconcelos *et al.*, 2007). The sources used in seismic interferometry can be either controlled shots (Bakulin & Calvert, 2004; Calvert *et al.*, 2004; Schuster *et al.*, 2004; Bakulin & Calvert, 2006; Mehta *et al.*, 2007; van Wijk, 2006) or ambient noise (Weaver, 2005; Shapiro *et al.*, 2005; Roux *et al.*, 2005;

Stehly *et al.*, 2006; Godin, 2006; Curtis *et al.*, 2006; Miyazawa *et al.*, 2008).

Although the extraction of the Green's function is usually based on cross-correlation, deconvolution can also be used (Snieder & Şafak, 2006; Vasconcelos & Snieder, 2008a,b). The term "interferometry" in this chapter refers to cross-correlation based interferometry. Interferometry applied to acoustic waves can be expressed in the frequency domain as (Snieder *et al.*, 2007):

$$G(\mathbf{r}_A,\mathbf{r}_B,\omega) - G^*(\mathbf{r}_A,\mathbf{r}_B,\omega) = \oint_S \frac{1}{\rho}(G^*(\mathbf{r}_A,\mathbf{r},\omega)\nabla G(\mathbf{r}_B,\mathbf{r},\omega) - (\nabla G^*(\mathbf{r}_A,\mathbf{r},\omega))G(\mathbf{r}_B,\mathbf{r}))\widehat{\mathbf{n}}\cdot dS, \quad (2.1)$$

where $G(\mathbf{r}_A,\mathbf{r}_B,\omega)$ is the pressure Green's function that describes wave propagation from $\mathbf{r}_B$ to $\mathbf{r}_A$ respectively, $*$ indicates complex conjugation, S is the surface where sources are located, $\widehat{\mathbf{n}}$ is the unit vector perpendicular to the surface dS, ω the angular frequency, ρ the density and c the wave velocity. When the waves satisfy a radiation boundary condition on the surface S, $\nabla G(\mathbf{r}_A,\mathbf{r},\omega) \approx i(\omega/c)G(\mathbf{r}_A,\mathbf{r},\omega)\widehat{\mathbf{r}}$, and equation (2.1) becomes

$$G(\mathbf{r}_A,\mathbf{r}_B,\omega) - G^*(\mathbf{r}_A,\mathbf{r}_B,\omega) \approx 2i\omega \oint_S \frac{1}{\rho c} G(\mathbf{r}_A,\mathbf{r},\omega)G^*(\mathbf{r}_B,\mathbf{r},\omega)(\widehat{\mathbf{r}}\cdot\widehat{\mathbf{n}})dS, \quad (2.2)$$

Thus, the integration over all source positions of the cross-correlation of $G(\mathbf{r}_A,\mathbf{r},\omega)$ and $G(\mathbf{r}_B,\mathbf{r},\omega)$ yields the superposition of the causal Green's function $G(\mathbf{r}_A,\mathbf{r}_B,\omega)$ and time-reversed Green's function $G^*(\mathbf{r}_B,\mathbf{r},\omega)$. Using the geometric relationship defined in figure 2.1, equation (2.2) becomes

$$G(\mathbf{r}_A,\mathbf{r}_B,\omega) - G^*(\mathbf{r}_A,\mathbf{r}_B,\omega) \approx 2i\omega \oint_{S'} \frac{1}{\rho c} G(\mathbf{r}_A,\mathbf{r},\omega)G^*(\mathbf{r}_B,\mathbf{r},\omega)dS', \quad (2.3)$$

in which $dS' = dScos\psi$ is the projection of the surface element dS on a circle with radius r. A similar mathematical expression exists for the extraction of the Green's function for diffusion. The main difference is that the surface integral becomes a volume integral

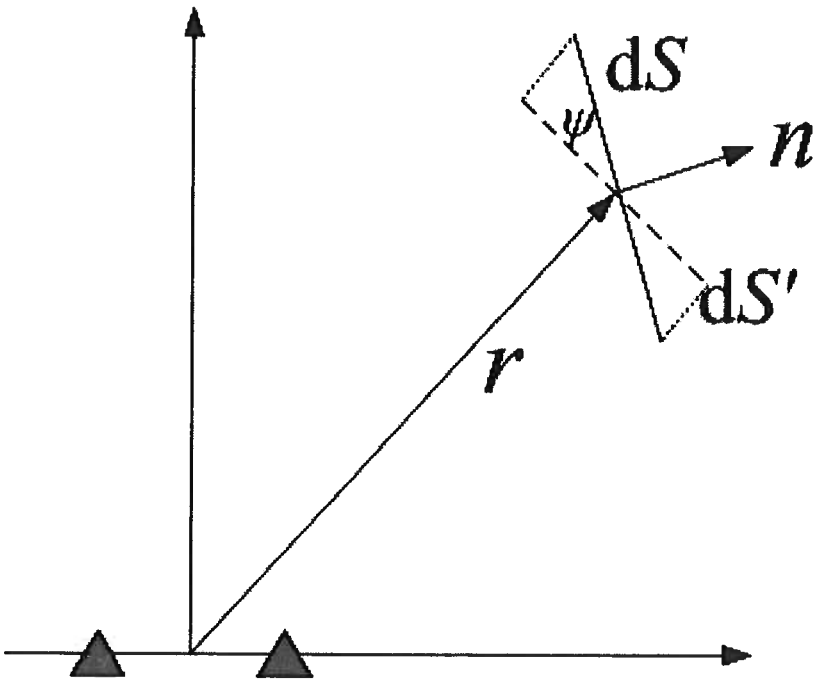

Figure 2.1. An arbitrary surface element dS and its projection dS'

(Snieder, 2006b):

$$G(\mathbf{r}_A, \mathbf{r}_B, \omega) - G^*(\mathbf{r}_A, \mathbf{r}_B, \omega) = 2i\omega \int_V G(\mathbf{r}_A, \mathbf{r}, \omega) G^*(\mathbf{r}_B, \mathbf{r}, \omega) dV, \qquad (2.4)$$

in which V is the volume containing the sources. The meaning of other terms are the same as those in equation (2.3).

Equations (2.3) and (2.4) show that the main difference between wave equation and diffusion equation interferometry is the required source distribution. For waves, equation (2.3) shows that if two receivers are surrounded by active sources on a closed surface, the response that describes waves propagating between two receivers can be reconstructed as if one of the receivers were an active source. For diffusion, equation (2.4) states that sources are required to be everywhere in the volume (Snieder, 2006b). In practice, there are only a finite number of sources. Therefore, one can never have a closed source surface for waves or

sources throughout the volume for diffusion. This raises the question: what is the required source density and how should one locate these sources in order to reconstruct the Green's function accurately?

The importance of cross-correlation-based interferometry for waves has been addressed by numerous authors. Cross-correlation-based interferometry for diffusion is still at the theory stage. In exploration geophysics, there are at least two important diffusive fields: pore pressure and low-frequency inductive electromagnetic fields. From the pore pressure one can infer the fluid conductivity between wells (Bourdet, 2002; Kutasov *et al.*, 2008). Electromagnetic fields carry information about the resistivity of the pore fluid and may thus help distinguish between hydrocarbons and water. For offshore oil exploration, controlled-source electromagnetic (CSEM) is an important technique used to detect hydrocarbons (Hoversten *et al.*, 2006; Constable & Srnka, 2007; Darnet *et al.*, 2007; Scholl & Edwards, 2007).

2.3 Model and Results

I study the required source distribution in both homogeneous and heterogeneous media for waves, and a homogeneous model for diffusion, with a finite number of sources using numerical experiments. In the next section we discuss these simulations, providing explanations of the observations. We first show numerical experiments demonstrating the extraction of wave equation Green's function.

2.3.1 Waves in Homogeneous Media

For simplicity we first show numerical tests using a 2-D model with a velocity of 1 km/s. To define the source position, we use two parameters: the source angle and source radius as shown in Figure 2.2. A and B are two receivers with a separation b. The vectors connecting the source to the two receivers are denoted by $\mathbf{r}_{SA}$ and $\mathbf{r}_{SB}$, respectively. The source function we use for the examples in the wave part for homogeneous media is a Ricker wavelet with a central frequency of 0.5 Hz. The source amplitude is the same for all sources

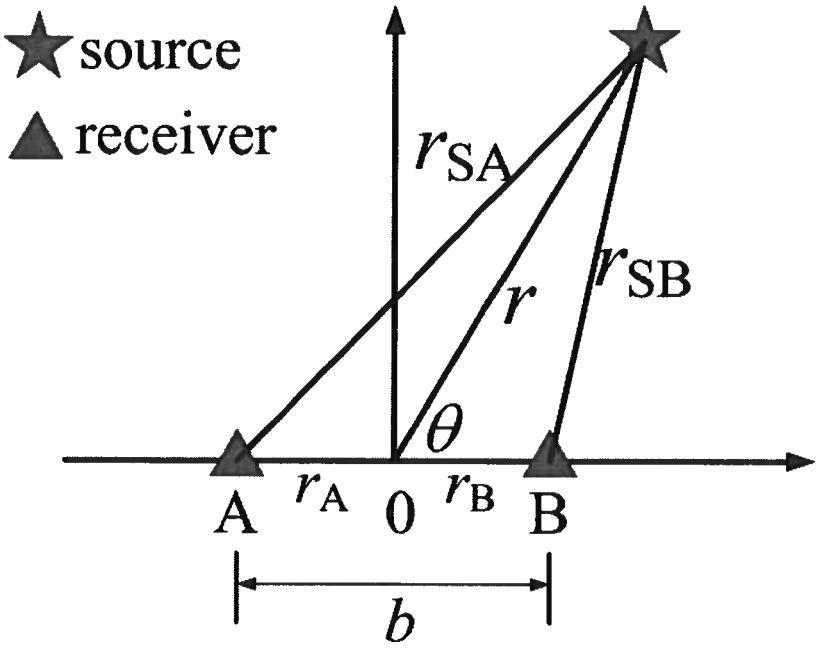

Figure 2.2. Definition of the source radius r and source angle θ that define a source position in 2-D.

in all the experiments in this chapter.

Experiment 1: uniformly distributed source angle.

I first study the effect of the source angle distribution. Sources are uniformly distributed on a circle with a radius of 40 km. The distance between the two receivers is 6 km. Figure 2.3 shows the reconstructed response between the two receivers for a homogeneous distribution of sources with increasing number of sources. The response has two parts, the causal and anti-causal parts as represented by equation (2.3). The causal part of the signal represents the signal propagating from receiver A to B and the anti-causal part is the time-reversal of this, i.e. the signal propagating from receiver B to A. If we replace one of the receivers with an active source, the received signal arrives after a propagation time of 6 s. To make the shape of the received signal the same as that of the reconstructed signal, we correlate the received signal with the source-time function. This new signal is represented by the

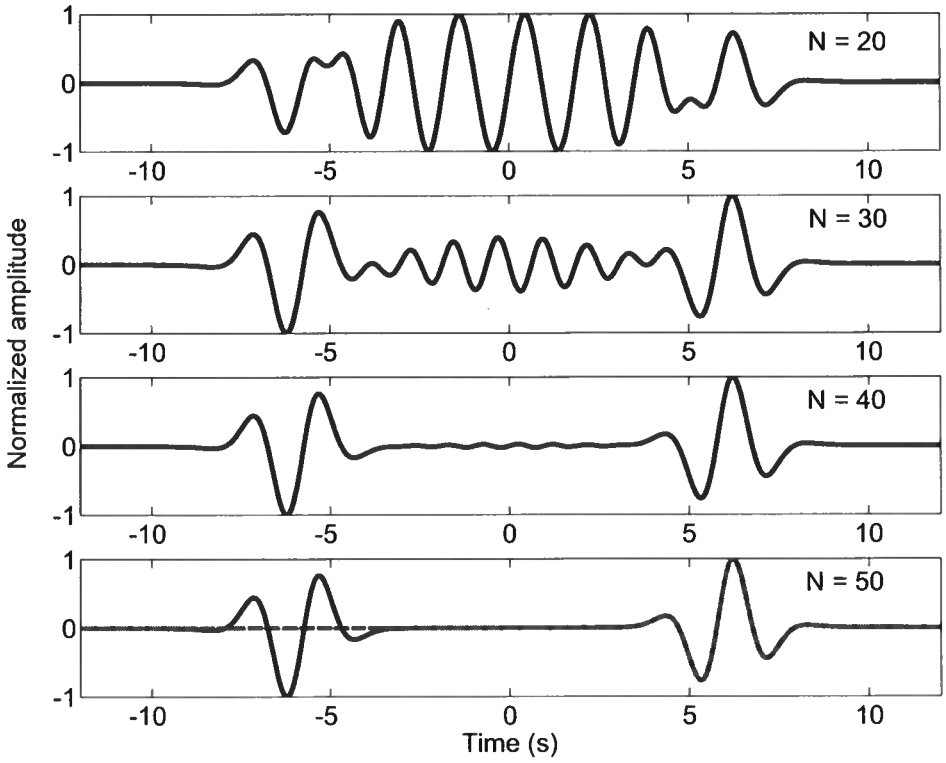

Figure 2.3. Reconstructed responses (solid lines) for uniform angle distribution with different number of source N (the dashed line in the bottom panel is the exact response between the two receivers)

dashed line in the bottom panel and is virtually indistinguishable from the causal part of the reconstructed response with 50 sources (the amplitudes of both reconstructed and active signals are normalized). The main point in figure 2.3 is that the oscillations observed in the middle part of the reconstructed signal decreases with increasing number of sources N. Hence, a minimum source density needs to be exceeded for extracting the response successfully. This required source density is derived in the discussion part of this section.

I quantify the spurious fluctuations that arrive between the anti-causal and the causal response by defining the fluctuation energy

$$E_m = \frac{1}{N_m} \sum_{i=1}^{N_m} A[i]^2, \tag{2.5}$$

in which N_m is the number of the discrete sample points in the middle part of the signal (i.e. the part between the two main pulses), $A[i]$ is the amplitude of the ith sample point in the middle part. Figure 2.4 shows this fluctuation energy decay as a function of number of sources N. Weaver & Lobkis (2005) showed that these fluctuations decay as N^{-1} if the sources are randomly distributed. Figure 2.4 shows that when the sources are uniformly distributed in angle, the decay rate is much faster than N^{-1}. The reason of this is shown in the discussion part of the wave problem.

Note that the sources are always distributed starting from angle zero (the line crossing two receivers) in the example. By doing this, there is always a source located at angle zero (one stationary point). If the starting point of angle distribution is arbitrary, the energy fluctuation behavior with a small number of sources is not exactly the same as the one shown in figure 2.4. This difference in the energy fluctuation is caused by different sampling of the stationary phase zone by sources. The stationary phase zones for the configuration in this example are shown by the dashed curves in figure 2.5. The sources that are located in the stationary phase zones give the most contribution to the physical arrivals in the Green's function reconstruction (Snieder, 2004). For small number of sources, the sampling

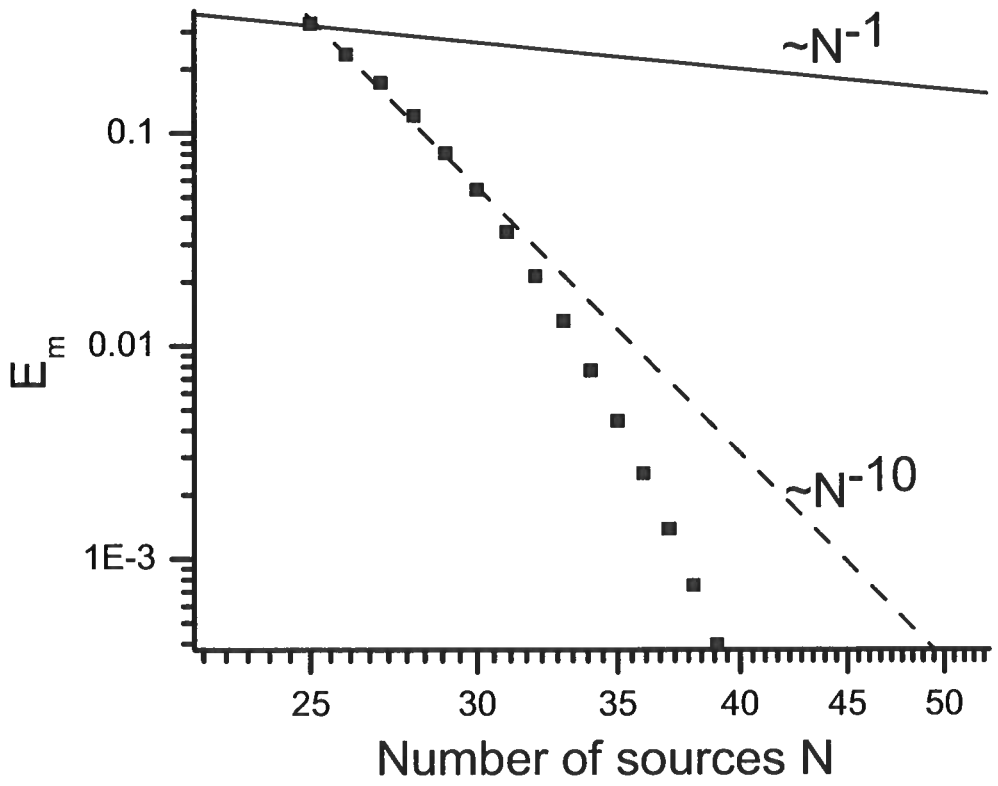

Figure 2.4. Fluctuation energy decay as a function of number of sources N for the uniform angular distribution of sources. The dashed and solid line represent two different power-laws in the log-log coordinate system.

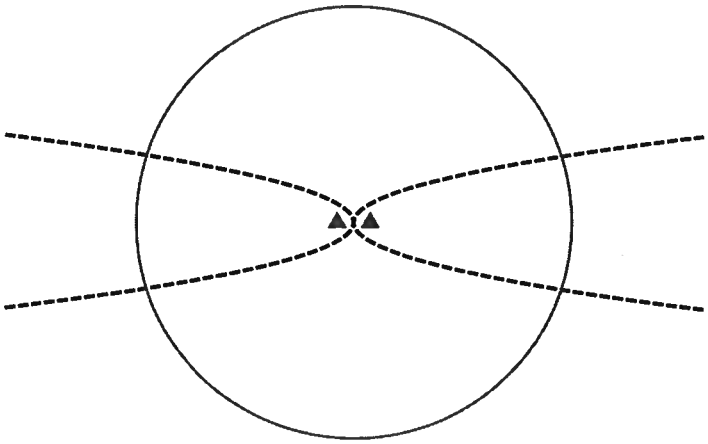

Figure 2.5. Stationary phase zone (denoted by the dashed curves) in a homogeneous medium.

of the stationary phase zone is sensitive to where the first source is located. Therefore, the decaying behavior of the energy fluctuation E_m varies depending on where the first source is located when the number of sources is small (< 50 in this case). With a large number of sources, it does not matter anymore where the first source is located because the stationary phase zone can always be sampled sufficiently.

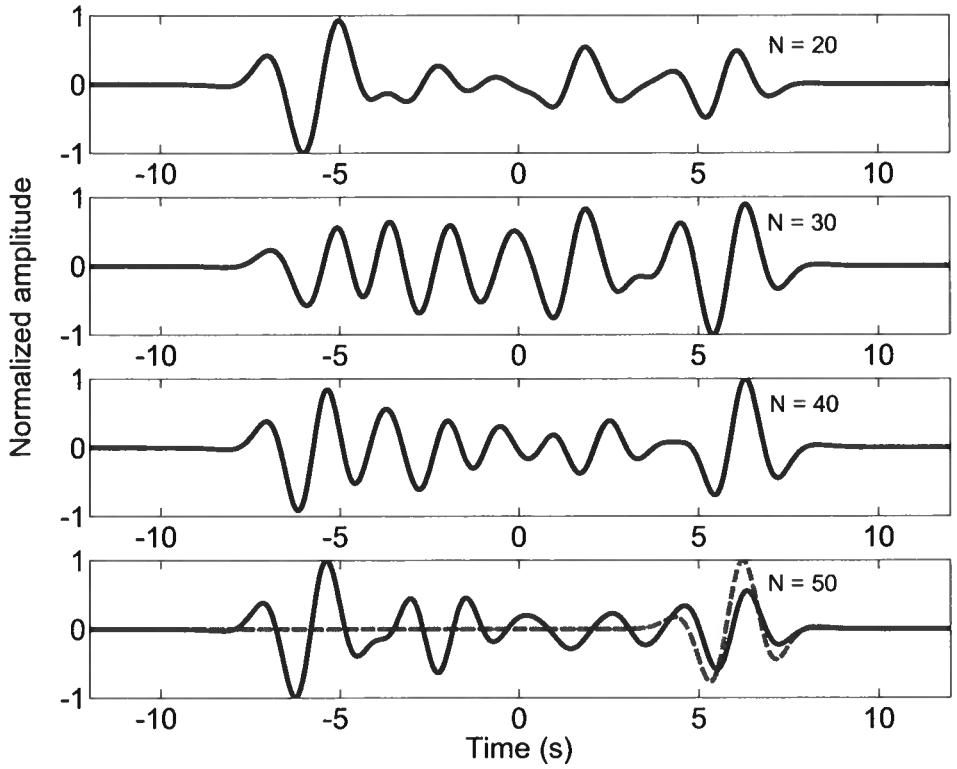

Figure 2.6. Reconstructed responses (solid lines) for random angular distribution with different number of sources N (the dashed line in the bottom panel is the exact response between the two receivers).

Experiment 2: randomly distributed source angle.

In this experiment, the source angles are randomly distributed with constant source radius. Figure 2.6 shows the reconstructed response as a function of the number of sources N for a random angular distribution of sources along the circle. Compared with figure 2.3, the random distribution gives a much poorer reconstruction than does the uniform distribution with the same number of sources. Figure 2.7 shows this fluctuation energy decay, as defined in equation (2.5), as a function of N for randomly distributed sources. The fluctuation decay behavior is consistent with the prediction of Weaver and Lobkis(2005): the decay

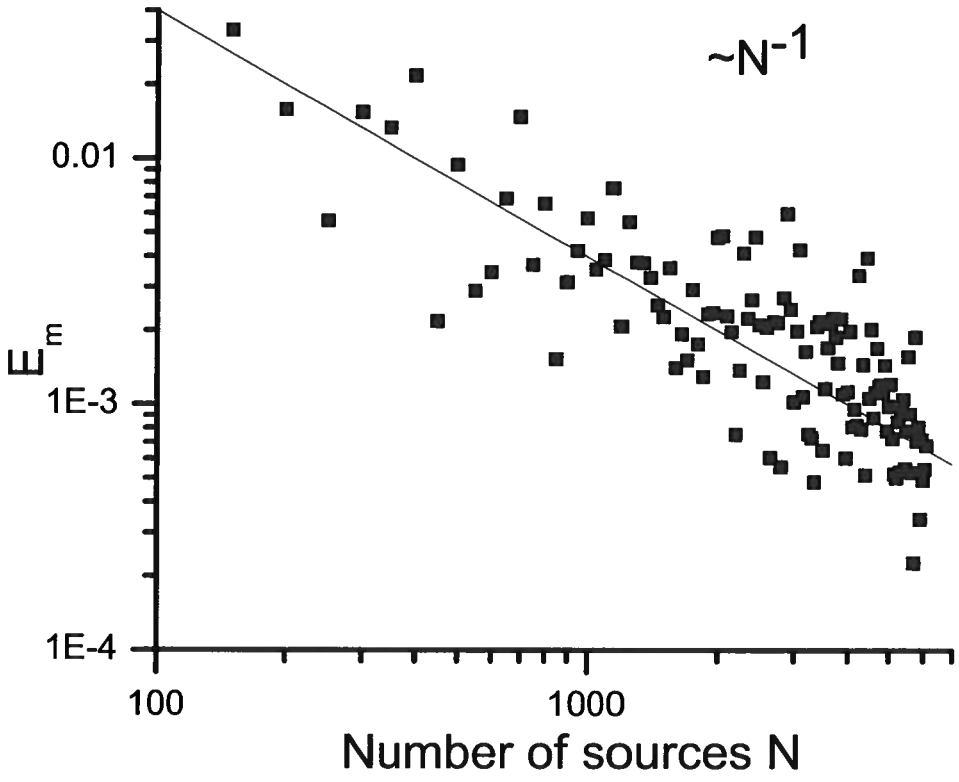

Figure 2.7. Fluctuation energy decay as a function of number of sources N for the random angular distribution of sources. The solid line represents a N^{-1} power-law decay in the log-log coordinate system.

is proportional to N^{-1}. In contrast to the uniform distribution, it does not matter where the first source is located for the random distribution. In this experiment, the source radius remains much larger than the distance between the two receivers. If the radius is very small (for example 6 km), the fluctuation E_m decays more slowly ($N^{1/2}$) because the radiation boundary condition that reduces equation 2.1 to equation 2.2 is inaccurate. Experiment 2 suggests that not only the number of sources is important, but also their angular distribution. The difference of this decay rate of uniformly and randomly distributed sources is explained in the discussion part of this section.

Experiment 3: smooth source angle distribution.

From experiments 1 and 2, one might conclude that the source angle needs to be uniformly distributed with angle to apply this technique successfully with a small number of sources. Figure 2.8 shows that the angles not necessary have to be uniformly distributed but may be smoothly varying. Next we show examples with non-uniform but smoothly varying angle distribution where the response is accurately reconstructed. In the example shown in figure 2.8, the sources are uniformly distributed on a circle with the center of the two receivers moved away from the center of the circle (from (0,0) to (-5,6)). This makes the source angle distribution no longer uniform, but it's still smooth. The numerical simulation shows accurate reconstruction of the response from 50 sources. The amplitude differences of the causal and anti-causal parts are due to the different energies from the two stationary-phase zones on the left and right side of the receivers as illustrated by the two dashed curves in the upper panel of figure 2.8. Only sources within these two stationary zones contribute to the extraction of the direct wave (Snieder, 2004; Roux *et al.*, 2005). In this case, the stationary zone on the right side corresponds to the causal pulse and the left stationary zone corresponds to the anti-causal pulse. In the right stationary zone there are more sources than on the left side. This explains why the causal pulse is stronger than the anti-causal one. Notice that the distance of the sources to the midpoint of the

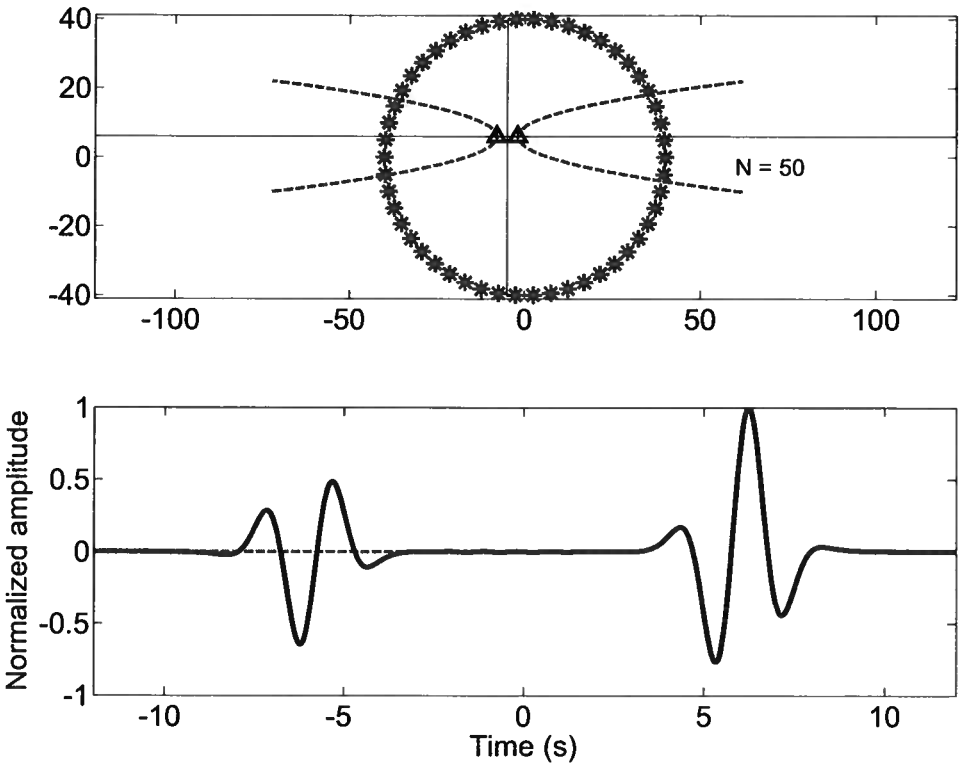

Figure 2.8. Reconstructed response (solid line in the lower panel, dashed line is the exact response) for a smoothly varying source angle distribution (upper panel)

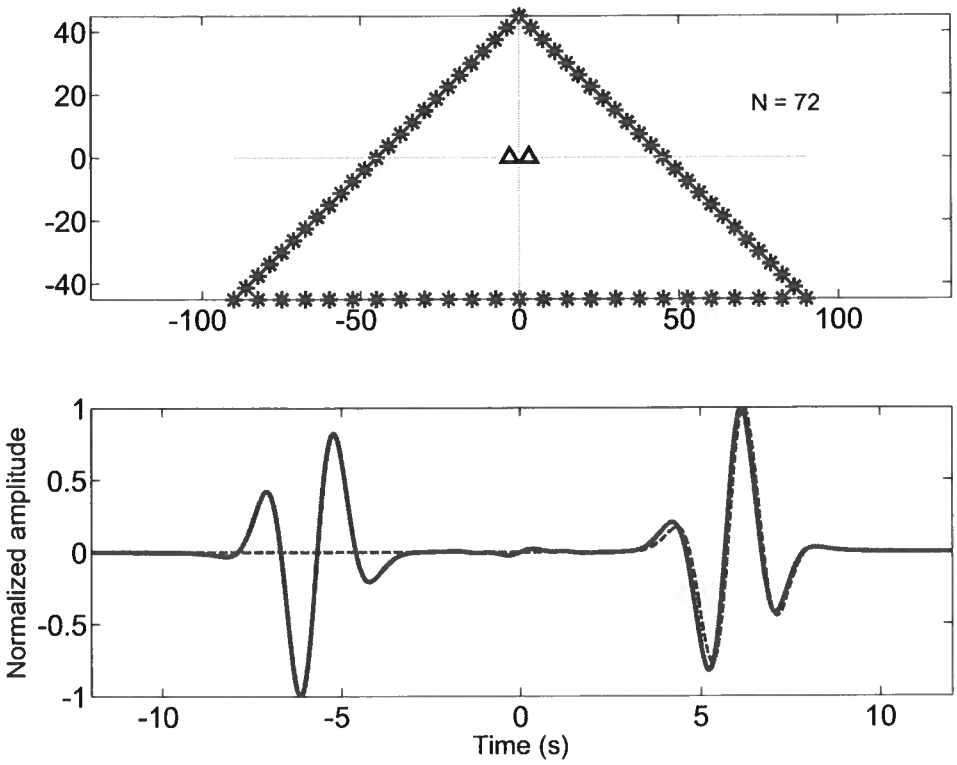

Figure 2.9. Reconstructed response (solid line in the lower panel, dashed line is the exact response) for source spaced equidistantly on a triangle (upper panel)

receiver locations is not constant in this experiment. In the example shown in figure 2.9, the sources are uniformly distributed on the sides of a triangle. The source angle is not uniform but is smoothly varying. The lower panel in figure 2.9 shows that for 72 sources, the reconstruction of the response is still accurate. In this case, the required number of sources is slightly larger than that for the uniform distribution but much smaller than for the accurate reconstruction of the Green's function with the random source distribution. The value of this number depends on the smoothness of the angular variation. Similar to an acquisition geometry with sources along a line (Bakulin & Calvert, 2006; Mehta *et al.*, 2007), the source radius now varies with the source position. Note that in this example the source radii are much larger than the distance between the two receivers. Thus, the influence of varying source radii is negligible. This is shown in detail in the next experiment.

Experiment 4: varying source radius.

In the previous three experiments we learned how the angular distribution influences the response extraction. The uniform angular distribution has a faster decay rate of the fluctuation energy E_m (N^{-10}) than for the random angular distribution (N^{-1}). The number of sources required for a smoothly varying angle distribution is between these two extreme cases and it depends on how smooth the angular distribution is. There is, however, still another parameter: the radius r as defined in figure 2.2. In this example we compare the result from two distributions with the same angular distribution but different source radii. The first one is the example we showed in experiment 1, when 50 sources are uniformly distributed on a circle (stars in the upper panel of figure 2.10). The second one is for sources with the same angle distribution but the radius is randomly varying in a range in which all radii are much larger than the distance between the two receivers (dots in the upper panel of figure 2.10. The reconstructed responses in figure 2.10 suggest that varying the source radii does not degrade the accuracy of the Green's function extraction. This is only true when source radii are much larger than the distance between the two receivers. The reason for this is explained in the discussion part.

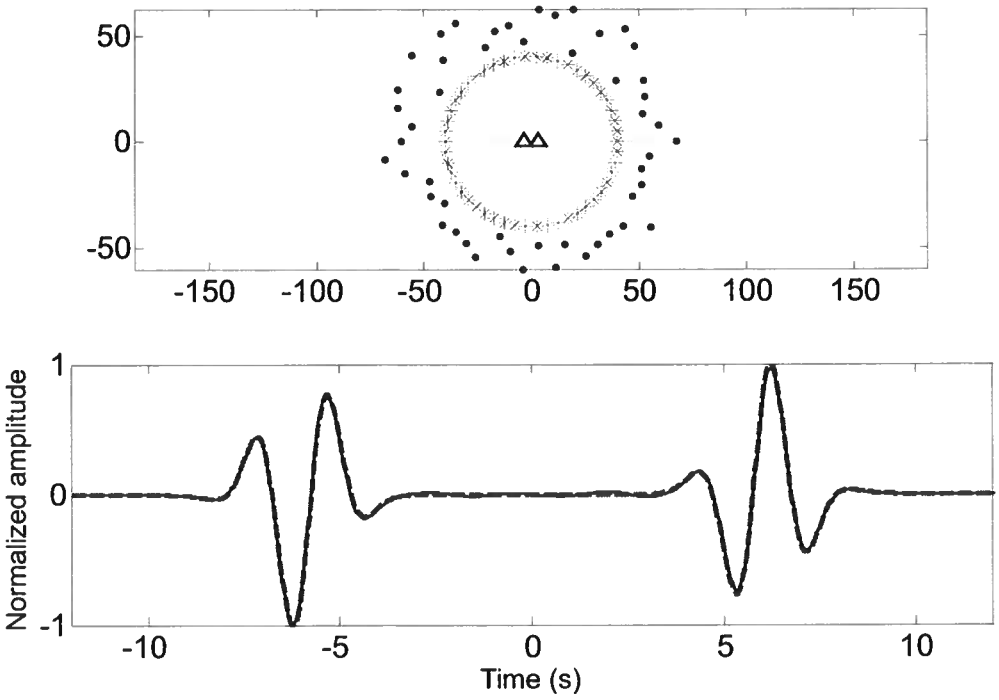

Figure 2.10. Two source distributions with the same angular distribution but different radii (top) and the reconstructed responses: solid (same radius), dashed line (different radius)

2.3.2 Waves in Heterogeneous Media

It is commonly believed that the source distribution is less important for the heterogeneous medium than for a homogeneous medium because the heterogeneity scatters the wave fields into different directions. In an extreme case, one might think that one source is sufficient to reconstruct the Green's function if the medium is sufficiently complicated. In this study, we find that these beliefs are not correct and more sources are required to reconstruct the full Green's function for a strongly heterogeneous medium than for an homogeneous medium.

The heterogeneous medium in this section consists of 200 isotropic point scatterers in a 80 m by 80 m square around the two receivers. The source radius is 90 m and the receivers are 20 m apart. The wavefield was modeled using the theory of Groenenboom and Snieder (1995), which takes all multiple scattering events into account. The waveform is a Gaussian wavelet with 600Hz the center frequency and bandwidth 400 Hz. The phase velocity in the background medium is 1500 m/s.

Figure 2.11 shows the the reconstructed responses between the two receivers using full illumination (sources uniformly distributed around the medium) and one single source. The red dashed curve is the signal received by one receiver when the other one acts as a real source. The black solid curve is the signal reconstructed by interferometry. Panel (a) shows the reconstruction when 300 uniformly distributed sources are used while panel (c) is the case when a single source is used. Panels (b) and (d) are the enlarged version of panels (a) and (c), respectively. The correlation coefficient between the exact and the causal part of the extracted signal is 0.97 for the 300 uniformly distributed sources while it is -0.03 for the single source. In this scattering medium, the wavefield from a single source is equipartitioned, see the discussion part. Perhaps surprisingly, the reconstructed signal from a single source does not represent the Green's function between the two receivers at all. We also find that more sources are needed to reconstruct the Green's function accurately for this heterogeneous medium (300 sources) than for a homogeneous medium (140 sources) with the same velocity, source wavelet and source distribution. Derode et al. (2003) reached a

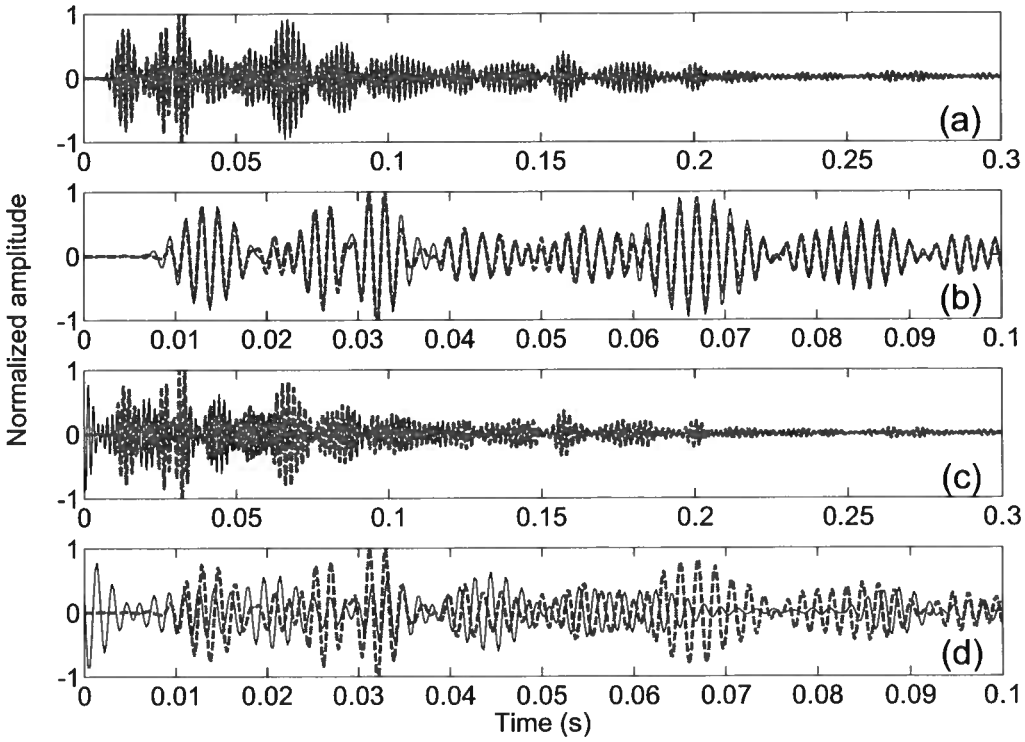

Figure 2.11. The Green's function reconstruction in a strongly scattering medium. The red dashed curve is the active experiment and the black solid curve is the reconstruction. Panel (a) shows the reconstruction when 300 uniformly distributed sources are used while panel (c) is the case when a single source is used. Panels (b) and (d) are the enlarged version of panels (a) and (c), respectively.

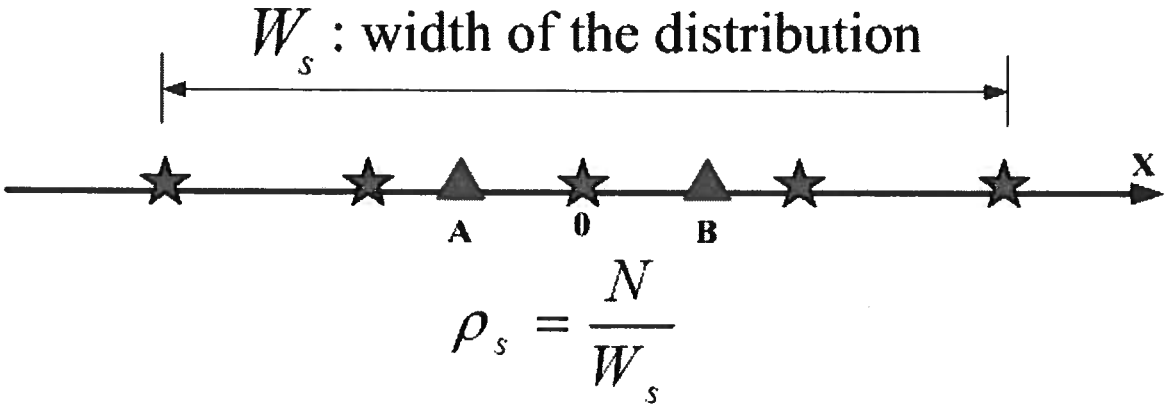

Figure 2.12. 1-D source distribution and the definitions of geometric parameters.

similar observation based on their finite difference simulations. An explanation and required source density in an strongly scattering medium is given in the discussion section.

2.3.3 Diffusion

Equation (2.4) shows that one needs sources in the entire volume to extract the diffusion Green's function. To simplify the problem, we first analyze a 1-D medium with a constant diffusion coefficient and then extend my investigations to 3-D.

Experiment 1: diffusion Green's function recovery in 1-D.

I choose the origin of the coordinate system to be the mid-point between the two receivers. The separation of the two receivers is 2 km. The diffusion coefficient used in this model is $D = 1\ km^2/s$. We distribute sources uniformly on the 1-D line with the center of the distribution at origin. Figure 2.12 shows the geometry of 1-D source distribution. I define two parameters to characterize this source distribution. As shown in figure 2.12, W_s is the width of the distribution and $\rho_s = N/W_s$ is the source density. Next we test three different distributions. The first is a distribution with narrow width W_s and high source density ρ_s (figure 2.13). The second is a distribution with the same number of sources, but with a wide width W_s and low density (figure 2.14). The third distribution has more sources and has

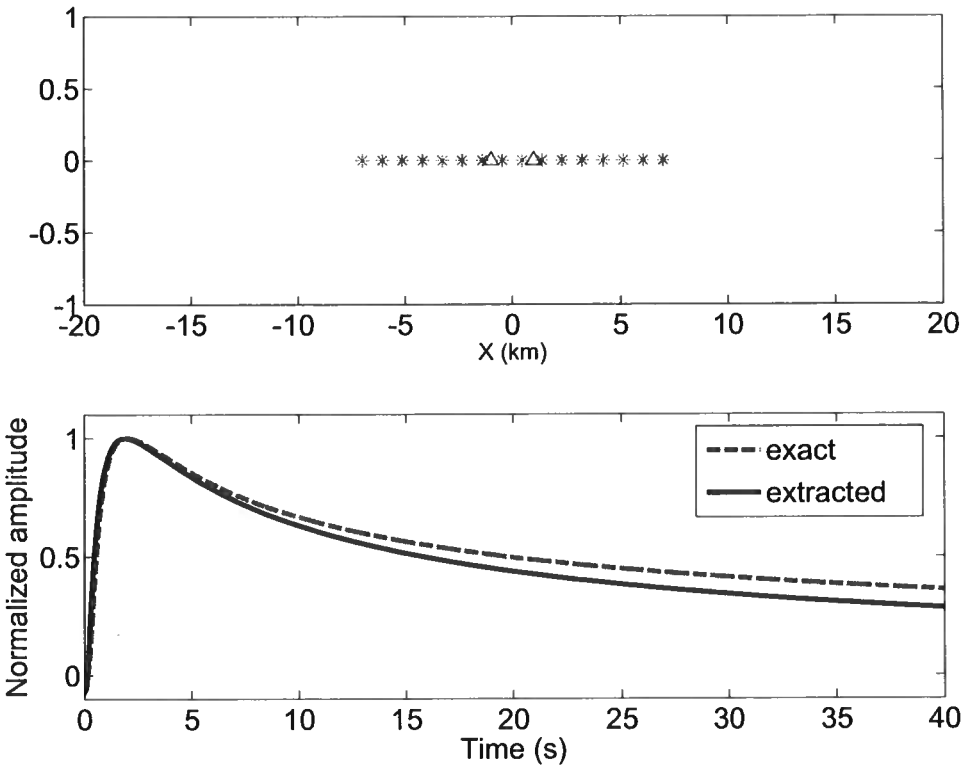

Figure 2.13. 1-D source distribution (upper panel) with Ws=14 km, ρ_s=1.143 km^{-1} and the extracted Green's function (lower panel).

wide W_s and high density ρ_s (figure 2.15). Figures 2.13 to 2.15 show that different source distributions are needed for the accurate reconstruction of the early-time and the late-time response. The early-time response is defined as the response before the peak in the Green's function of the diffusion equation, the late-time part is defined as the response after the main peak. The early-time reconstruction is controlled by the source density ρ_s (figure 2.13 and 2.15) and late-time reconstruction is more affected by the distribution width Ws (figure 2.14 and 2.15).

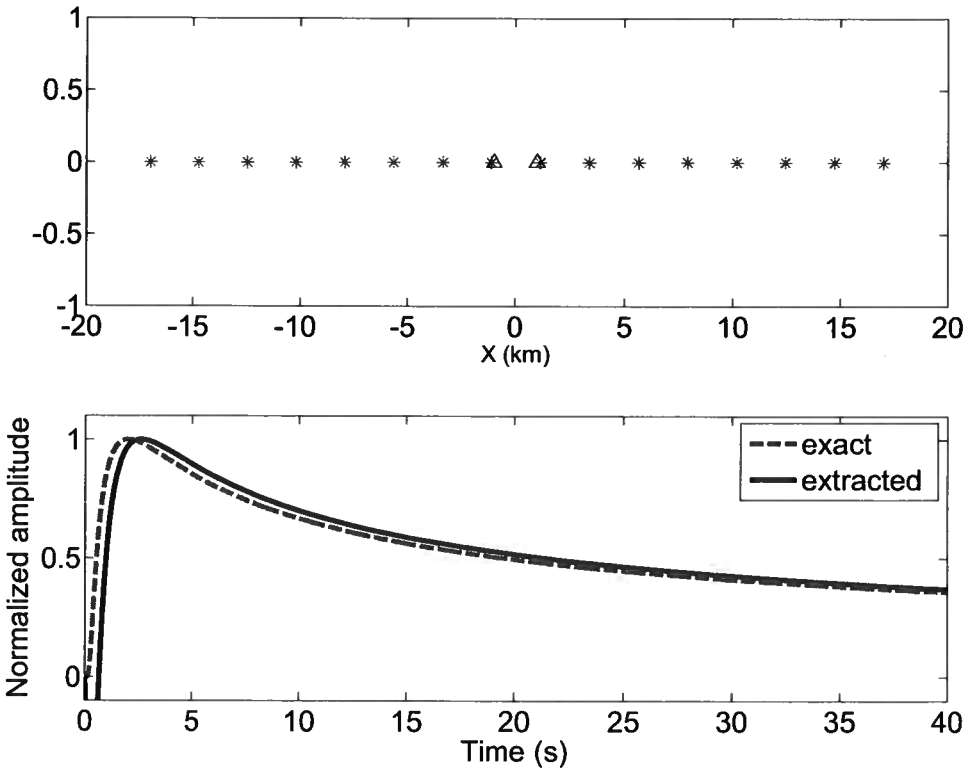

Figure 2.14. 1-D source distribution (upper panel) with $Ws = 34$ km, $\rho_s = 0.47\ km^{-1}$ and the extracted Green's function (lower panel).

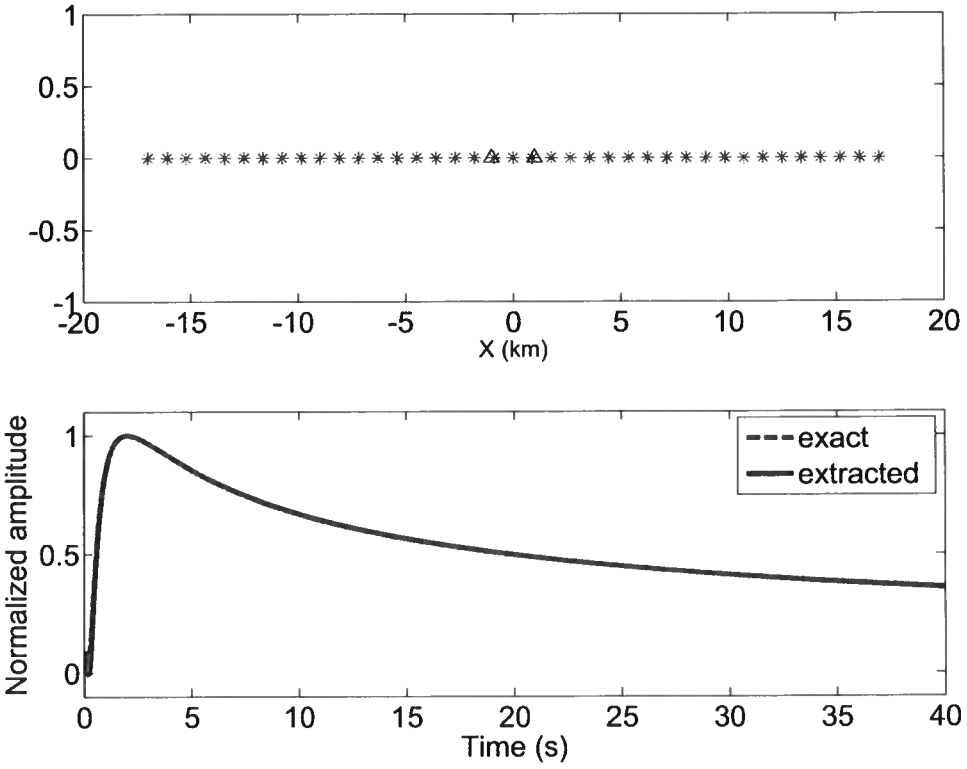

Figure 2.15. 1-D source distribution (upper panel) with $Ws = 34$ km, $\rho_s = 1.147\ km^{-1}$ and the extracted Green's function (lower panel).

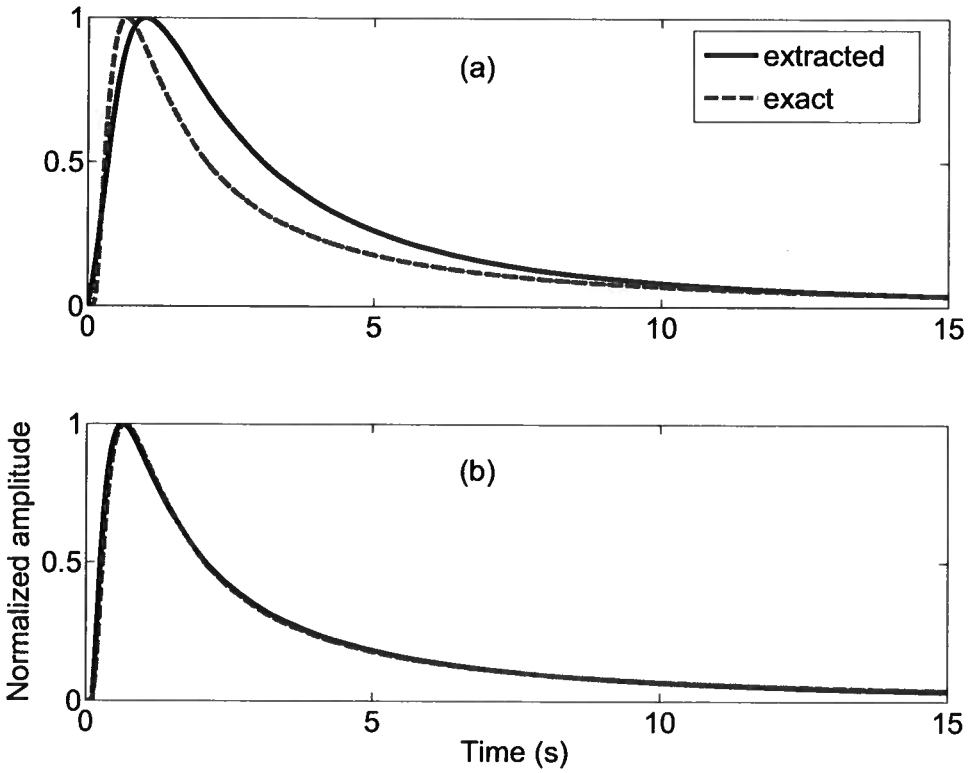

Figure 2.16. 3-D reconstruction of diffusion Green's function. (a)W_s = 2.5 km and ρ_s = 0.51 km^{-3}. (b)W_s = 10 km and ρ_s = 0.51 km^{-3}.

Experiment 2: Green's function reconstruction for diffusion in 3-D.

Following the same strategy we extend the diffusion experiment to 3-D. Instead of putting the sources on a line, we uniformly distributed them in a cube. We define W_s as the side length of the cube, and the source density is defined as $\rho_s = N/(W_s)^3$.

In figure 2.16a, a source distribution with small W_s is used. As in 1-D, the early-time of the Green's function is reconstructed well, but the late-time behavior is not. When the width of the distribution increased, with sufficiently high source density ρ_s, both early and late-time can be extracted well (figure 2.16b).

2.4 Discussion

The discussion of the experiments follows the same order as the experiments in the last section.

2.4.1 Waves in Homogeneous Media

The Green's function of the wave equation of a homogeneous medium in 2D is represented in the frequency domain by the first Hankel function of degree zero (Snieder, 2006a):

$$G(r) = \frac{i}{4} H_0^{(1)}(kr). \tag{2.6}$$

In the numerical simulations for waves in homogeneous media, we use the far-field approximation of equation (2.6), which is

$$G(r) = \sqrt{\frac{1}{8\pi kr}} e^{i(kr+\pi/4)}. \tag{2.7}$$

Inserting this into equation (2.3), we obtain

$$\begin{aligned} &G(\mathbf{r}_A, \mathbf{r}_B, \omega) - G^*(\mathbf{r}_A, \mathbf{r}_B, \omega) \\ &\quad \approx \frac{i}{4\pi\rho} \oint_{S'} \sqrt{\frac{1}{r_{SA} r_{SB}}} e^{ik(r_{SA}-r_{SB})} dS', \end{aligned} \tag{2.8}$$

When the source radius is much larger than the distance between the two receivers, the distance in the geometrical spreading can be approximated as $r_{SA} \approx r_{SB} \approx r$, while for the phase the approximation $r_{SA} - r_{SB} \approx b\cos\theta$ is accurate to first order in b/r (These parameters are defined in figure 2.2.) Using these approximations and the relationship $dS' = rd\theta$, equation (2.8) becomes

$$G(\mathbf{r}_A, \mathbf{r}_B, \omega) - G^*(\mathbf{r}_A, \mathbf{r}_B, \omega) \approx \frac{i}{4\pi\rho} \int_0^{2\pi} e^{ikb\cos\theta} d\theta \tag{2.9}$$

Note that the right hand side does not depend on the source radius r. Experiment 4 in the wave part supports this conclusion: in that experiment, variations in the source radius do not influence the Green's function extraction.

The source radius enters this interferometry problem in three ways. The first is the geometrical spreading term $1/r$, the second is the relationship between the surface element and the increment in source angle $dS' = rd\theta$, and the third is the width of the stationary-phase zones as illustrated in the upper panel of figure 2.8. Equation (2.9) confirms that the first two factors compensate each other. Consequently, only the width of the stationary-phase zones contribute to the amplitude of the reconstructed signal. The different number of sources in the left and right stationary-phase zones cause the asymmetry in the amplitude of causal and anti-causal response as shown in the lower panel of figure 2.8.

Another interesting observation is that the right hand side of equation (2.9) is the integral representation of the Bessel function (Snieder, 2006a), which is related to the exact Green's function:

$$\begin{aligned} \frac{1}{2\pi}\int_0^{2\pi} e^{ikbcos\theta}d\theta &= J_0(kb) \\ &= \frac{1}{2}\left[H_0^{(1)}(kb) - H_0^{(1)}(-kb)\right] \end{aligned} \tag{2.10}$$

This shows that by using only far-field of the waves in the interferometry, both far-field and near-field response are reconstructed. This was shown for elastic waves by Sánchez-Sesma *et al.* (2006) and Sánchez-Sesma & Campillo (2006).

For the dependence on the angle θ, we need to study the character of the integrand in equation (2.9). The real part of this integrand is the oscillatory function shown in figure 2.17. The extraction of the Green's function depends on the sampling of this integral over source angle θ, and reduces to the numerical integration of a continuous oscillatory function. For a homogeneous source distribution we effectively use Simpson's rule to represent this integral by summation ($\int F(\theta)d\theta \rightarrow \sum_{i=1}^{N} F(\theta_i)\Delta\theta$). While for random angular distribution, this

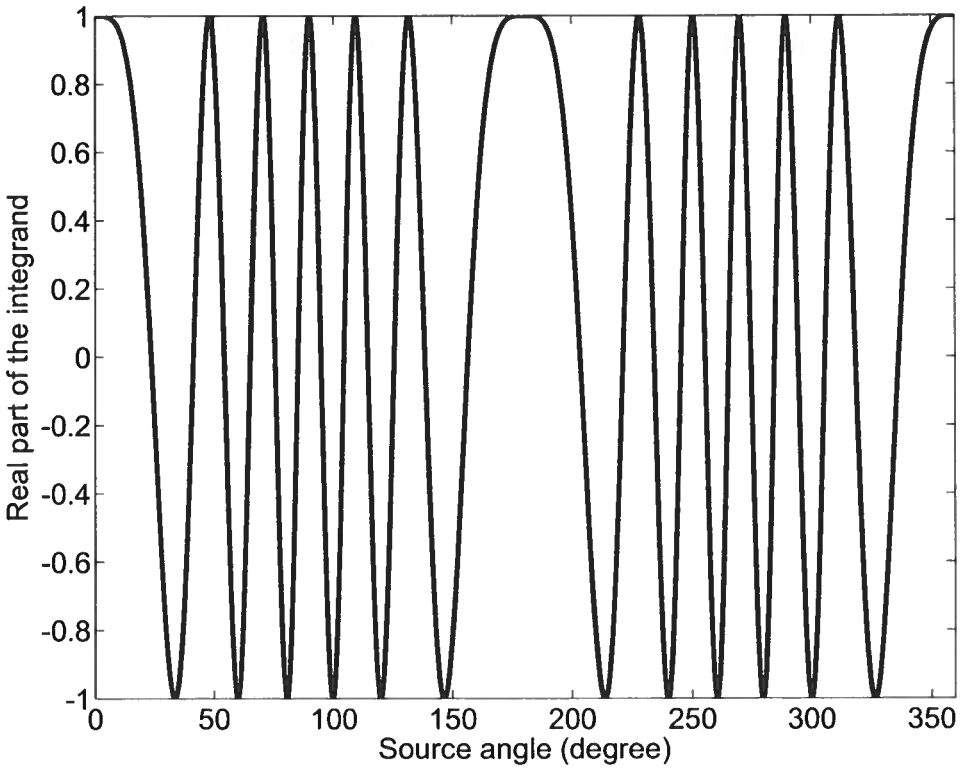

Figure 2.17. The real part of the integrand in equation (2.9).

would not give an accurate estimation with a small number of sources by using summation to replace integral ($\int F(\theta)d\theta \rightarrow \sum_{i=1}^{N} F(\theta_i)\Delta\theta_i$). If the angle separation for each source is known, one may use $\Delta\theta_i$ as a weight in the summation as it does in the numerical integral. But if there is no information on $\Delta\theta_i$, the average over repeated experiments with different random distributions converges to a more accurate reconstruction. Figure 2.18 shows a histogram of 100 repeated estimations of the integration of the function (figure 2.17) using random sampling points. In each realization, 1000 randomly distributed sources are used to estimate this integral. The estimated value for a specific realization can be far from the exact value while the average over all realizations (dashed line) is close to the accurate value (solid line). For a smoothly varying source angle, $\Delta\theta_i$ is locally fairly constant and therefore the reconstruction is still accurate with a relatively small number of sources. For most of the applications of interferometry using controlled shots, the source angle is actually smoothly changing (Bakulin & Calvert, 2006; Mehta *et al.*, 2007). Here we explain why those smooth source angle distributions from experiment 3 for waves give accurate Green's function reconstruction.

What is the minimum required source density if the sources are uniformly distributed in a homogeneous medium? As shown in figure 2.17, the oscillations have a variable period. In order to make the highest frequency oscillations cancel so that the stationary phase contribution remains (Snieder, 2004), we need to have enough sampling points at the fastest oscillation. This oscillation depends on the phase term $\Phi = kbcos\theta$ of equation (2.9). The change in the phase for an angular increment $\Delta\theta$ is $\Delta\Phi = kbsin\theta\Delta\theta$. The most rapid oscillation happens at $sin\theta = 1$. In order to have N_r number of sources within the period of the most rapid oscillation, the required source density becomes

$$\rho_s = \frac{N_r kb}{2\pi} \ (radian^{-1}), \tag{2.11}$$

Based on the numerical simulations, when $N_r > 2.5$, the fluctuation energy between the

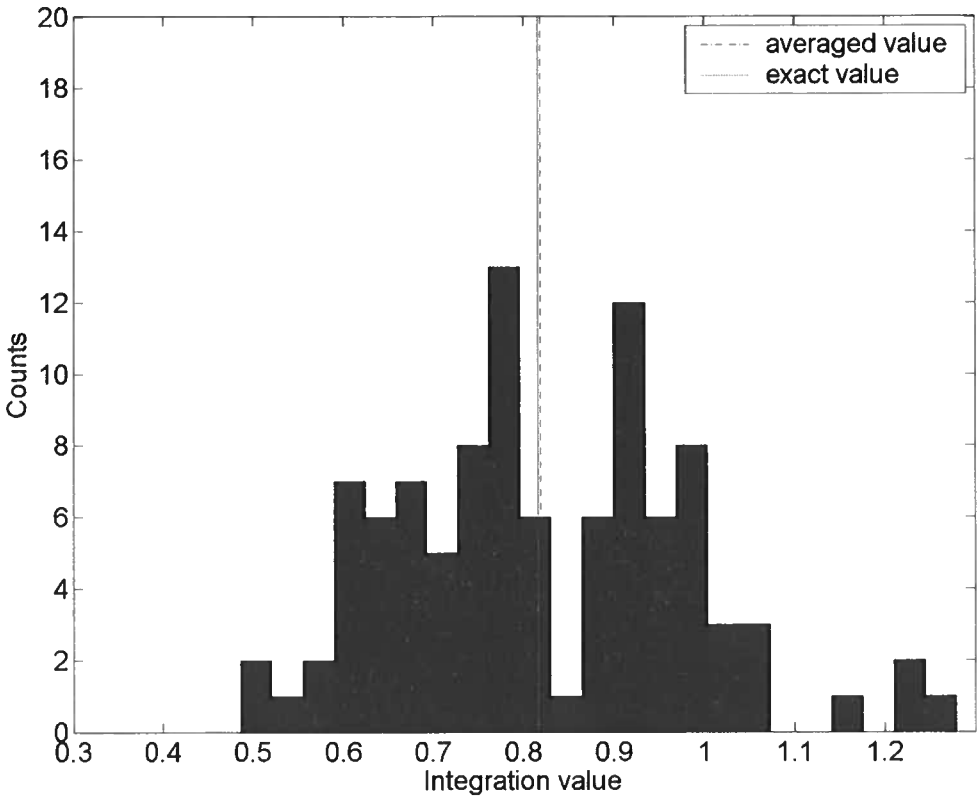

Figure 2.18. Histogram of 100 repeated estimations of the integral in figure 2.17 using 1000 randomply placed sources in each estimate.

two main pulses in the reconstruction vanishes, this gives the sampling criterion

$$\rho_s = 0.4kb \ (radian^{-1}). \tag{2.12}$$

In practical applications, sources may only be located in the stationary zone. In tat case, there is no need to cancel the high oscillations in figure 2.17, and the required source density can be smaller than the one shown in equation 2.12. The source density needed to adequately sample the stationary zone is derived below. The width of the stationary zone (the angle between the two nearest minimum points) is $2cos^{-1}(1-\pi/kb)$. In order to have N_r number of sources within this stationary zone, the required source density is

$$\rho_s = \frac{N_r}{2cos^{-1}(1-\pi/kb)} \ (radian^{-1}). \tag{2.13}$$

If four sources sample the stationary zone, which in practice is sufficient, the source density is

$$\rho_s = \frac{2}{cos^{-1}(1-\pi/kb)} \ (radian^{-1}). \tag{2.14}$$

Next, we show an application of the derived source density in a virtual source survey. The configuration of the survey is shown in figure 2.19. The sources are denoted by the stars and receivers as triangles. The receivers can be located in an horizontal well in an land survey, or at the ocean bottom in a marine survey. The target layer is at depth d_1 and receivers are at depth $d_1 - d_2$. The two receivers (r_A and r_B) to which interferometry is applied are separated by a distance l. What kind of source distribution is required to apply the interferometry in this configuration? If we use the target layer as a mirror, the configuration in figure 2.19 can be transfer to the one shown in figure 2.20. Term b in equations 2.11 and 2.13 becomes $\sqrt{4d_2^2 + l^2}$. Source radius r (distance from reflection point O to sources in the stationary phase zone) is $\sqrt{d_2^2 + l^2/4}d_1/d_2$. Apply these parameters to

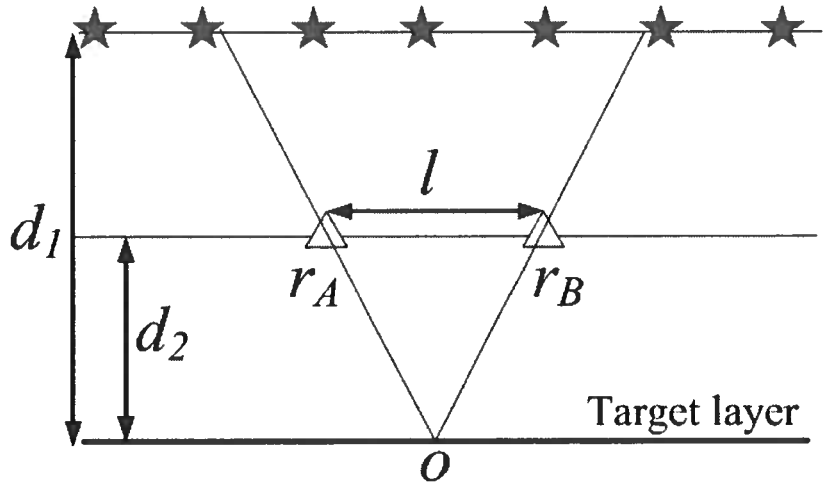

Figure 2.19. Source and receiver configuration of in an virtual source survey.

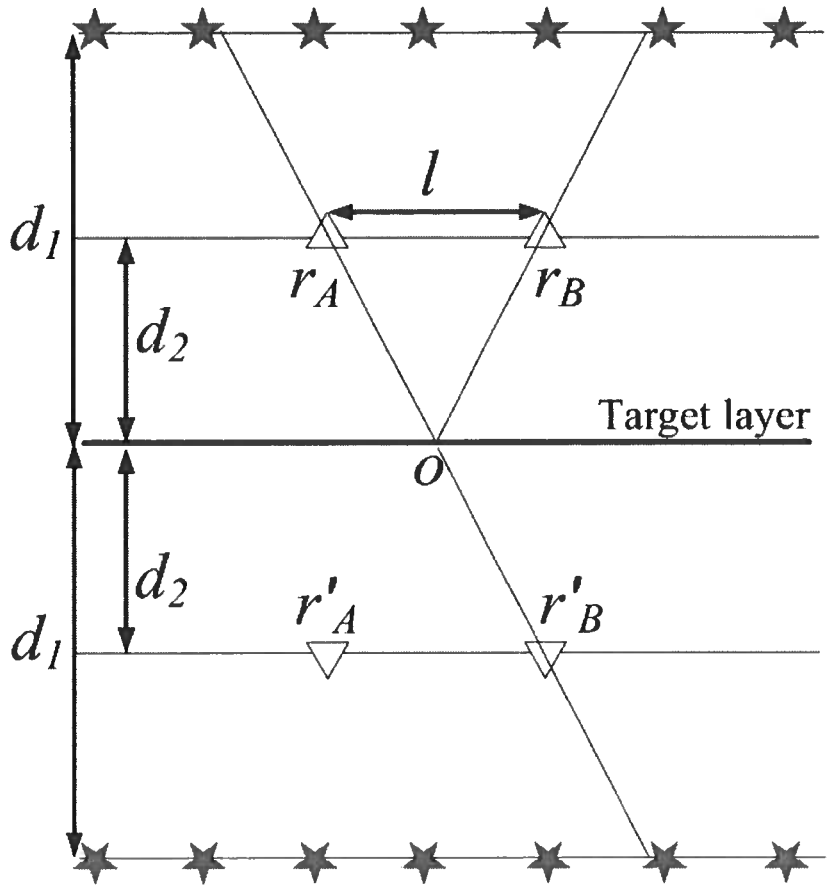

Figure 2.20. Source and receiver configuration of in an virtual source survey.

equation 2.12 and the source density on the surface becomes

$$dr = r\rho_s = \frac{0.8k(d_2^2 + l^2/4)d_1}{d_2} \ (m^{-1}). \tag{2.15}$$

This is the required source density if the contributions from the fastest oscillations in figure 2.17 must cancel. If only the sources in the stationary zone are used in the summation, equation 2.14 should be used and source density on the surface becomes

$$dr = \frac{d_1\sqrt{4d_2^2 + l^2}}{d_2 cos^{-1}(1 - \pi/(k\sqrt{4d_2^2 + l^2}))} \ (m^{-1}). \tag{2.16}$$

In conclusion, for wave interferometry in a homogeneous model, the most important parameter is the source angle distribution. If we know the source distribution, and hence the source angle, different weighting of the sources can be used to more accurately replace the integral over sources by a sum over sources. If randomly distributed sources are used and there is no information on the source angle distribution, the average of a large amount of extracted signals is more accurate to describe the real response than a single extracted signal.

This conclusion holds when all sources have the same amplitude. If the amplitude of the sources fluctuates randomly, a uniform angle distribution gives similar reconstruction of the Green's function as the random angle distribution for a constant source strength.

2.4.2 Waves in Heterogeneous Media

I find that one single source never gives an accurate Green's function reconstruction in the open scattering medium used in the example (see figure 2.11). In contrast, a dense source distribution is still needed in this strongly scattering medium. In my numerical experiment 140 uniformly distributed sources are enough to reconstruct the Green's function accurately if the scatterers are absent (homogeneous medium). This number is consistent with the criterion of expression 2.12. This suggests that more sources are needed to reconstruct the full

Green's function accurately for this heterogeneous medium (300 sources) than the homogeneous medium with the same parameters (140 sources). This contradicts the common notion that the heterogeneity around the receivers would reduce the required number of sources. When the wave propagation is equipartitioned in the heterogeneous medium (propagation path >> transport mean free path l_*), the wave field is diffusive. Cross-correlating these diffusive fields at two receiver locations is believed to give the Green's function between two locations (Lobkis & Weaver, 2001). Because of the equipartitioning one might think that the source distribution should not matter. This is not what we observe in my numerical experiment (figure 2.11), as 200 isotropic scatters in my experiment suffice to produce equipartitioning.

The optical theorem states that the total scattering cross section in 2-D medium can be represented as $\sigma = -\mathtt{Im}A/k_0$ (Groenenboom & Snieder, 1995), in which $\mathtt{Im}A$ is the imaginary component of the forward scattering amplitude A and k_0 is the wave vector in the background medium. For isotropic scatters, the imaginary component of A is restricted by $-4 \leq \mathtt{Im}A \leq 0$ because of the energy conservation (Groenenboom & Snieder, 1995). In my numerical experiment, $\mathtt{Im}A$ is chosen to be -3.99 to give strong scattering. For isotropic scatterers, the transport mean free path l_* is equal to the scattering mean free path (Ishimaru, 1997). The scattering mean free path is given by $l_s = 1/(N\sigma)$, in which N is the density of scatterers (Sheng, 1990). Using these expressions, the transport mean free path in my 200 isotropic scatterers area is about 5 m and the transport mean free time is about 3 ms. As the shortest propagation path in the heterogeneous area from a source to a receiver is 30 m, the earliest signal arrives at the receivers has propagated 6 mean free path in the heterogeneous area; therefore the energy flow associated with wave propagation is very close to being equipartitioned. We also cross correlated the later part of the signal (later than 50 mean free times) but the cross-correlation does not give the full Green's function at all with the 300 random sources. This raises a fundamental question: is equipationing a necessary condition in Green's function reconstruction, or is it a sufficient

condition? Our experiment suggests that equipartitioning is necessary but not sufficient. A source distribution with a sufficiently large aperture and source density is still important to retrieve the full Green's function.

Another question is how one can understand that more sources are needed in this heterogeneous medium than that in the homogeneous one? To answer this question, we show in figure 2.21 a medium with heterogeneity (scatterers) around the receivers. The stars are sources and triangles are receivers. The gray part represents the heterogeneous area. The signal recorded at each receiver is the superposition of wavefields from all possible scattering paths. First, consider one possible path of wave propagation from source S to receiver A. The wave hits the first scatterer (not necessary to be a scatterer on the boundary of the heterogeneous area) after a propagation distance L_A and then propagates to receiver A in the heterogeneous part in a complicated path with a propagation distance P_A. The dashed lines in figure 2.21 means that one does not know the exact path from the first scatterer to the receivers. Another possible path from source S to receiver B is also shown in the same manner. When we cross-correlate these two fields received at A and B from source S, the phase of the cross-correlation is $\phi = k(L_A - L_B) + (\phi_A - \phi_B)$, in which k is the wave numbers in the homogeneous area, ϕ_A and ϕ_B are the phase shifts along the paths P_A and P_B, respectively. When the source is moved with a small step from S to S$'$, the propagation paths in the heterogeneous area P_A and P_B stay the same while the paths in the homogeneous part changed to L'_A and L'_B. The phase of the cross-correlation becomes $\phi' = k(L'_A - L'_B) + (\phi_A - \phi_B)$. Therefore, the phase change of the cross-correlation when the source is moved from S to S$'$ is $\Delta\phi = k(L'_A - L_A) - k(L'_B - L_B)$. We can quantify this phase change using the parameters shown in figure 2.22. The angle between the path from the source to the first scatterers and the source radius r is defined as α. From the geometry of figure 2.22, we obtain $L'_A - L_A = dr sin\alpha_A$. Similarly we can get $L'_B - L_B = -dr sin\alpha_B$. Therefore, the phase change is given by

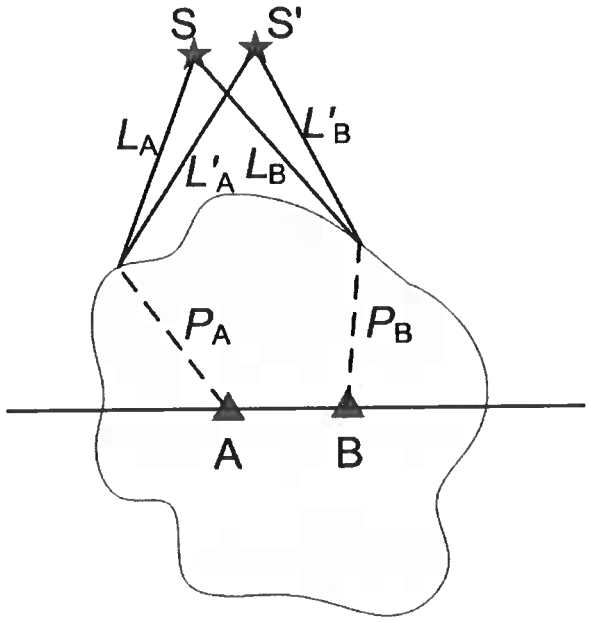

Figure 2.21. The configuration of wave propagation with receivers in a heterogeneous area.

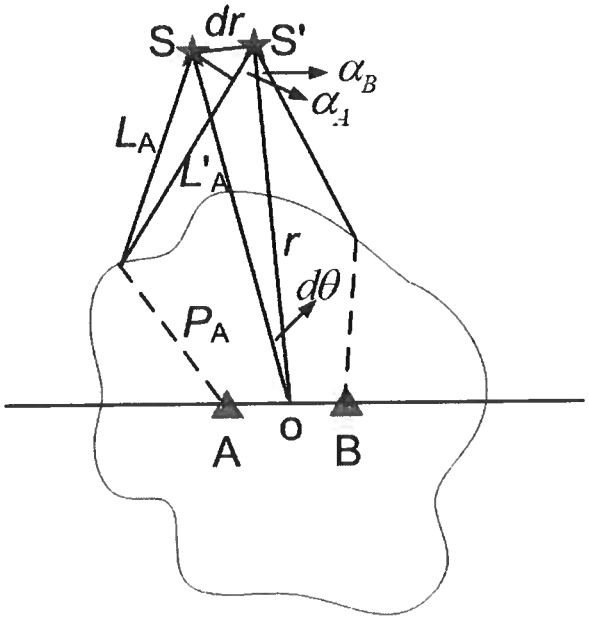

Figure 2.22. Parameters used to quantify the phase change in cross-correlation

$$\Delta\phi = k(sin\alpha_A + sin\alpha_B)dr, \tag{2.17}$$

In order to avoid aliasing, this phase change should be smaller than $\pi/2$. Consequently, we obtain the following criterion for the source separation

$$dr \leq \frac{\pi}{2k(sin\alpha_A + sin\alpha_B)}, \tag{2.18}$$

Applying $k = 2\pi/\lambda$, the criterion becomes

$$dr \leq \frac{\lambda}{sin\alpha_A + sin\alpha_B}, \tag{2.19}$$

Equation 2.19 shows that the source density is controlled by the size and position of the heterogeneous area with respect to the source position, rather than by the heterogeneity itself. When heterogeneity appears around the receivers, the maximum angle between the source radius and the path from the source to the first scatterer becomes larger. In equation 2.19, it means $\alpha_{A,B}$ increases. Consequently, the required source separation dr needs to be smaller than that for homogeneous medium. Therefore more sources are needed for the heterogeneous medium than for the homogeneous one.

If one is interested in the direct arrival Green's function only, the requirement of the source distribution can be relaxed. For example, Malcolm et al. (2004) showed that the ensemble-averaged Green's function in a granite can be retrieved from a single source by averaging over a pair of receivers with constant offset. The low frequency component of the direct surface wave Green's function has been retrieved from several irregularly distributed earthquakes (Campillo & Paul, 2003). However, the full Green's function is not retrieved in those studies. One interesting study shows that in a layered model with enough horizontal layers to give strong scattering and refraction, the full Green's function can be reconstructed by one-sided illumination with sources uniformly distributed on the free surface (Wapenaar, 2006a). In his 1-D layered model with normal-incident plane wave, the subsurface acts like

a mirror when the heterogeneity of the layers is strong enough, with the result that sources on one side suffice for the Green's function reconstruction.

2.4.3 Diffusion

The frequency domain Green's function of the diffusion equation in a 1-D homogeneous medium is given by

$$G^{1D}(x,\omega) = \frac{1}{(1+i)\sqrt{2\omega D}} e^{(-1-i)x\sqrt{\omega/2D}} \tag{2.20}$$

Inserting this expression into equation (2.4), gives

$$G(\mathbf{r}_A,\mathbf{r}_B,\omega) - G^*(\mathbf{r}_A,\mathbf{r}_B,\omega) = \frac{i}{2D}\int_x e^{-(r_{SA}+r_{SB})\sqrt{\omega/2D}} e^{-i(r_{SA}-r_{SB})\sqrt{\omega/2D}} dx \tag{2.21}$$

in which r_{SA} and r_{SB} are the distances between the source to the receiver A and B, respectively. Similar as for the analysis of the waves, we study the real part of the integrand of equation (2.21) as a function of source position x. Notice that the integrand is a function of frequency ω. Figure 2.23 shows the real part of this integrand for two different frequencies. The width of the distribution decreases with frequency. Qualitatively we can conclude that because the early-time behavior of the Green's function has more high-frequency components, the required source distribution can be narrower. This explains experiment 1 of the diffusion part: with small W_s, the early-time behavior is reconstructed well. With increasing W_s, more lower frequency components are recovered. Since the tail of the Green's function mostly contains low frequencies, the late-time Green's function is recovered accurately with a large width W_s. Consequently, the source density ρ_s controls the retrieval of the high-frequency components of the Green's function (eg. early-time of the Green's function), and the width of the distribution W_s controls lower frequency components (e.g. the late-time of the Green's function).

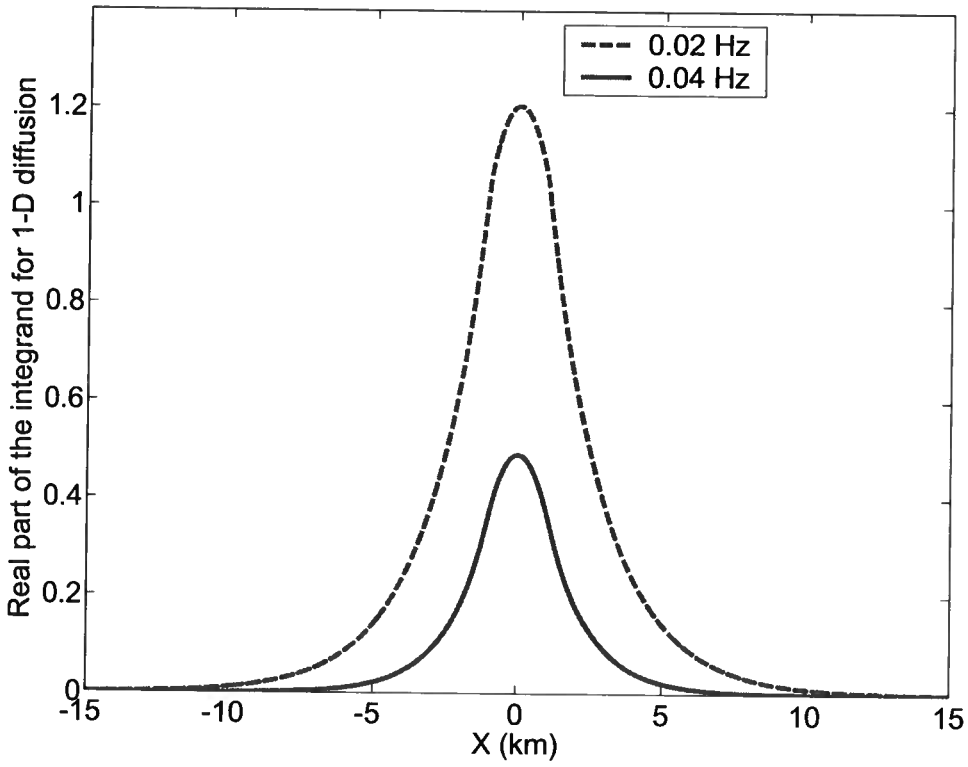

Figure 2.23. The real part of the integrand in equation (2.21) at two different frequencies.

The frequency domain Green's function for diffusion in 3-D is

$$G^{3D}(r,\omega) = \frac{1}{4\pi D r} e^{(-1-i)r\sqrt{\omega/2D}} \tag{2.22}$$

Inserting this into equation (2.4) we obtain

$$\begin{aligned} &G(\mathbf{r}_A,\mathbf{r}_B,\omega) - G^*(\mathbf{r}_A,\mathbf{r}_B,\omega) = \\ &\quad 2i\omega \int_V \frac{1}{(4\pi D)^2 r_{SA} r_{SB}} \\ &\quad e^{-(r_{SA}+r_{SB})\sqrt{\omega/2D}} e^{-i(r_{SA}-r_{SB})\sqrt{\omega/2D}} dV \end{aligned} \tag{2.23}$$

The integrand of equation 2.23 has two singularities at the receiver positions where r_{SA} and r_{SB} vanish. The integrand in equation 2.23 is largest for the sources near the receivers. In fact, it has an integrable singularity. One needs to integrate over this singularity to retrieve the exact Green's function since the integrand of equation 2.23 itself is not equal to the Green's function.

I next address the question how to quantify the required source distribution width W_s and source density ρ_s. As we learned from the examples in the diffusion part, W_s determines the late-time reconstruction of the Green's function. We define τ_a to be the time up to which we want to reconstruct the Green's function accurately. Sources within a source-receiver distance $r_{max}^2/(4D\tau_a) = 1$ give the largest contribution (Mehrer, 2007). Therefore, the required W_s should be

$$W_s = 4\sqrt{D\tau_a} + b \tag{2.24}$$

for an accurate reconstruction up to time τ_a, in which b is the distance between the two receivers. I define the error as the ratio of the difference between the exact and extracted signals to the exact signal at time τ_a. The error is less than 5% with W_s from the criterion 2.24.

The source density ρ_s controls the early-time reconstruction. In other words, it determines the accuracy of the reconstruction for the high-frequency components. For the maximum frequency f_m in the problem – either the highest frequency component of the Green's function itself or the maximum frequency of the source function – there is a sensitivity function of source position. This sensitivity is controlled by the decay factor $e^{-(r_{SA}+r_{SB})\sqrt{\omega/2D}}$ as shown in equations (2.21) and (2.23). The $1/e$ width of this sensitivity function is:

$$\sigma = \sqrt{2D/\omega} \tag{2.25}$$

Then if N_r is the number of sources needed in this range σ to estimate the integral accurately, the required source density is:

$$\rho_{sa} = N_r \sqrt{\omega/2D} \tag{2.26}$$

Based on the numerical examples, when N_r is larger than 2, the early-time response is reconstructed accurately. Then criterion (2.26) becomes:

$$\rho_{sa} = 2\sqrt{\omega/2D} \tag{2.27}$$

I can estimate the maximum frequency component in the Green's function as $1/(4t_p)$, in which t_p is the arrival time of the amplitude peak in the Green's function. We define the error as the ratio of the difference between the exact and extracted signals to the exact signal at time $t_p/2$. The error is less than 5% with source density from the criterion in equation 2.27.

In conclusion, for cross-correlation-based diffusion interferometry, instead of having sources everywhere in the volume, it suffices to have sources in only a small volume surrounding the receivers. For the 1-D problem, the source distribution width controls the late-time (low-frequency components) reconstruction of the Green's function and source density controls the early-time (high-frequency components) reconstruction. For the 3-D

problem, sources should not be located too close to the receivers position because of the singularities at those points.

2.5 Conclusion

Cross-correlation-based interferometry used to extract the Green's function which describes the field propagation between two receivers can be applied to the solution of both the wave equation and the diffusion equation. The main difference is the required source distribution.

For wave interferometry in a homogeneous medium, the source angle distribution is the most important parameter. With the assumption that the source radii are much larger than the distance between the two receivers, the variation in the source radius has a negligible effect, and the interferometry problem can be represented by a numerical integral of an oscillatory function of source angle. If cross-correlations from different sources are simply added in the Green's function extraction, the uniform source angle distribution gives a high decay rate of the non-physical fluctuation as a function of number of sources (faster than N^{-10}). With the same number of sources, the random distribution gives much poorer Green's function reconstruction. The rate of the non-physical fluctuation decay is approximately N^{-1}. The decay rate of the smoothly angular varying distribution is between those of uniform and random distributions and depends on how smooth the source angle varies. The required source density is determined by the distance between the two receivers and the wavenumber.

For wave interferometry in a heterogeneous medium, one single source is not sufficient to give accurate reconstruction even the wavefield is equipartitioned. This suggests that equipartition is a necessary but not sufficient condition in the Green's function reconstruction. Besides, more sources are needed to reconstruct the full Green's function in an heterogeneous medium than that for an homogeneous medium. The required source density is determined by the position and size of the heterogeneous area with respect to the sources.

For diffusion interferometry in a homogeneous medium, although the study shows that

a finite number of sources suffice to reconstruct the Green's function, the cross-correlation-based interferometry is not applicable for real applications because the sources are required to be close to the receivers. For a 1-D model, the sensitivity of the sources decays from the center of the two receivers. The width of the distribution controls the late-time of the reconstructed Green's function while the source density controls the early-time of the reconstructed Green's function. For a 3-D model, the main properties are the same as for the 1-D problem. The important point is that the sources between the two receivers give most of the contribution and these source distributions are hard to realize in practice. Because the requirement on the source distribution for diffusion interferometry is difficult to match in practice, it is preferable to use multi-dimensional deconvolution methods instead of correlation for diffusive fields, such as low-frequency electromagnetic fields (Wapenaar *et al.*, 2008; Snieder *et al.*, 2009)

Chapter 3

3-D Controlled Source Electromagnetic (CSEM) interferometry by multidimensional deconvolution

3.1 Summary

Controlled Source Electromagnetics (CSEM) is an important technique in hydrocarbon exploration, because it uses the large contrast in electrical resistivity to distinguish between water and hydrocarbons. In a shallow sea environment, the airwave that is refracted from the air-water interface dominates the recorded signal at large offsets. Therefore, the hydrocarbon detection ability of the CSEM is weakened because the airwave is independent of the properties of the subsurface. We apply multi-dimensional-deconvolution interferometry to synthetic 3-D CSEM data and estimated the reflection response of the subsurface. The difference in the models with and without the reservoir is significantly increased by the employed interferometric analysis. However, the required receiver spacing for the up-down decomposition needed for multi-dimensional deconvolution is much denser than that of current CSEM surveys. In order to reduce the required receiver spatial density, we introduce the synthetic aperture technique to construct smoothly varying electromagnetic fields.

3.2 Basic Theory and History of Virtual Source Technique

The concept of *interferometry* was first introduced to the seismic community by Claerbout (1968). It became a hot research topic in geophysics in the last decade. The method is also referred to as the *virtual source technique* and in a wider sense as *Green's function*

reconstruction. In this work, we refer to the same technique using these three terms. For waves, the key idea of this technique is the following. The Green's function that describes wave propagation between two receivers can be reconstructed by cross-correlation of the wavefields at two receiver positions provided that the receivers are enclosed by uncorrelated sources on a closed surface. Because of the advantages of this technique and its use in passive surveys, research on seismic interferometry has progressed significantly during the last ten years (Lobkis & Weaver, 2001; Weaver & Lobkis, 2001; Derode *et al.*, 2003; Campillo & Paul, 2003; Weaver & Lobkis, 2004; Wapenaar, 2004; Snieder, 2004; Malcolm *et al.*, 2004; Bakulin & Calvert, 2004; Calvert *et al.*, 2004; Wapenaar *et al.*, 2005; Shapiro *et al.*, 2005; Roux *et al.*, 2005; Sabra *et al.*, 2005a,b; van Wijk, 2006; Larose *et al.*, 2006; Bakulin & Calvert, 2006; Snieder, 2007; Mehta & Snieder, 2008).

Snieder (2006b) showed that interferometry can be applied not only to wavefields, but also to diffusive fields. This discovery inspired further research and novel applications to diffusive fields, as has happened for wave fields. Diffusive fields have a wide range of applications and use in physics, chemistry, medical physics, earth science (Mandelis, 1984; Yodh & Chance, 1995; Basser *et al.*, 1994; Mori & Barkar, 1999; Koyama *et al.*, 2006; Constable & Srnka, 2007). In earth science, diffusive fields are ubiquitous. Examples include heat conduction, flow in porous media, and low-frequency electromagnetic fields in the conductive subsurface. In this work, we focus on the application of interferometry to low-frequency electromagnetic fields in the subsurface. However, one can extend the concept to other diffusive fields. Because the electromagnetic field is sensitive to the electric resistivity, it has been used in medical physics and the mining industry for a long time. In recent years, electromagnetic surveys became increasingly popular in the petroleum industry for hydrocarbon exploration because of its ability to distinguish the difference between hydrocarbons and water (Andréis & MacGregor, 2008; Lien & Mannseth, 2008). The technique is usually referred to as the Control Source Electromagnetics (CSEM). Seismic methods are not sensitive to the chemical content of pore fluids. By using a combination of seismic and CSEM

methods, the success of finding the hydrocarbon reservoir in the subsurface dramatically increases (Darnet *et al.*, 2007; Kwon & Snieder, 2010).

The theories of interferometry based on cross-correlation for waves and diffusion are similar but differ in the required source distribution. Interferometry for acoustic waves can be expressed as (Snieder *et al.*, 2007)

$$G(\mathbf{r}_A, \mathbf{r}_B, \omega) - G^*(\mathbf{r}_A, \mathbf{r}_B, \omega) = 2i\omega \oint_S \frac{1}{\rho c} G(\mathbf{r}_A, \mathbf{r}, \omega) G^*(\mathbf{r}_B, \mathbf{r}, \omega) dS, \tag{3.1}$$

in which $G(\mathbf{r}_A, \mathbf{r}_B, \omega)$ is the pressure Green's function caused by a volume injection that describes wave propagation from $\mathbf{r}_B$ to $\mathbf{r}_A$ respectively, $*$ indicates complex conjugation, S is the surface where sources are located, and ω is the angular frequency. For the case of diffusion interferometry the expression becomes

$$G(\mathbf{r}_A, \mathbf{r}_B, \omega) - G^*(\mathbf{r}_A, \mathbf{r}_B, \omega) = 2i\omega \int_V G(\mathbf{r}_A, \mathbf{r}, \omega) G^*(\mathbf{r}_B, \mathbf{r}, \omega) dV, \tag{3.2}$$

where V is the volume containing the sources. The main difference is that the surface integral in equation (3.1) becomes a volume integral in equation (3.2) (Snieder, 2006b). This volume integral implies that sources in the entire volume are required to reconstruct the Green's function. Fan & Snieder (2009) show that the sources in a small volume close to the two receivers give the largest contribution to the Green's function reconstruction. In practice, a finite number of sources is sufficient to reconstruct the Green's function. Criteria for the required source distribution are derived by Fan & Snieder (2009). However, it is still unpractical to apply cross-correlation-based interferometry to field recordings of diffusive fields, because sources close to the receivers are critical in this technique. The purpose of interferometry technique is to use a receiver both as a receiver and a virtual source. If real sources close to the receivers are required to do this, then one could just as well place a real

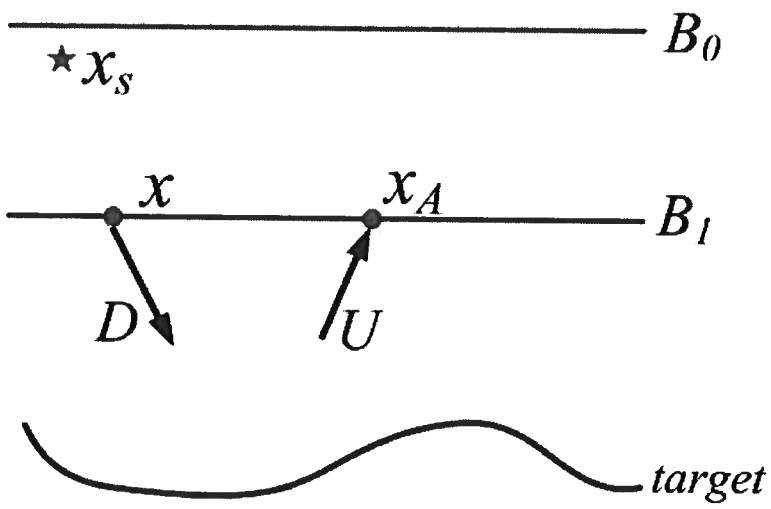

Figure 3.1. A generic configuration for the application of the multi-dimensional deconvolution interferometry concept.

source at the receiver position.

When the receivers are located in a plane and sources are placed above this plane, a multi-dimensional-deconvolution approach is applicable to a diffusion field (Amundsen *et al.*, 2006; Slob *et al.*, 2007; Wapenaar *et al.*, 2008). This approach works for both diffusion and waves. It also holds for any field which can be decomposed into upgoing and downgoing components. A generic geometry for this approach is sketched in Figure 3.1. The source is denoted by the star, and receivers are located on the plane B_1. B_0 is a boundary above the sources, which may or may not be present. D and U represent downgoing and upgoing fields at B_1, respectively. The upgoing and downgoing fields can be related with the following integral equation

$$U(x_A, x_s, \omega) = \int R(x_A, x, \omega) D(x, x_s, \omega) dx, \tag{3.3}$$

where $U(x_A, x_s, \omega)$ represents the upgoing field received at location x_A in the frequency domain due to the source at x_s. The downgoing field is noted by D, and $R(x_A, x, \omega)$ is the reflection response that relates the downgoing field at x to the upgoing field at x_A. Although

the entire medium can be arbitrarily heterogeneous in order to decompose the field into upgoing and downgoing components (Grimbergen *et al.*, 1998), the up-down decomposition operator can be simplified if the layer where receivers are located is homogeneous or weakly heterogeneous (Wapenaar *et al.*, 2008). Because the downgoing fields at all positions in the plane B_1 contribute to the upgoing field at position x_A, one needs to integrate x over the whole surface to obtain a complete upgoing field at x_A. The inversion of R from equation (3.3) is ill-posed because no unique R can be obtained from a downgoing field D and upgoing field U excited by a single source. If a source at another position $x_{s'}$ is used, a different pair of U and D is obtained from the decomposition. The medium response R, however, remains the same because it is independent on the source position. This means that the more sources are used, the more constraints there are on the inversion of R. Therefore, a band-limited medium response R can be accurately inverted from a band-limited input signal, if a sufficient number of sources are used.

A discretized version of equation (3.3) may help to illustrate the importance of multiple sources. Equation (3.4) is a discretized version of equation (3.3) for a single source at x_s

$$\begin{pmatrix} U_1 \\ U_2 \\ \vdots \\ U_n \end{pmatrix} = \begin{pmatrix} R_{11} & R_{12} & \cdots & R_{1n} \\ R_{21} & \cdots & \cdots & \cdots \\ \cdots & \cdots & \cdots & \cdots \\ R_{n1} & \cdots & \cdots & R_{nn} \end{pmatrix} \begin{pmatrix} D_1 \\ D_2 \\ \vdots \\ D_n \end{pmatrix}, \tag{3.4}$$

where the subscripts 1 through n of U and D are the discretized sampling points of the surface B_1, R_{ij} denotes the reflection response between the positions i and j. The arrays of U and D are the measured data and R is the unknown matrix. In general, there is no unique solution for matrix R because there are more unknowns (n^2) than the number of equation (n). Using reciprocity, the number of unknowns can be reduced to $n(n+1)/2$. The expression below is a similar equation but combines sources at position x_s and another

position $x_{s'}$

$$\begin{pmatrix} U_1,\ U_1' \\ U_2,\ U_2' \\ \vdots \\ U_n,\ U_n' \end{pmatrix} = \begin{pmatrix} R_{11}\ R_{12}\ \cdots\ R_{1n} \\ R_{21}\ \cdots\ \cdots\ \cdots \\ \cdots\ \cdots\ \cdots\ \cdots \\ R_{n1}\ \cdots\ \cdots\ R_{nn} \end{pmatrix} \begin{pmatrix} D_1,\ D_1' \\ D_2,\ D_2' \\ \vdots \\ D_n,\ D_n' \end{pmatrix}, \tag{3.5}$$

where U' and D' are the new upgoing and downgoing fields generated by the source at position $x_{s'}$. The matrix R remains the same as it is independent of the source. By increasing the number of sources, the number of columns in U and D increases. The matrix R can be accurately estimated if a sufficient number of sources are used.

When discretizing equation (3.3), only a finite number of the receivers from a limited range of the surface B_1 can be used. This raises the question how to choose the receiver distribution in order to represent the integral in equation (3.3) accurately for a band-limited response R?

3.3 Why Apply Interferometry in Marine CSEM?

Figure 3.2 shows a typical configuration of an offshore marine CSEM survey. A resistive target (e.g. hydrocarbon reservoir) in the subsurface, acts as a secondary source that generates an upgoing EM field. We can distinguish between models with and without the reservoir from the secondary fields which the subsurface generates. The large difference in the electrical resistivity between water and hydrocarbons makes CSEM a useful tool to distinguish between these pore fluids. Most of the current successful applications of CSEM are offshore because the water strongly attenuates anthropogenic and natural noise. However, one of the most significant problems in offshore CSEM is the airwave when the water layer is shallow. The airwave is the secondary EM field refracted from the water-air interface as shown in figure 3.2. The airwave weakens the difference between the signal with a reservoir and the signal without a reservoir because it is much stronger than the target signal.

With multi-dimension-deconvolution interferometry, as described in the last section,

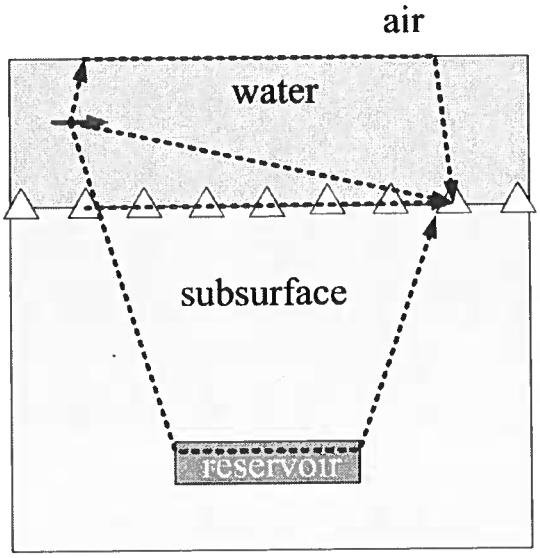

Figure 3.2. A simple configuration of a offshore CSEM survey and possible field propagation paths (dashed arrows). The solid arrow denotes the dipole source and the triangles are the ocean bottom receivers.

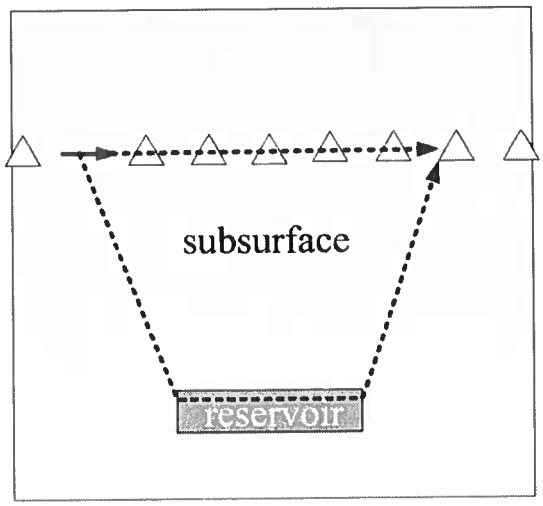

Figure 3.3. The configuration of CSEM after the application of the multi-dimensional-deconvolution interferometry.

one of the receivers is converted into a source and the overburden is extended upwards to a homogeneous half space (Wapenaar *et al.*, 2008). The new configuration after applying this technique is shown in figure 3.3. In this configuration, the imprint of the air-water interface and the sea floor on the electromagnetic field is removed. Note that the sea floor interface may or may not be removed depending on the boundary condition which we use in the decomposition process. Therefore, by applying this interferometry technique to CSEM data, the airwave problem is solved and the complexity of the media above receivers is removed as well. Consequently, the secondary field is generated only by the subsurface and therefore it is easier and more accurate to detect the properties of a target. This significant improvement has been demonstrated in 2-D synthetic examples (Wapenaar *et al.*, 2008; Hunziker *et al.*, 2009).

3.4 Synthetic Example for a 3-D Reservoir in Shallow Water

I first present a synthetic study of multi-dimensional-deconvolution interferometry for a 3-D marine CSEM survey. This synthetic study shows the feasibility of applying this technique to 3-D CSEM data and illustrates how this technique helps to detect the hydrocarbon reservoir. This study also provides the required receiver distribution.

Figure 3.4 shows the 3-D model used. Because both wave numbers in the x and y directions are required in the decomposition of upgoing and downgoing fields (Wapenaar *et al.*, 2008), and the surface integral in the equation (3.3) must be replaced by summation of receivers, a 2-D receiver array is used in the synthetic example as shown in figure 3.5. The uniformly sampled 2-D receiver array is on the sea floor from positions -10 km$< x <$10 km, -10 km$< y <$10 km with a receiver separation dr of 50 m in both x and y directions. The EM source (arrow in figure 3.5) is a dipole in the x direction with a length of 100 m and a AC current of 100 A and an operating frequency of 0.25 Hz. The source is located 100 m above the sea floor. The employed station spacing (50 m) is unrealistically dense, and we discuss a way to reduce the required receiver spatial density in the next section.

The measured E_x field is shown in figures 3.6. Figure 3.6(a) shows the E_x field without

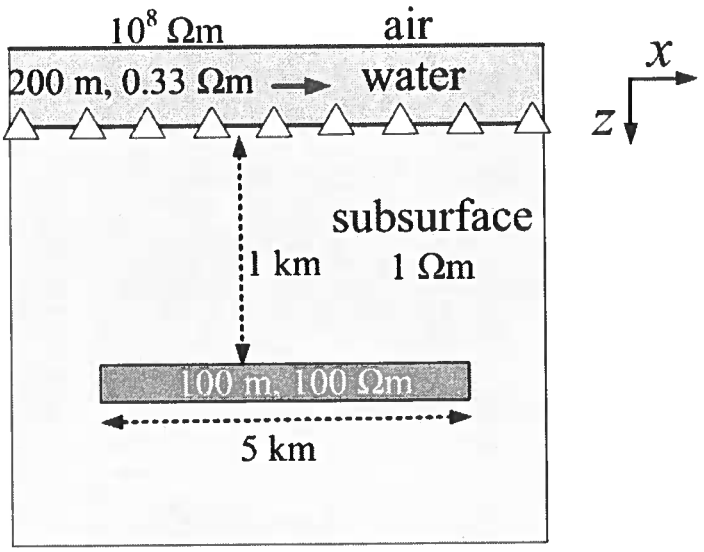

Figure 3.4. The 3-D model used in the synthetic example. The source is 100 m above the sea floor and the background subsurface is a homogeneous half space.

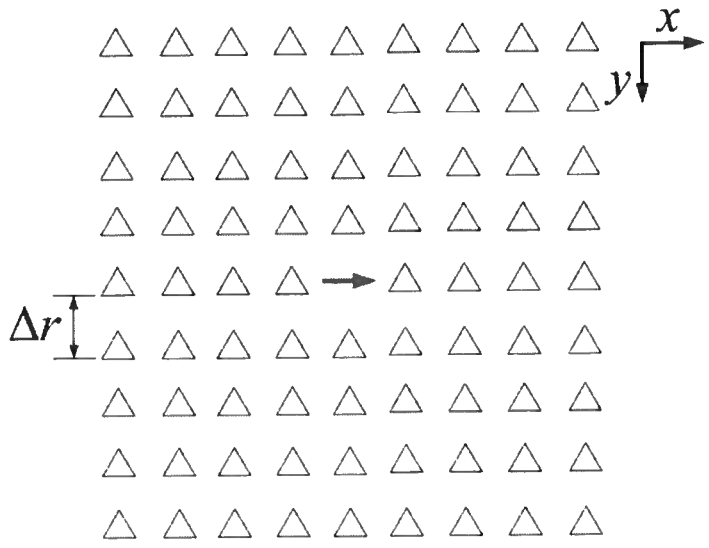

Figure 3.5. A map view of the 2-D receiver array used in the synthetic example.

the reservoir and figure 3.6(b) the E_x field with the reservoir. The difference of the total E_x field between the models with and without the target layer is small because the secondary E_x field from the reservoir is much weaker than the direct field or the airwave. In current CSEM surveys, it is common to use only the inline profile (receivers only locate on x-axis) of the E_x field because the signal to noise ratio is high and 3-D acquisition is more expensive. Figure 3.7 shows the inline profile of the E_x field. The solid curve is the field without the reservoir and the dashed curve is the field with the reservoir. For small offsets (< 2 km), there is almost no difference between these two curves because the direct field dominates. For large offsets (> 7 km), the electric field is strongly influenced by the airwave, which does not depend on the subsurface properties at all. Consequently, targets leave a useful imprint only for intermediate offsets (2km to 7km). Because this intermediate range is narrow and the difference between the signals with and without target is weak, it is difficult to interpret the difference between the signals with and without the target, especially in the presence of noise.

We next apply multi-dimensional-deconvolution interferometry to the measured electromagnetic field. The first step of this technique is to decompose the total field into upgoing and downgoing components. The implementation of the up-down decomposition follows the theory in the appendix of Wapenaar *et al.* (2008). This decomposition writes the total fields as the superposition of flux-normalized upgoing and downgoing fields. The input data used in the decomposition are the horizontal E and H fields. The measured electric and magnetic fields can be related with the upgoing and downgoing flux by

$$P(k_x, k_y) = L^{-1}(k_x, k_y)\, Q(k_x, k_y) \tag{3.6}$$

where P is the decomposed upgoing and downgoing potential, normalized to energy flux, Q contains the input horizontal E and H fields and L^{-1} is the conversion operator. Wapenaar *et al.* (2008) show a numerical example for a 2-D field with a layered model. With an

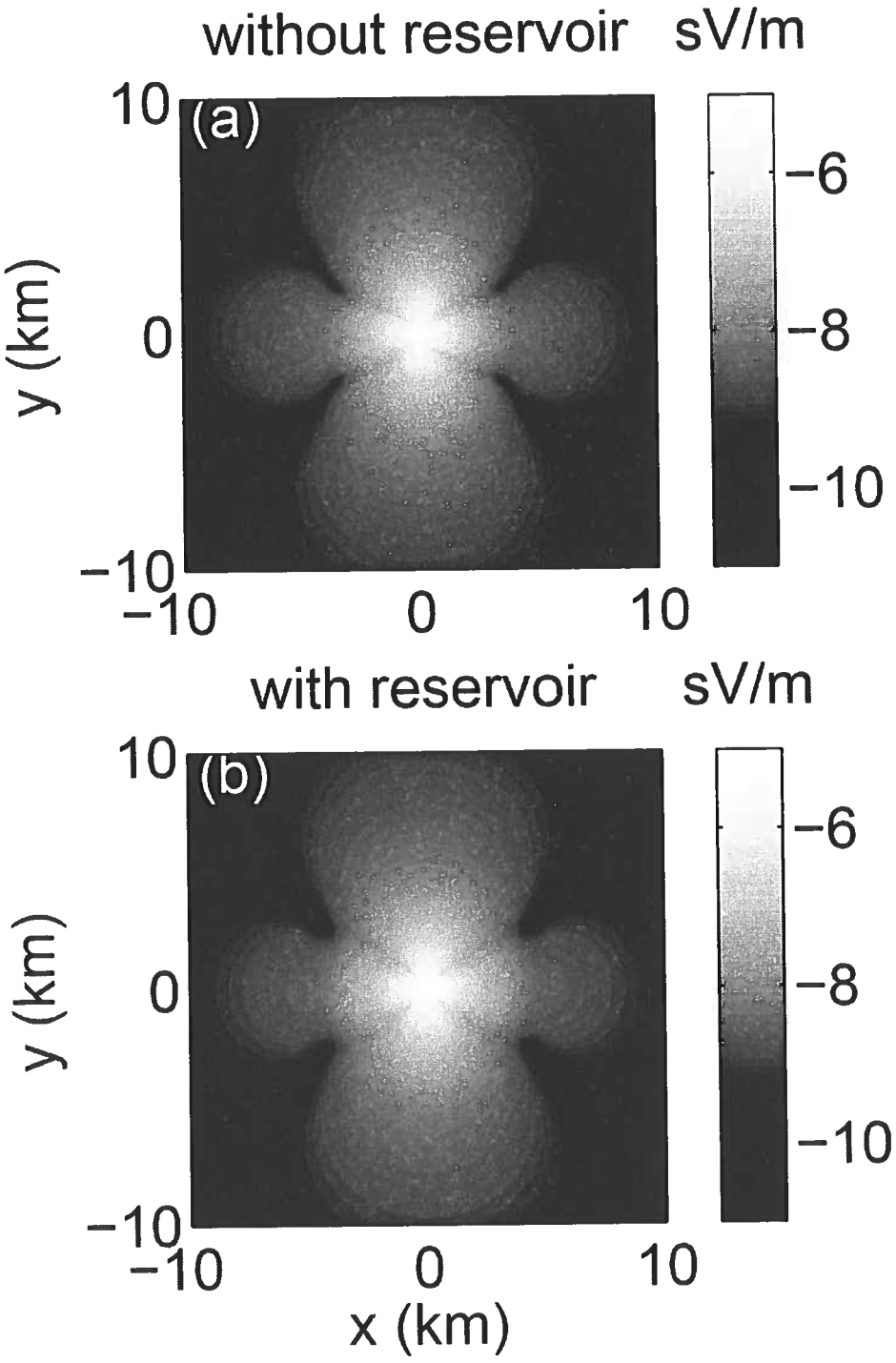

Figure 3.6. E_x field without (a) and with (b) the reservoir on a log10 scale.

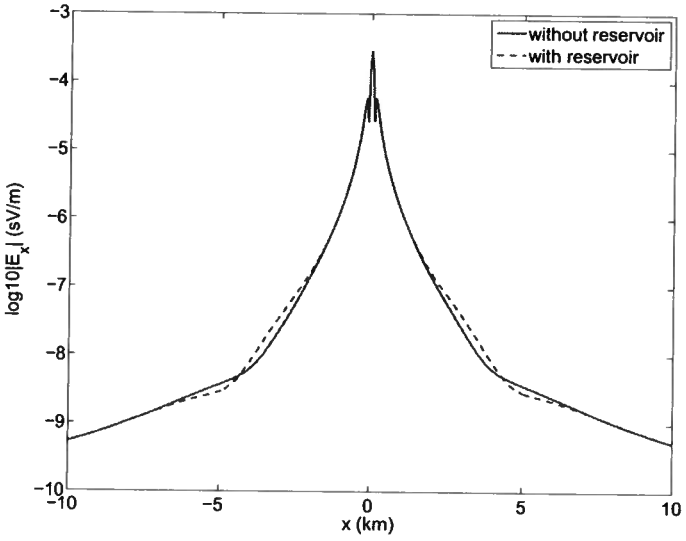

Figure 3.7. The inline profile of the E_x field on a log10 scale.

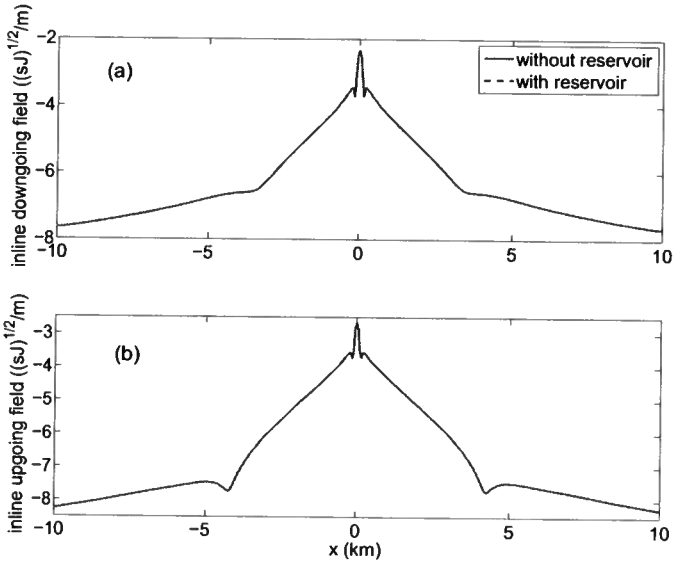

Figure 3.8. The inline profile on a log10 scale of the downgoing fields (a) and upgoing fields (b) with (dashed lines) and without (solid lines) the reservoir using parameters values for sea water in the operator L.

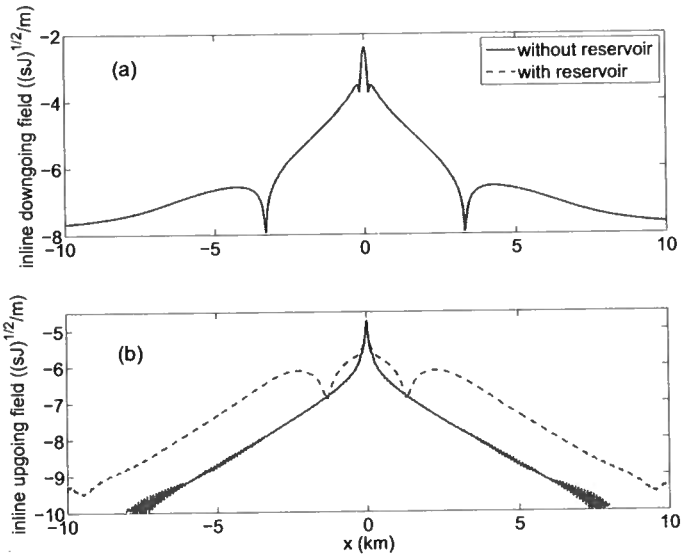

Figure 3.9. The inline profile on a log10 scale of the downgoing fields (a) and upgoing fields (b) with (dashed lines) and without (solid lines) the reservoir using parameters values for sea floor in the operator L.

inline dipole source, the physical meaning of $P = [P_d, P_u]'$ is the decomposed energy flux of the TM (transverse magnetic) mode (subscripts d and u denote downgoing and upgoing, respectively). The downgoing field is defined as the field which decays downwards and the upgoing field is defined as the field which decays upwards.

In our synthetic example, the field is 3D, hence Q contains four components E_x, E_y, H_x, H_y and P has four components as well $[P_d^1, P_u^1, P_d^2, P_u^2]$. Because the receivers are located at the boundary of the water and the sea floor, we can choose the parameters for L^{-1} either from the upper medium (water) or the lower medium (sea floor). These two choices lead to different physical meanings for the decomposed field. Using the water parameters for the up-down decomposition, we obtain the upgoing and downgoing fields in the water just above the sea bottom. If the sea floor parameters are used, we obtain the upgoing and downgoing fields in the sea bottom just below the acquisition surface. Figures 3.8 and 3.9 compare the

upoing and downgoing fields for these two choices. For demonstration purposes, only the inline profile of the fields is shown. When the water parameters are used in the decomposition, we obtain the same downgoing fields for the models with and without the reservoir, as we expected (figure 3.8(a)). Surprisingly, we also do not see any difference in the upgoing field (figure 3.8(b)). This is because in this case the upgoing field is dominated by the reflected or refracted field from the sea floor interface. Because the water is shallow, these upgoing fields from the sea floor interface caused by the direct field and airwave are still much stronger than the upgoing secondary field from the reservoir.

When the sea floor parameters are used in the decomposition, the downgoing fields (figure 3.9(a)) are still the same for the models with and without the reservoir. The upgoing fields (figure 3.9(b)) highlight the difference between the models with and without the reservoir because the upgoing field in the sea floor is mainly from the target in the subsurface.

After decomposing the energy flux into upgoing and downgoing components, we calculate the impulse response of the subsurface using equation (3.3). This is a multi-dimensional-deconvolution problem to compute R from U and D. As illustrated in equation (3.4) and (3.5), the retrieving of R from a single source data is ill-posed. In order to accurately compute matrix R, decomposed field from more sources are required according to equation (3.5). The required number of sources should be larger or equal to the number of the receivers . Because the horizontal extension of the reservoir in my model is large (5 km), we approximately treat my 3-D model as a layered earth model. In this approximate layered earth model, the impulse response only depends on the relative position $(x - x', y - y')$, so we can rewrite equation (3.3) as

$$U(x, y) = \int R(x - x', y - y')D(x' - x_s, y' - y_s)dx'dy'. \tag{3.7}$$

The angular frequency ω is not shown in the equation. Equation (3.7) presents a spatial convolution. In the wave-number domain, we can present spatial convolution in equation

(3.7) by multiplication as

$$U(k_x, k_y) = R(k_x, k_y)D(k_x, k_y). \tag{3.8}$$

Consequently, R can be obtained by a division in the wave number domain. To stabilize this process, the devision is modified in the following way.

$$R(k) = \frac{U(k)D^*(k)}{D(k)D^*(k) + \epsilon^2 \frac{\sum_{k'} D(k')D^*(k')}{N_{k'}}}, \tag{3.9}$$

where ϵ is a small number to stabilize the division and $N_{k'}$ is the number of discrete wave numbers used in the calculation. We used $\epsilon = 0.2$.

The up and downgoing fields in the sea floor, whose inline profiles are shown in figure 3.9, are used in equation (3.9) to calculate the impulse response. The calculated impulse response is shown in figure 3.10(a) (without the reservoir) and figure 3.10(b) (with the reservoir). The difference of the impulse response is significant between the models with and without the reservoir. Comparing with the inline profile of the total E_x field (figure 3.7), the inline profile of the impulse response (figure 3.11) gives a much more pronounced difference between the models with and without the reservoir.

3.5 Reducing the Required Receiver Spacing Using Synthetic Aperture

Although we have shown that multi-dimensional deconvolution interferometry can significantly increase the imprint of the reservoir, the required receiver spatial density makes it difficult to apply to current CSEM surveys. In the synthetic example, we used an array of 400 by 400 (160000) receivers as illustrated by figure 3.5. This unrealistically large number of receivers can not be realized in field experiments. Furthermore, the number of receivers also affects the required number of sources when calculating the matrix R. In a real CSEM survey, receivers are normally distributed in a line instead of a 2-D array and the spacing between the receivers is about 1 km, which is much larger than the spacing used here. Next,

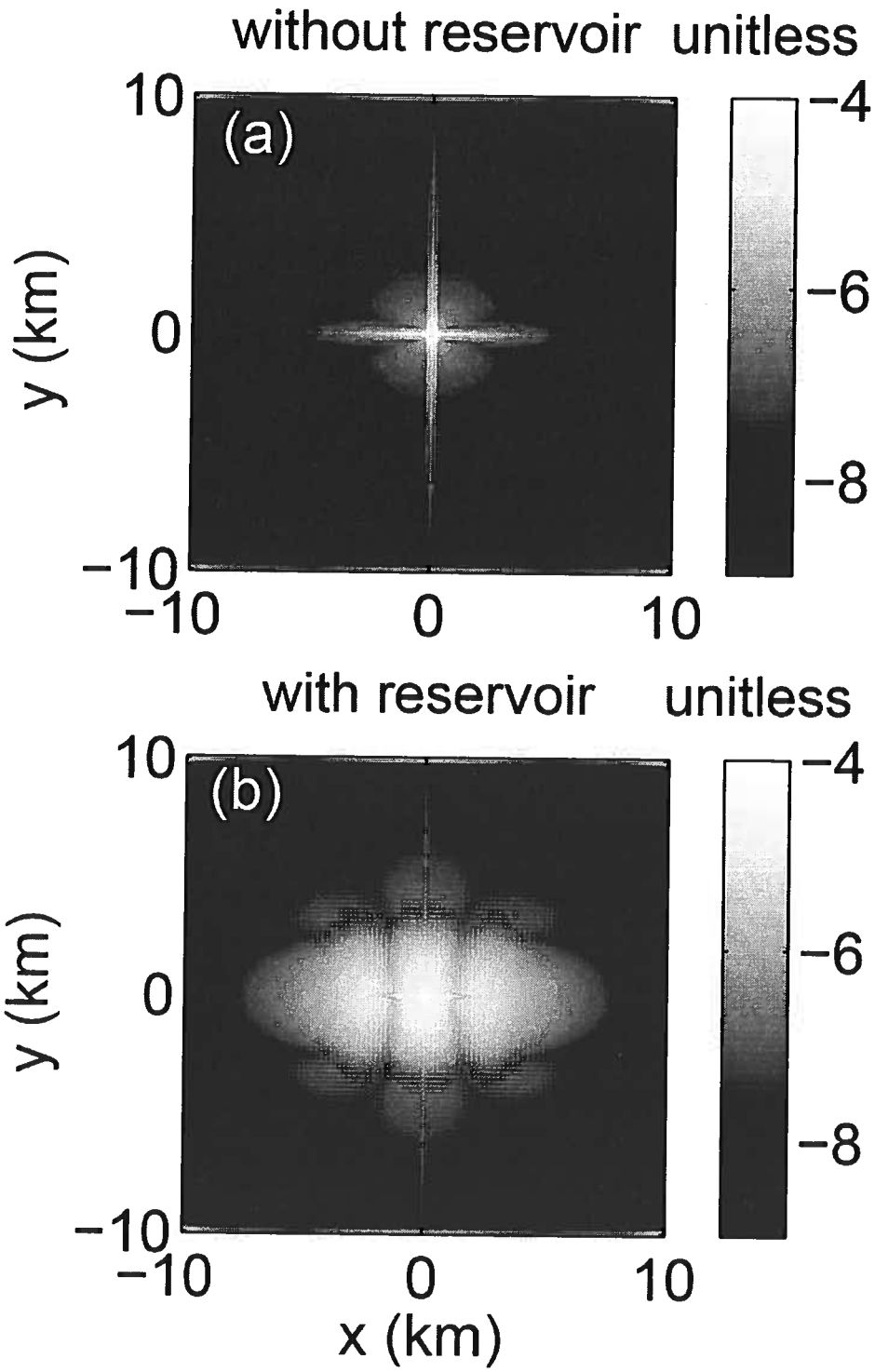

Figure 3.10. The impulse reflection response R without (a) and with (b) the reservoir on a log10 scale.

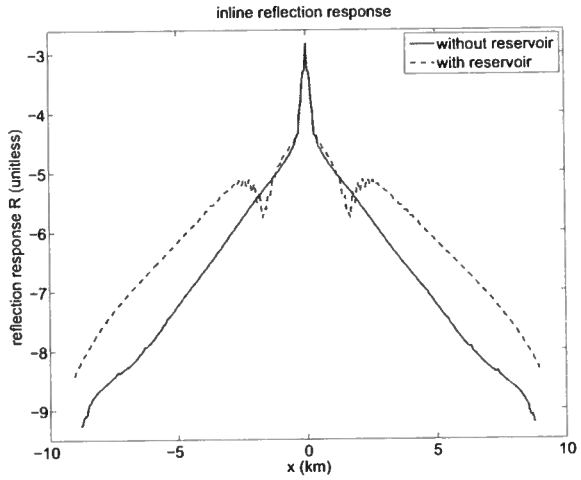

Figure 3.11. The inline profile of the reflection response R on a log10 scale

we investigate the consequences of ignoring the crossline dimension in CSEM data in the up-down decomposition.

First, what happens if we only have a line of receivers available? we can approximately decompose the field into upgoing and downgoing components by ignoring the variation of the field in the crossline direction. This is equivalent to setting k_y=0 in equation (3.6). Figure 3.12 shows the comparison of the 2-D (using receivers on x-axis) and 3-D (using all receivers in the array) decomposition for the model used above. Figure 3.12(a) shows the downgoing fields and figure 3.12(b) shows the upgoing fields. The solid lines and dashed lines represent the 3-D and 2-D decomposition, respectively. Because the crossline variation of the field is missing, the decomposed fields using a line of receivers are not accurate and the discrepancy in the upgoing field is larger than that in the downgoing field. The 2-D decomposed fields, however, still have the imprint of the reservoir as shown in figure 3.13. The solid lines in figure 3.13 are the downgoing (a) and upgoing (b) fields without the reservoir using a 2-D decomposition. The dashed lines are the fields with the reservoir and the solid lines represent the fields without the reservoir. The downgoing fields (figure 3.13(a)) are similar

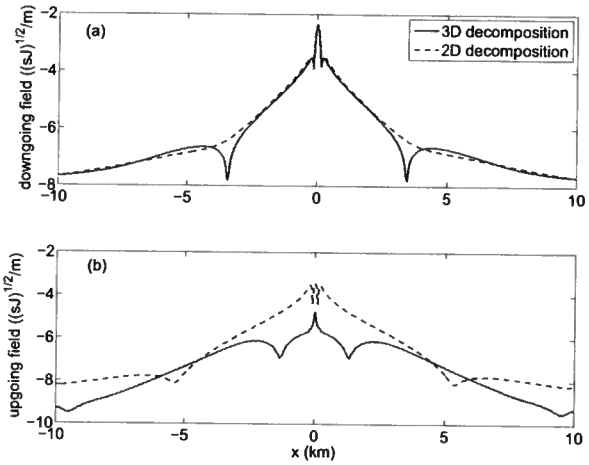

Figure 3.12. The comparison of the 2-D (dashed lines) and 3-D (solid lines) decompositions. Panel (a) shows the downgoing fields and (b) shows the upgoing fields.

for the models with and without the reservoir. The upgoing fields (figure 3.13(b)) clearly show the imprint of the reservoir, though the difference in the upgoing field using the 2-D decomposition is smaller than that using the 3-D decomposition (figure 3.9(b)).

What if we only have a sparse receiver distribution? The dense receiver distribution is mainly needed for the up-down decomposition. Because the up-down decomposition shown in equation 3.6 is a wave number domain operation, one needs to transform E and H fields to the wave number domain (Wapenaar *et al.*, 2008). Figure 3.14 shows the real part (Re) and imaginary part (Im) of the measured E_x and H_y fields recorded by the receivers on x-axis. Both the real and imaginary parts of E and H fields vary rapidly with space close to the source at x=0 km. Therefore, the dense receiver spacing is required to avoid aliasing in the x-k transform. In order to increase the required receiver spacing for the x-k transform, the input electric and magnetic fields used for the up-down decomposition need to be smoothly varying in space. One way to reduce the high wave number components in the fields is to use a much longer source. The large source can be either a physical long dipole or can be constructed by adding small sources using synthetic the aperture concept

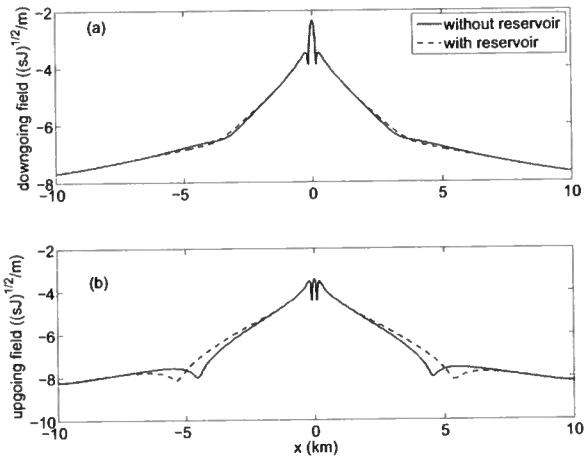

Figure 3.13. 2-D decomposed downgoing (a) and upgoing (b) fields for the models with (dashed lines) and without (solid lines) the reservoir.

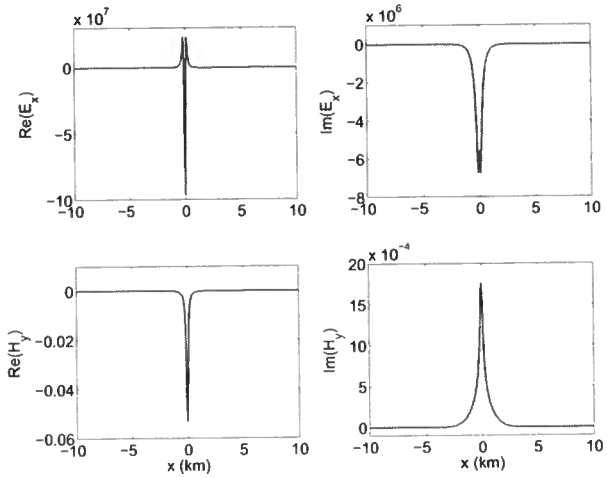

Figure 3.14. The real (Re) and imaginary (Im) parts of E_x and H_y fields for a 100 m long dipole.

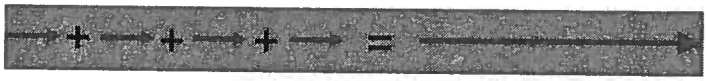

Figure 3.15. An illustration of the synthetic aperture concept: a large synthetic source can be constructed by adding small sources.

(illustrated by figure 3.15). The synthetic aperture technique has been popularly used in the radar community. Fan *et al.* (2010b) introduced this technique to CSEM data and show that the diffusive fields can be steered. Although there are many sophisticated ways to construct synthetic aperture source, here we only use the weighted summation to build large sources.

Figure 3.16 shows the real and imaginary parts of the E_x and H_y fields from a 10 km long dipole (from x=-5 km to x=5 km). Although these fields are smoother than those shown in figure 3.14, the real part of the E_x field contains rapid oscillations at the edges of the source. These rapid oscillations still require a dense receiver spacing in the x-k transform. Figure 3.16 suggests that with a large physical source, the required receiver spacing is still dense. For a synthetic aperture source, however, we can give different weight to the individual small sources to construct a smoother E_x field. I illustrate this by constructing a 10 km long dipole by adding 100 dipoles that are each 100 m long. Because the source is continuously moving in a CSEM survey, we have such spatially distributed small sources without any additional acquisition. To reduce the contribution from the edges of the large source, we use a Hann window function squared as defined by

$$w(n) = \frac{1}{4}(1 - \cos(\frac{2\pi n}{N-1}))^2, \tag{3.10}$$

where n is the index of the individual small sources and N is the total number of the sources used in the array (N=100 in this case). Figure 3.17 shows the fields from this weighted 10 km long synthetic source. Comparing with a physical 100 m dipole (figure 3.14) and a 10 km dipole (figure 3.16), the fields in figure 3.17 are much smoother and the high wave number

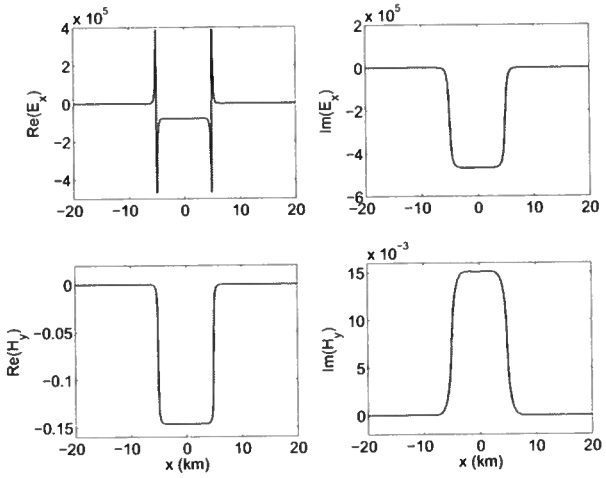

Figure 3.16. The real (Re) and imaginary (Im) parts of E_x and H_y fields for a 10 km long dipole.

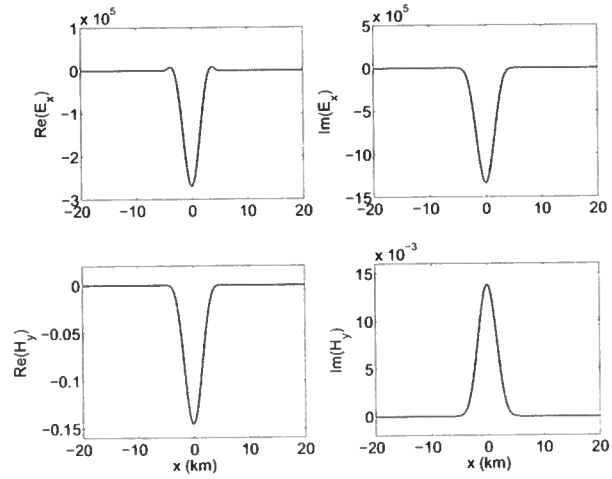

Figure 3.17. The real (Re) and imaginary (Im) parts of E_x and H_y fields for a synthetic 10 km long dipole that is weighted by a Hann window.

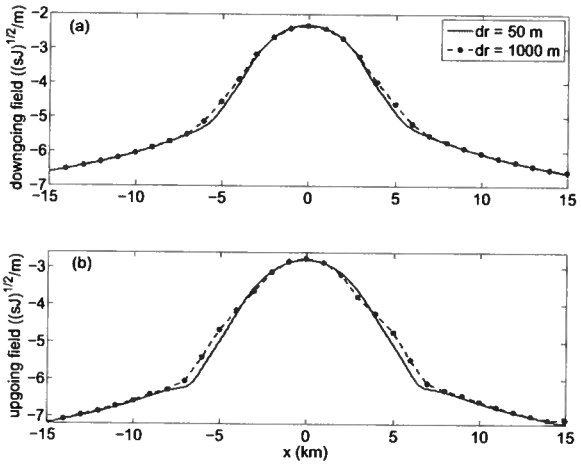

Figure 3.18. the 2-D decomposed downgoing (a) and upgoing (b) fields using a receiver spacing of 50 m (solid lines) and 1000 m (dashed lines). Note that the horizontal scale is different from figure 3.17.

components are removed. Consequently, the required receiver spacing increases from 50 m to 1 km. Figure 3.18 shows the decomposed fields using a 1 km receiver spacing comparing with those using 50 m spacing. Figure 3.18(a) is the downgoing field from the weighted 10 km long source and figure 3.18(b) is the upgoing field. The solid lines are the fields calculated with 50 m receiver spacing and the dashed-marked lines are calculated based on a receiver spacing of 1 km. Because the high wave number components of the original E and H_y fields are removed by tapering, we can increase the required receiver spacing from 50 m to a realistic value (1 km) used in current CSEM surveys.

3.6 Discussion and Conclusions

I have shown that by using the multi-dimensional-deconvolution interferometry in a 3-D synthetic CSEM survey, the airwave in shallow water is removed. The reflection response of the subsurface is obtained, which contains information only from below the receiver level. Consequently, the difference between the models with and without a reservoir is significantly enhanced. The required receiver sampling criterion, however, is unrealistically

dense comparing to current CSEM surveys. Besides, a 2-D receiver array, instead of the receivers located on a line, is required to apply this technique accurately .

In order to increase the required receiver spacing, we introduce the synthetic aperture concept. In this chapter, we demonstrate how to construct a large source in the inline direction. By tapering the contribution to the large synthetic source, we effectively remove the high wave number components in the E and H fields. These smooth E and H fields requires less receivers in the up-down decomposition process. In this chapter, Hann window function squared has been used. One, however, can design other tapering windows to remove the spikes in data. Note that in the real part of the E_x field (figure 3.17), there are small bumps at the edge of the source. These bumps contains some high wave number components. The tapering window can be optimized to further increase the required receiver spacing in the up-down decomposition.

If there are only receivers located on a line, the lack of information in k_y leads to an inaccurate up-down decomposition. In order to accurately decompose the field, receivers in the crossline direction are crucial. As we have done in the inline direction, further research on the 3-D synthetic aperture source is needed to reduce the crossline direction receiver spacing. The upgoing field from a 2-D decomposition, however, still increases the imprint of the reservoir. Therefore, 2-D decomposition can still be valuable for interpreting the presence of the reservoir as well as the inversion of the CSEM data, as long as one applies the same process to both data and synthetics.

Chapter 4

Can diffusive fields be steered and focused?

4.1 Summary

Although beam steering and focusing have been used for waves in many important ways, the application of these concepts to diffusive fields has not been wide spread because of a common belief that diffusion lacks directionality and therefore can neither be steered nor focused. We show the similarities between diffusion and waves and prove that diffusive fields can be steered and focused both in the frequency domain and time domain. This finding has potential of extending the use of diffusive fields as a diagnostic tool in science.

4.2 Introduction

In general, diffusive fields (such as diffusing chemicals, heat, low-frequency electromagnetics in conductive media, light in highly scattering media) are fields whose propagation is governed by the diffusion equation or that have a diffusive character. An example of the latter is low-frequency electromagnetic fields in conductive media (Ward & Hohmann, 1987). These diffusive fields have been used in important ways in modern science (Yodh & Chance, 1995; Mandelis, 2000). Beam steering and focusing have been widely used for waves (Barber, 1985; Ralston *et al.*, 2007; Cutrona, 1975; Bellettini & Pinto, 2002; Song & Park, 1990; Lu *et al.*, 1994; Wooh & Shi, 1999; Liu & Weiss, 2009; Lu *et al.*, 2006) either by using a physical array that steer or focus waves, or by using data processing to achieve this (referred to as the synthetic aperture technique in Refs (Barber, 1985; Ralston *et al.*, 2007; Cutrona, 1975; Bellettini & Pinto, 2002)). These techniques have seldom been discussed for

diffusive fields because it is commonly believed that such fields lack directionality (Mandelis, 2000; Gershenson, 1999). In this letter, we use the similarities between the Green's functions of waves and diffusion in a homogeneous space to show that diffusive fields can be steered and focused. For vector fields, the change of the propagation direction also causes the change in the polarization of the field.

As with the applications involving waves, beam steering and focusing for diffusive fields can extend the use of these fields and open new research directions. For example, it is shown in (Fan *et al.*, 2010b) that the anomaly in the electromagnetic field due to the presence of the submarine hydrocarbon reservoir is dramatically increased by applying beam steering to diffusive electromagnetic fields.

4.3 Similarities Between Diffusion and Waves

Although diffusion and wave propagation are two different fundamental physical processes, the analogy in the mathematical description of these two processes is known (Kunetz, 1972; Isaev & Filatov, 1981; Filatov, 1984; Lee *et al.*, 1989). Also, the interference (a wave concept) of diffusive fields has been widely used in physics (Schmitt *et al.*, 1992, 1993; Knuttel *et al.*, 1993; Yodh & Chance, 1995; Wang & Mandelis, 1999).

The 3D diffusion equation in a homogeneous medium, under the Fourier convention $f(t) = \int F(\omega)e^{i\omega t}d\omega$, can be written in the frequency domain as

$$D\nabla^2 G(\mathbf{r}, \mathbf{r}_s, \omega) - i\omega G(\mathbf{r}, \mathbf{r}_s, \omega) = -\delta(\mathbf{r} - \mathbf{r}_s), \tag{4.1}$$

where D is the diffusivity of the medium, δ the Dirac-Delta function, ω the angular frequency, and $G(\mathbf{r}, \mathbf{r}_s, \omega)$ the Green's function at position $\mathbf{r}$ from a source at $\mathbf{r}_s$. The homogeneous equation $D\nabla^2 u(\mathbf{r}, \omega) - i\omega u(\mathbf{r}, \omega) = 0$ has plane wave solution in the frequency domain

$$u(\mathbf{r}, \omega) = e^{-ik\hat{\mathbf{n}}\cdot\mathbf{r}}e^{-k\hat{\mathbf{n}}\cdot\mathbf{r}}, \tag{4.2}$$

where $k = \sqrt{\omega/(2D)}$. Equation (4.2) shows that at a single angular frequency ω, diffusion

can be treated as damped wave propagation (Mandelis, 2000). Because of the used Fourier-convention, this solution is multiplied with $e^{i\omega t}$ to give an outgoing propagation. Term $e^{-ik\hat{\mathbf{n}}\cdot\mathbf{r}}$, therefore describes the propagation of the field in the $\hat{\mathbf{n}}$ direction and $e^{-k\hat{\mathbf{n}}\cdot\mathbf{r}}$ defines the decay of the field in the $\hat{\mathbf{n}}$ direction. Note that as with monochromatic wave propagation, diffusion admits solutions with a specific direction of propagation.

A transform used often to covert a diffusive field to a lossless wave is $i\omega' = \sqrt{i\omega}$ (Lee *et al.*, 1989; Gershenson, 1999). This transform is referred to as the q-transform or diffusive-to-propagation mapping. In practice, this transform usually is not stable. In this letter, we use another approach to implement diffusion as damped and dispersive wave propagation. Following the definition of the phase velocity $v = \omega/k = \sqrt{2D\omega}$ and the attenuation coefficient $\alpha = \sqrt{\omega/(2D)}$, one can view diffusion as a dispersive wave both in phase velocity and attenuation. With this representation, a traditional Fourier transform can be used to transfer the field to the time domain.

In the next section, we construct synthetic elongated sources (i.e. the white bar in Fig. 4.1) by adding point sources together. The field from a point source is given by the Green's function of equation (4.1)

$$G(\mathbf{r}, \mathbf{r}_s, \omega) = \frac{1}{4\pi D\,|\mathbf{r}-\mathbf{r}_s|} e^{-ik|\mathbf{r}-\mathbf{r}_s|} e^{-k|\mathbf{r}-\mathbf{r}_s|}, \tag{4.3}$$

where $\mathbf{r}_s$ is the source position (Mandelis, 2001). The diffusive field generated by the synthetic line source is steered and focused by applying appropriate phase shift and energy compensation. Both frequency domain and time domain examples are shown in the next section.

4.4 Numerical Examples

Next we show numerical examples of field steering and focusing in both the frequency domain and the time domain.

4.4.1 Frequency Domain

In many applications of diffusive fields, the analysis is carried out in the frequency domain. This is the case, for example, in controlled source electromagnetics for hydrocarbon exploration (Edwards, 2005; Constable & Srnka, 2007). The frequency domain steering and focusing method in this section can also be adapted to time-domain monochromatic fields such as a single-frequency light in strongly scattering media.

Here we show a numerical example for a three-dimensional homogeneous medium with the diffusivity of D =2.4×10^5 m$^2/s$, which corresponds to the diffusivity of low frequency electromagnetic fields in conductive sea water. The frequency of the field used in this section is 0.25 Hz. The field from a 10 km linear synthetic source, as illustrated by the white bars in Fig. 4.1 , is defined as

$$G_A(\mathbf{r}) = \int_{-L/2}^{L/2} e^{-i\Delta\phi(x)} e^{-A(x)} G(\mathbf{r}, x, \omega) dx, \tag{4.4}$$

where x is the individual point source location, L the length of the synthetic source, $\Delta\phi(x)$ the phase shift for the source at location x and $A(x)$ an energy compensation coefficient for the source at x. The phase shift $\Delta\phi(x)$ controls the interference of the field from different sources. Because of the strong decay of the field, the contribution from each individual source to the total field can be very different at a specific point depending on the distance between the individual source and this observation point. For this reason, an exponential term $e^{-A(x)}$ is needed to compensate for the diffusive loss. We choose the energy compensation coefficient $A(x)$ to be the same as $\phi(x)$. The decay of the field is associated with the applied phase shift, and the attenuation coefficient in equation (4.3) has the same value as the wave number ($\sqrt{\omega/(2D)}$).

For steering the field, we use a linear phase shift $\phi(x) = c_1 k \Delta x$, where $\Delta x = |x + L/2|$ is the distance between each source and the left edge of the synthetic source, $c_1 = \sin\theta$ is a coefficient to control the steering angle θ. We next steer the field approximately 45

degrees to the right side of the source using $c_1 = 0.7$. Because of the rapid decay nature of the diffusive field, no feature can be visualized with a linear scale. In order to visualize both the amplitude and sign of the highly attenuated field G_A, we define the following transformation. First, the imaginary part of G_A is scaled by $I_G = m\mathtt{Im}(G_A)$, where m is a scaling factor to make the smallest amplitude of $|I_G|$ to be 10^0. We then define

$$Z = \mathtt{sgn}(I_G)\mathtt{log}_{10}|I_G|, \tag{4.5}$$

to retain the sign of the field. The upper and middle panels of Fig. 4.1 show the new dimensionless field Z, which is the logarithm of $|I_G|$ with a minus sign when I_G is negative. The upper panel shows the field with zero steering ($c_1 = 0$). In the middle panel, the field is steered at approximately 45 degrees and the constant phase fronts are tilted by the steering ($c_1 = 0.7$). The lower panel of Fig. 4.1 is the ratio of the field amplitude with phase steering to the field amplitude without the phase steering, defined as

$$R = \frac{\left|\int_{-L/2}^{L/2} e^{-i\Delta\phi(x)} e^{-\Delta\phi(x)} G(\mathbf{r}, x, \omega) dx\right|}{\left|\int_{-L/2}^{L/2} e^{-\Delta\phi(x)} G(\mathbf{r}, x, \omega) dx\right|}. \tag{4.6}$$

This ratio is the largest at angle of 45 degrees from the synthetic source. This example illustrates that we can indeed steer a frequency-domain diffusive field at a designed angle.

We next apply a phase shift, which is designed to focus the diffusive field, to the individual sources. When (x_f, z_f) is the designed focal point in the x-z plane, the distance from the focal point to the nearest end (x_e, z_e) of the synthetic source is $r = \sqrt{(x_e - x_f)^2 + (z_e - z_f)^2}$. The phase shift for each point source is defined as $\Delta\phi(x) = k(\sqrt{(x - x_f)^2 + (z - z_f)^2} - r)$. In Fig. 4.2 we show an example of focusing with the focal point at (x=0 km, z=1 km). As in the example in Fig. 4.1, the imaginary part of G_A is transformed using equation (4.5) and field Z is shown in the upper panel. The lower panel is the ratio of $|G_A|$ after and before focusing, as defined in equation (4.6). The lower panel of Fig. 4.2 shows that with

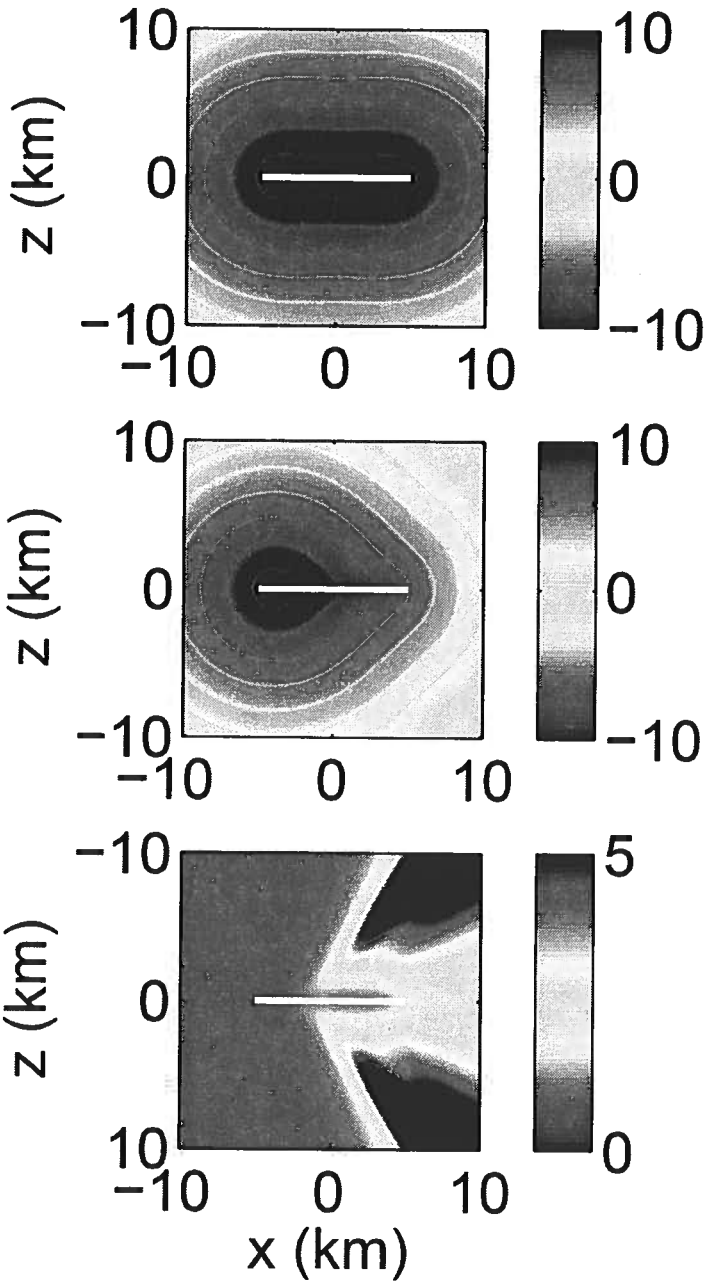

Figure 4.1. Upper panel: transformed field Z with zero steering ($c_1 = 0$); Middle panel: transformed field Z after steering at angle of 45 degrees ($c_1 = 0.7$). Lower panel: ratio of the field amplitude $|G_A|$ with steering to the amplitude without steering. The white bar in the two panels illustrates the size of the elongated synthetic source.

this phase shift the diffusive field indeed focuses at the designed location. The relationship between field focusing and the synthetic source properties (e.g. size and distance to the focal point) is described in the literatures of focusing technique for waves (Lu *et al.*, 1994; Wooh & Shi, 1998, 1999)].

4.4.2 Time Domain

For waves in non dispersive media, the steering and focusing in the above section can be also achieved by employing the individual sources with a different time delay (Wooh & Shi, 1998, 1999), but because of the dispersive character of diffusive fields, this time delay can not be applied to diffusive fields. Following equation (4.4), the steering in the frequency domain for a source at location x can be represented by a multiplication with $S(\omega, \theta, x) = e^{-\sqrt{i\omega/D}(x+L/2)\sin\theta}$. In the time domain, this multiplication corresponds to a temporal convolution with

$$s(t, \theta, x) = H(t)\frac{(x + L/2)\sin\theta}{\sqrt{4\pi D t^3}} e^{(x+L/2)^2 \sin^2\theta/(4Dt)}, \tag{4.7}$$

where $H(t)$ is the Heaviside function (makes $s(t, \theta, x)$ zero for the negative time). Contrary to non-dispersive waves, the steering is no longer a time shift factor, but a full time-convolution operator acting on all times for the source switching time to the time instant when steering is desired.

Here we take the dispersive-wave view of diffusion and present a method to steer or focus diffusive fields by synthesizing these fields in the frequency domain following the method we presented in the above section, and then Fourier transform back to the time domain. The following example shows that this synthesized field indeed can be steered or focused in the time domain.

In this example, the medium is the same as the one we used in the above examples. The source signal is a Gaussian wavelet with a frequency distribution of $g = e^{-(f-f_0)^2/\sigma^2}$, where f is the frequency, central frequency f_0=5 Hz, $\sigma = \sqrt{5}$ Hz. A linear 5 long km synthetic

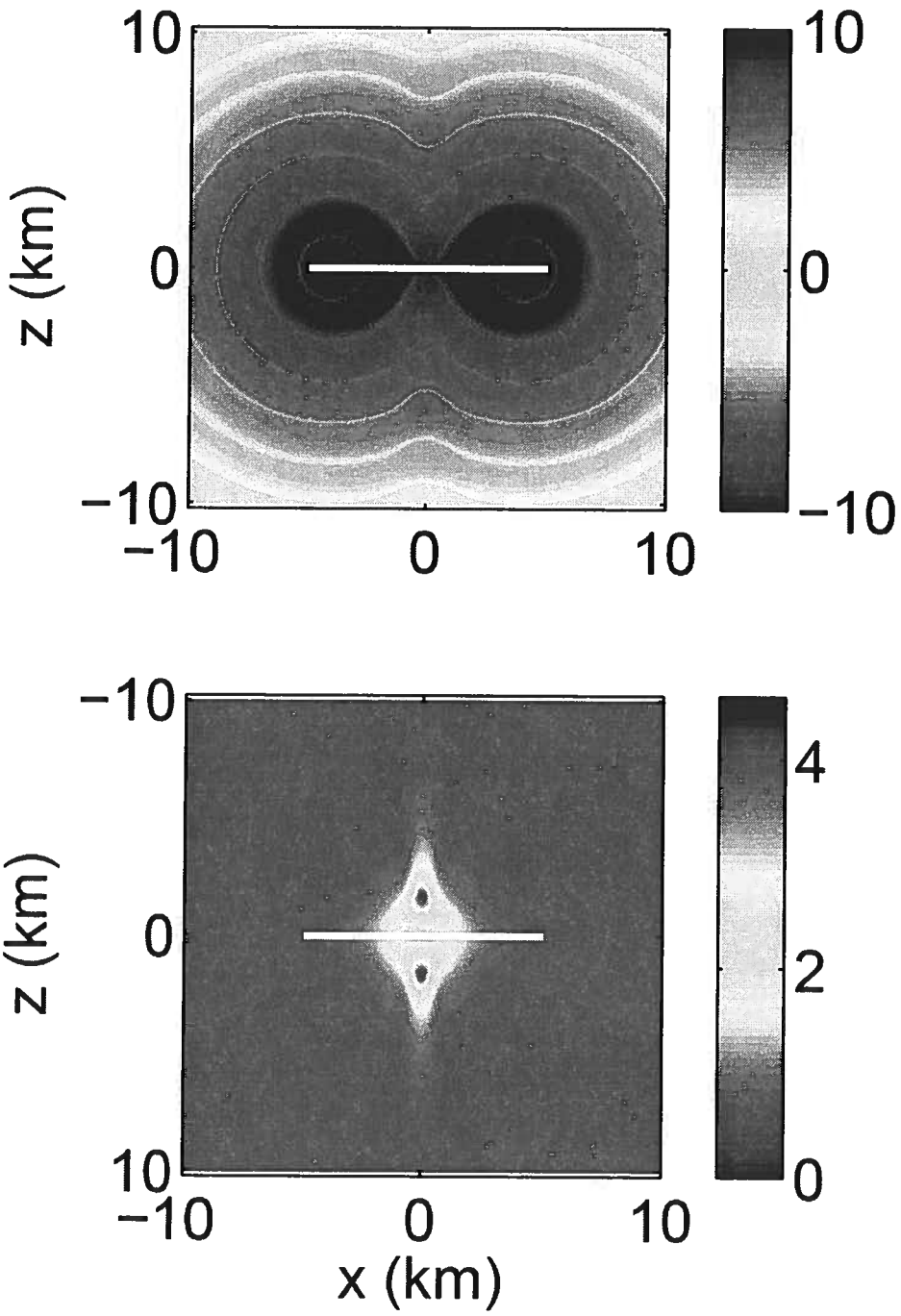

Figure 4.2. Upper panel: transformed field Z using equation 4.5 after focusing at (x=0 km,z=1 km). Lower panel: ratio of the field amplitude $|G_A|$ with focusing to the amplitude without focusing. The white bar in the two panels illustrates the size of the elongated synthetic source.

source (the white bars in Fig. 4.3) is constructed by adding individual sources in the line. Each frequency component is steered or focused using the method presented above (with same steering angle and focal point), but in this example the sources are not weighted. The Fourier transform of the modified field shows how the field propagates in time. Fig. 4.3 is a snapshot at t = 0.2 s. The transformed field Z is displayed using equation (4.5). The white bar in both panels illustrates the length of the synthetic source. The upper panel shows that the field propagates at an angle of 45 degrees to the right of the source as denoted by the dashed arrow. Because the attenuation increases with frequency, the high frequency components are only visible close to the source array, while the low frequency components travel further. In the lower panel, the field focuses at the depth of 1 km. The dashed arrows illustrate how the field propagates. An video of how the field is propagated in time can be seen online. Although the original waveform is not retained because of the dispersion in both velocity and the attenuation, this example illustrates that the total field in the time domain indeed can be steered and focused.

4.5 Conclusion

We have shown that diffusive fields can be treated as waves with a specific dispersion in both phase velocity and attenuation. In the frequency domain, diffusive fields can be steered and focused with proper phase shifts and amplitude weighting. In the time domain, the field can not be steered or focused with simple time shifts to the individual sources. Instead, each frequency component needs to be treated separately in the frequency domain first. The Fourier transform of these treated frequency components shows a steering or focusing of the field in time. The techniques provided in this letter has potential of extending or improving the use of diffusive fields, in applications such as hydrocarbon exploration using low frequency electromagnetics, submarine communications, and medical imaging using diffusive light.

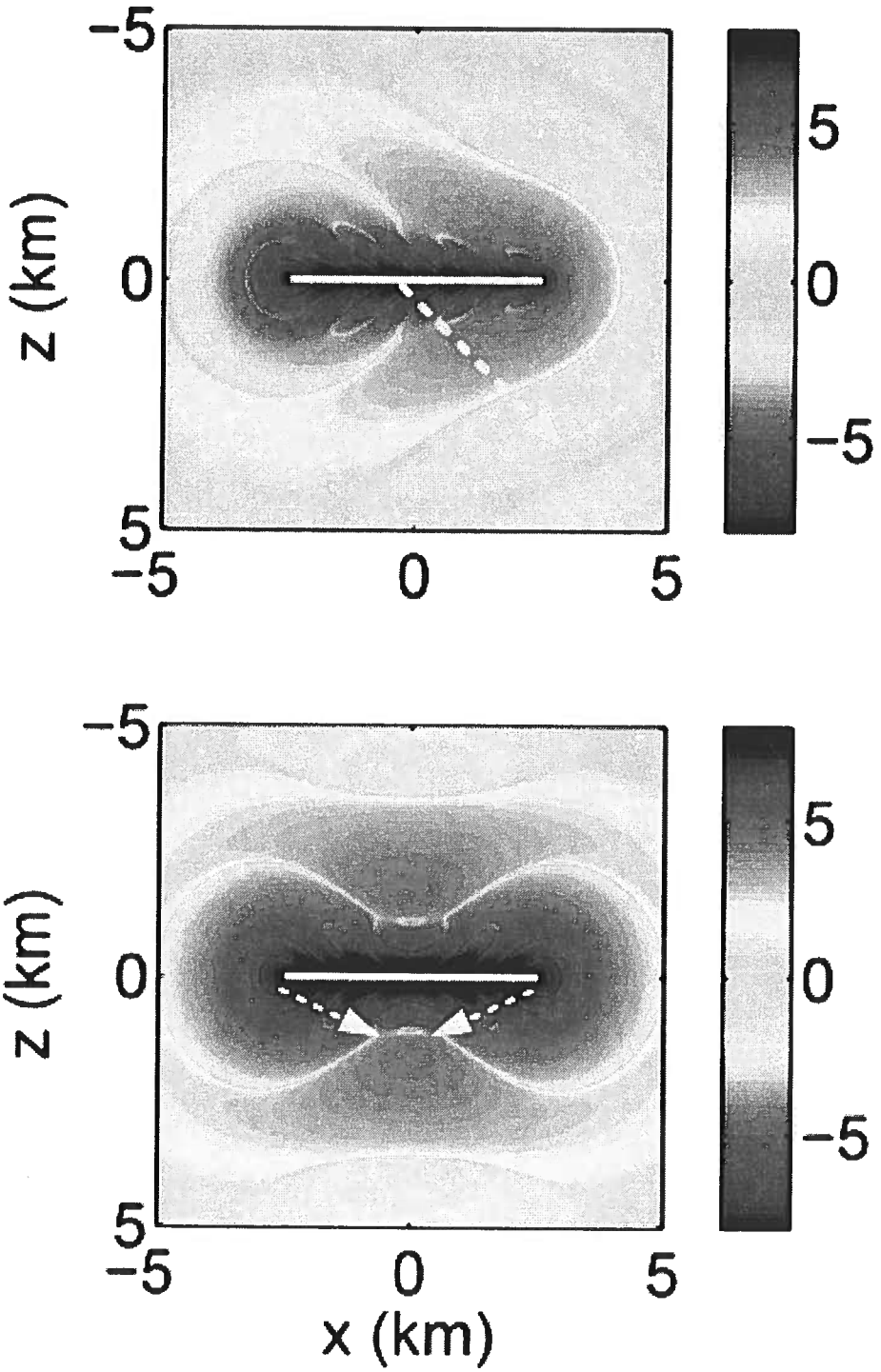

Figure 4.3. Upper panel: the diffusive field at t=0.2 s with field steered at angle of 45 degrees. Lower panel: the diffusive field at t=0.2 s with field focused at position (x=0 km,z=1 km). The white bar in the two panels illustrates the size of the synthetic source.

Chapter 5

Increasing the sensitivity of controlled source electromagnetics with synthetic aperture

5.1 Summary

Controlled-source electromagnetics (CSEM) has been used as a de-risking tool in the hydrocarbon exploration industry. Although there have been successful applications of CSEM, this technique is still not widely used in the industry because the limited types of hydrocarbon reservoirs CSEM can detect. In this chapter, we apply the concept of synthetic aperture to the low frequency electromagnetic field in CSEM. Synthetic aperture sources have been used in radar imaging for many years. Using the synthetic aperture concept, big synthetic sources can be constructed by adding the response to small sources (building blocks) in different ways, and consequently, big sources with different radiation patterns can be created. We show that the detectability of hydrocarbons is significantly enhanced by applying synthetic aperture to CSEM data. More challenging targets such as deep reservoirs 4 km below sea floor can be detected. We also propose alternative acquisition systems based on the increased response obtained by synthetic aperture techniques. This includes towing the source close to the sea surface, and towing both source and receivers close to the sea surface. These new acquisition geometries reduce the cost of CSEM surveys. We also show, with the synthetic aperture concept, how a synthetic vertical source can be constructed by adding the response to small horizontal sources. The synthetic aperture concept opens a new line of research in CSEM, with the freedom to design suitable synthetic aperture

sources creatively for a given purpose.

5.2 Introduction

Low frequency controlled-source electromagnetics (CSEM) has been used in the oil industry as a de-risking tool to distinguish hydrocarbon reservoirs since the beginning of this century. In hydrocarbon exploration, CSEM is also referred to as seabed logging (Ellingsrud *et al.*, 2002). The fundamental assumption of using CSEM as a detector of hydrocarbons is that porous rocks are resistive when saturated with gas or oil, but conductive when filled with brine. The history and detailed description of CSEM is given by MacGregor & Sinha (2000), Edwards (2005), and Constable & Srnka (2007).

Although there are many successful case studies showing the ability of CSEM to detect hydrocarbon reservoirs, this method has not been completely accepted by the industry as an exploration tool. The fundamental reason of the limitations in using CSEM is the diffusive nature of the electromagnetic field in conductive media such as sea water and the subsurface below it. Because of diffusion, the electromagnetic field decays rapidly in space, and consequently the secondary field refracted from the target can be much smaller than the background field (the received field without the target). Because only the secondary field from the target carries information about the target, the interpretation of the target signature can be difficult or impossible if the target field is hidden in the background field. Therefore, most of the successful applications of CSEM are in deep water (>1 km), with a shallow target (<2.5 km), with a large horizontal extent (several kilometers), and few other resistors in the background. Even with these criteria, the anomaly in the recorded field due to the hydrocarbon reservoir is small.

Fan *et al.* (2010b) showed that the detectability of hydrocarbon reservoirs increases dramatically by forming a synthetic aperture source for CSEM. In this chapter, we explore this concept in more detail and show some of the valuable applications and improvements to CSEM exploration. Synthetic aperture is a concept that has been widely used in the radar and sonar community e.g., (Barber, 1985; Ralston *et al.*, 2007; Zhou *et al.*, 2009;

Cutrona, 1975; Riyait *et al.*, 1995; Bellettini & Pinto, 2002). The basic idea of the synthetic aperture concept is to use the interference of the fields from different sources to construct a big synthetic source (aperture) which has a special radiation pattern designed for a specific purpose.

We consider a simple example to illustrate the concept. In a lossless homogeneous space, the frequency-domain 3D Green's function is $G(r,\omega) = e^{ikr}/r$ for wave propagation. The real part of the Green's function from a point source located at the origin is shown in the upper panel of figure 5.1. In this example we use a frequency of 0.25 Hz, a medium velocity of 866 m/s. We next construct an 10 km long elongated source by adding 200 uniformly distributed point sources from x = -5 km to 5 km, all at z=0 km. Apart from contributions from the edges of the source array, the elongated source emits a plane wave that propagates in the vertical direction (lower panel of figure 5.1). Compared to a physical source 10 km long, one has more freedom in building a big source synthetically by adding the fields emitted by small sources. For example, a linear phase shift along the source array can be applied to the individual sources before the summation, and as a result the total field is steered in a certain angle. This is illustrated by the upper panel of figure 5.2. Similarly, the total field can be focused in a location if appropriate phase shifts are applied to the individual sources, as shown in the lower panel of figure 5.2. Steering and focusing using synthetic aperture has already been used for wave problems such as radar and ultrasound imaging (Berson *et al.*, 1981; Lu *et al.*, 1994; Korobov *et al.*, 2010; Aguttes *et al.*, 2000; Wang *et al.*, 2009).

We have shown in Chapter 3 that diffusive fields can also be steered and focused by applying appropriate phase shift and amplitude weighting. Consequently, one can extend the synthetic aperture concept to CSEM, where the electromagnetic fields propagate diffusively. The basic idea is that a diffusive field can be viewed as a highly attenuating wave with dispersion in both phase velocity and attenuation. In fact, the similarities in the mathematical expressions of wave propagation and diffusion can be found in the literature

(Kunetz, 1972; Isaev & Filatov, 1981; Filatov, 1984; Lee *et al.*, 1989; O'Leary *et al.*, 1992; Boas *et al.*, 1993, 1994). Also, the interference of diffusive fields has been widely used in physics (Schmitt *et al.*, 1992, 1993; Knuttel *et al.*, 1993; Yodh & Chance, 1995; Wang & Mandelis, 1999).

In this chapter, we show that the imprint of the hydrocarbon reservoir in a measured field can be dramatically increased by applying field steering to CSEM data. This enhances the ability to detect more challenging reservoirs. We show that a deep target (4 km below the sea floor) can be detected with field steering. We also propose the possibility of alternative acquisition systems based on the increased response obtained with synthetic aperture techniques. This includes towing the source close to the sea surface, and towing both source and receivers close to the sea surface. These new acquisition geometries reduce the cost of CSEM surveys. Note that the concept of synthetic aperture is not limited to field steering or focusing. In the last example in this chapter, a synthetic vertical source is constructed by using two pairs of orthogonal dipoles. In practice, one can design a variety of synthetic sources depending on the goal of the survey. As is common for CSEM, the data and analysis in the following examples are in the frequency domain.

5.3 Field Steering

A general formula for constructing a synthetic aperture source S_A is

$$S_A(\mathbf{r},\omega) = \sum_{n=1}^{N} a_n e^{i\phi_n} s(\mathbf{r},\mathbf{r}_n,\omega). \tag{5.1}$$

At a single angular frequency ω, a synthetic source at location $\mathbf{r}$ is a superposition of the spatially distributed sources that are located from $\mathbf{r}_1$ to $\mathbf{r}_N$ with an amplitude weighting a_n and a phase shift ϕ_n. In expression (5.1), $s(\mathbf{r},\mathbf{r}_n,\omega)$ is the individual source function. Consistent with typical CSEM surveys, the sources are assumed to be continuously distributed along a line (taken to be the x axis). We apply a linear phase shift to the individual source

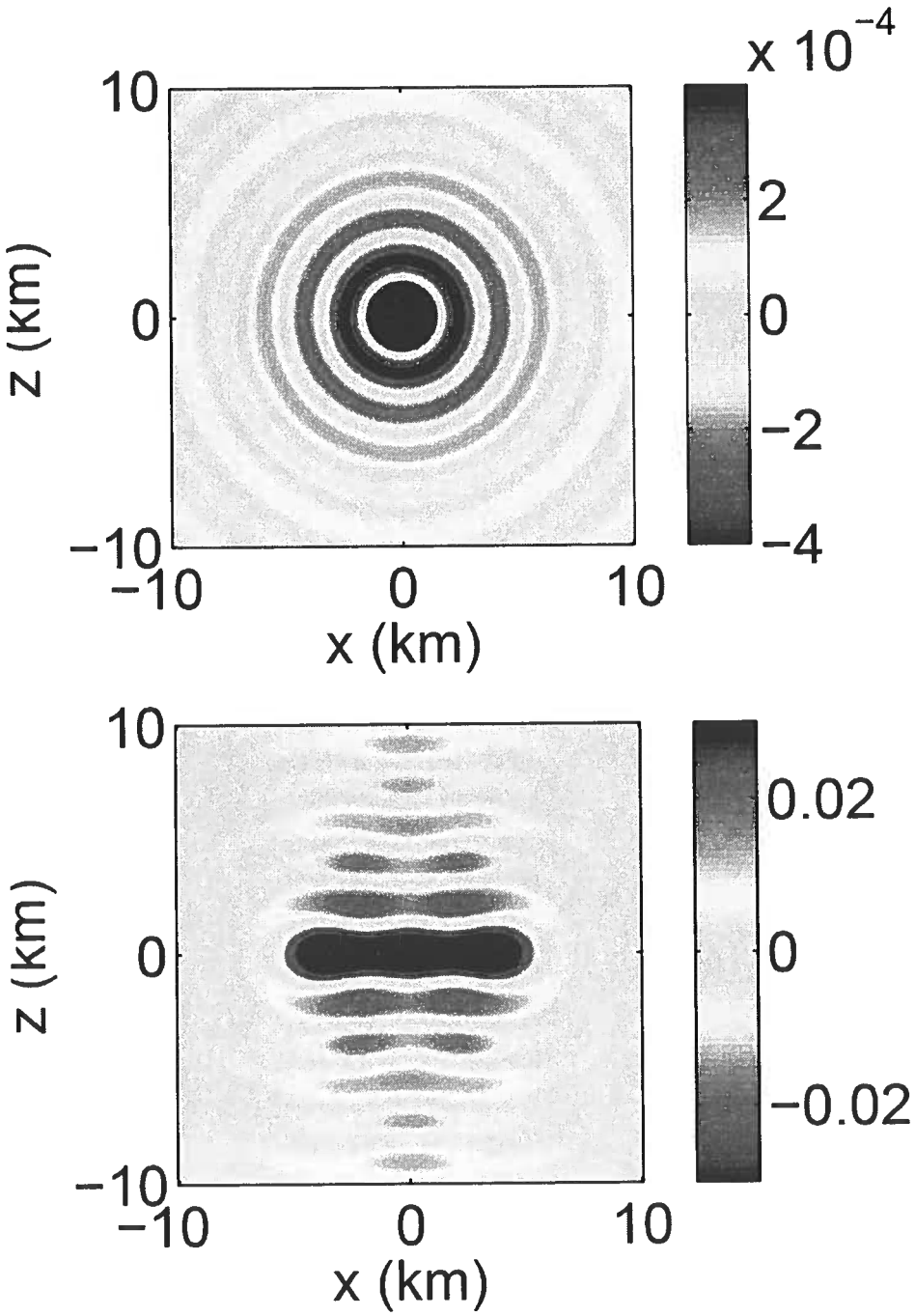

Figure 5.1. Upper panel: real part of the Green's function $G(r,\omega) = e^{ikr}/r$ for a point source of waves; Lower panel: an elongated source, 10 km long, created by adding Re(G) from 200 point sources between x=-10 km and x=10 km.

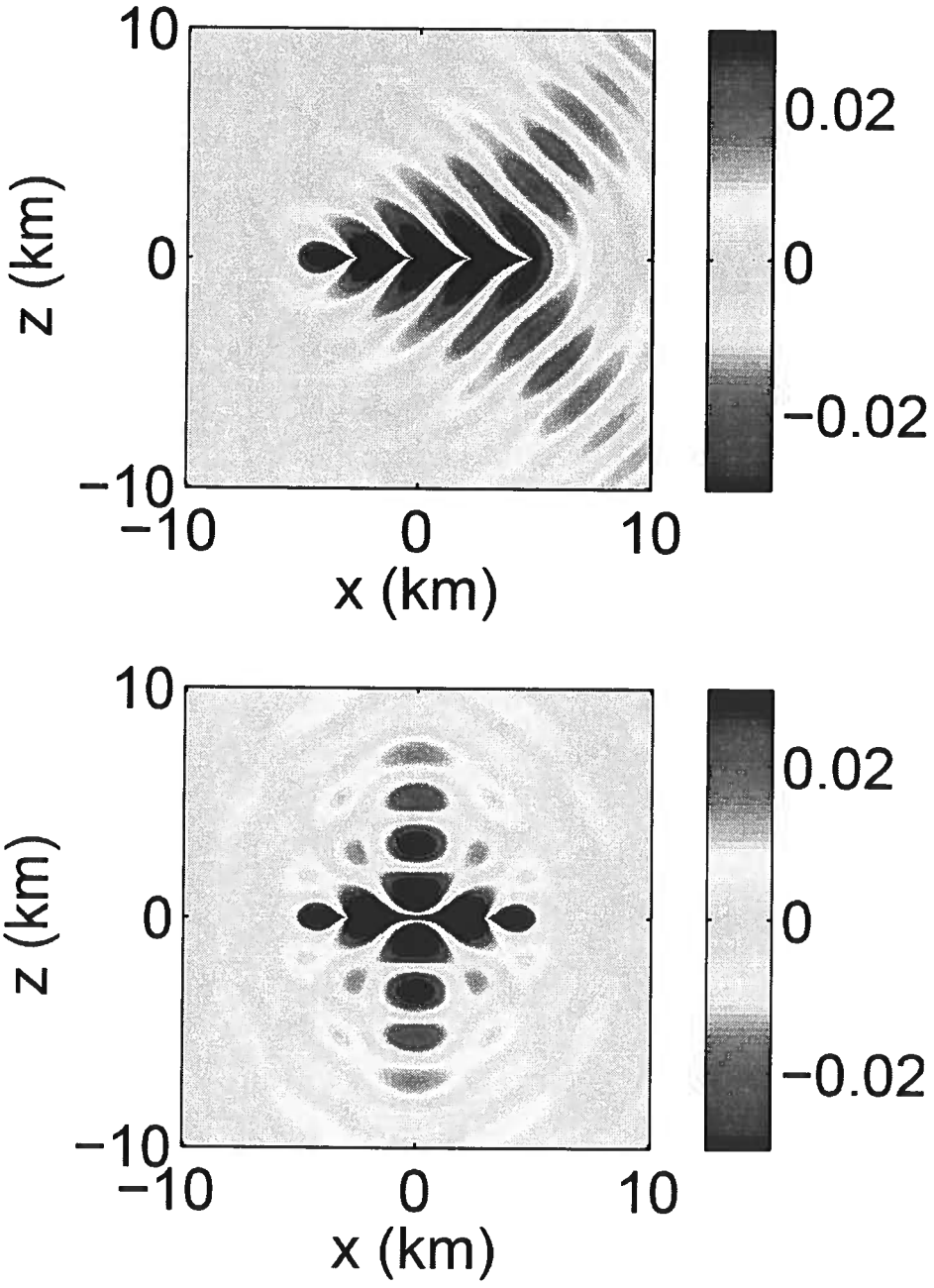

Figure 5.2. Upper panel: an elongated source, 10 km long, created by adding Re(G) from 200 point sources with field steering at 45 degrees; Lower panel: an elongated source, 10 km long, created by adding Re(G) from 200 point sources with field focusing at x=0 km and z=-3 km;

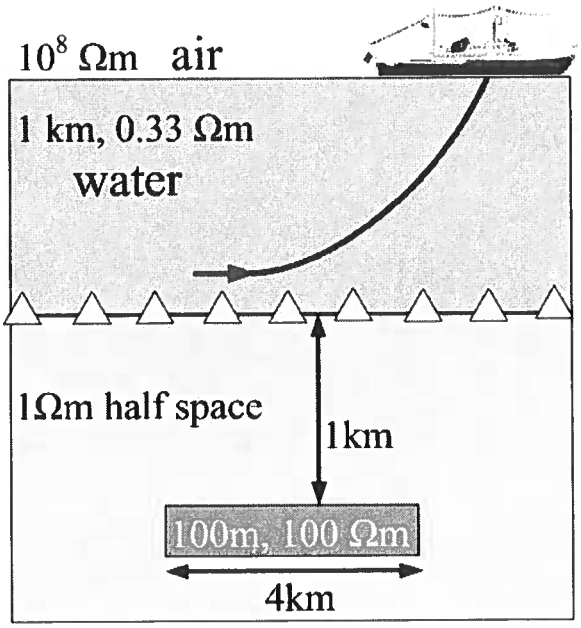

Figure 5.3. Model used in section "Shallow target". The arrow towed by the boat is the dipole source and the triangles on the sea floor are the receivers.

in the line to steer the field to an designed direction. The total field can be represented as

$$S_A(x,\omega) = \sum_{n=1}^{N} e^{-ic_1\alpha\Delta x_n} e^{-c_2\alpha\Delta x_n} s(x, x_n, \omega), \tag{5.2}$$

where $\alpha = \sqrt{\omega\mu\sigma/2}$ is the real or imaginary part of the wave number k for the diffusive electromagnetic field, μ is the permeability, σ is the conductivity, c_1 is a coefficient to control the steering angle (phase change), c_2 is a coefficient to compensate the energy loss due to the diffusion (amplitude weighting), and $\Delta x_n = |x_n - x_1|$ is the distance from the source x_n to the left edge of the array.

5.3.1 Shallow Target

We first show field steering to a shallow target (1 km below the sea floor) to illustrate the dramatic increase of the reservoir anomaly in measured fields. The model we use in this

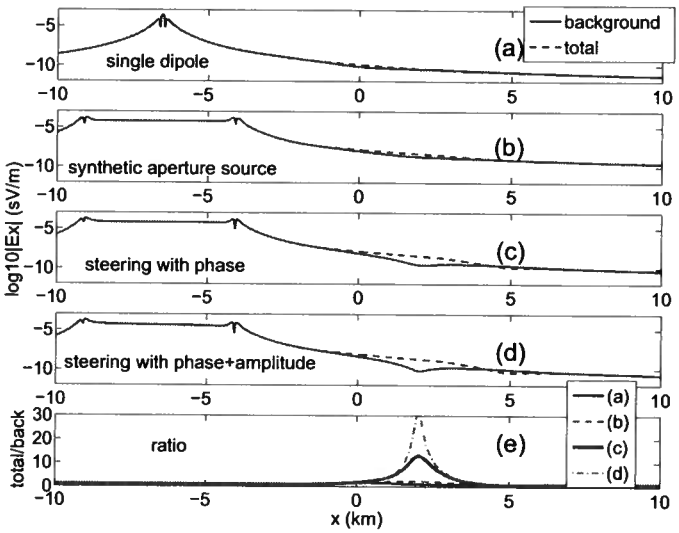

Figure 5.4. Panels (a) to (d) show the inline electrical fields with the reservoir (dashed lines) and without the reservoir (solid) for four different sources; a 100m dipole source (panel (a)); a 5 km dipole source (panel (b)); a 5km synthetic source obtained from field steering toward the target by the phase shift (panel (c)); a 5km synthetic source obtained from field steering toward the target by the phase shift and the amplitude compensation. Panel (e) shows the ratio between the fields with and without the reservoir. The four curves in panel (e) represent the ratios from each of the panels above.

numerical example is shown in figure 5.3. A hydrocarbon reservoir with resistivity of 100 Ωm is centered at the origin, with horizontal extent of 5 km in the x and y directions and a thickness of 100 m. The sea water is 1 km deep with a resistivity of 0.3 Ωm. The subsurface background is a half space with a resistivity of 1 Ωm. The receivers are located at the sea floor and a 100 m dipole source with a current of 100 A is continuously towed 100 m above the receivers. The source current oscillates with a frequency of 0.25 Hz. Figure 5.4(a) shows the inline electrical fields in the presence of the reservoir (dashed line) and without the reservoir (solid line) from a single 100 m dipole whose center is located at x=-6.5 km. There is a slight increase in the field around x=0 km when the reservoir is present. This

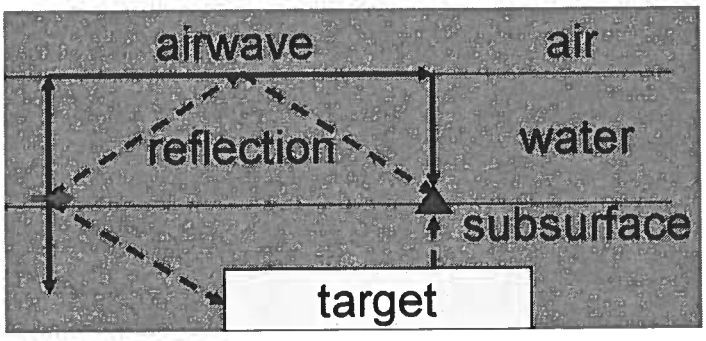

Figure 5.5. A sketch of the energy propagation paths from the source to the receivers in CSEM.

20% difference is shown by the ratio of the field with the reservoir to the field without the reservoir (thin solid curve in figure 5.4(e)). We next costruct a 5 km long dipole by superposing the 50 employed sequential sources. This is equivalent to setting c_1=0 (zero angle steering), c_2=0 (same weighting), and N=50 in equation 5.2. The superposition of the fields is exactly the same as the field from a 5 km long physical dipole source with a current of 100 A. The total E_x fields are given by figure 5.4(b). The ratio of the fields with and without the reservoir is shown by the dashed curve in panel (e). Although the overall signal strength increases compared to the single 100 m source (panel (a)), the difference in the measured E_x fields between the models with and without the reservoir does not significantly increase by simply using a longer dipole.

We next apply a linear phase shift to the 50 sequential sources using c_1=0.7 to steer the field to the angle of approximately 45 degrees. The coefficient c_1 controls the slope of the linear phase shift and can be related to the steering angle θ (steering direction to the vertical) by $c_1 = \sin\theta$ (valid for $c_1 < 1$) (Fan *et al.*, 2010a). Figure 5.4(c) shows the E_x field excited by the synthetic aperture source whose field is steered to the right. The ratio of the steered fields is illustrated by the thick solid curve in the bottom panel. This example shows that the detectability of the reservoir significantly increases by steering the field toward the target.

To explain the effectiveness of field steering, we consider how the field steering affects the way in which the electromagnetic field propagates. Figure 5.5 is a sketch of the paths along which the electromagnetic field propagates from the source to a receiver. Because of the radiation pattern of a dipole antenna, most of the energy propagates perpendicular to the dipole direction. For the horizontal dipole used in CSEM, most energy therefore propagates vertically (solid arrows from the source in figure 5.5). The vertical downgoing energy propagates into the subsurface where, in this case, the target is not located. This portion of energy therefore does not contribute to detect the target. Because of the extremely small critical angle from sea water to the air, the vertical upgoing energy is converted to airwave at the sea surface. The airwave does not attenuate while traveling along the sea surface, hence the airwave dominates the recorded field for large offsets. Besides the vertical paths, the energy also propagates in all other directions as illustrated in figure 5.5. Part of the energy radiates upward is totally reflected at the sea surface (dashed lines in figure 5.5). The downgoing energy that reaches the target is refracted by the target and the upgoing field after this refraction is called the target field.

When the field is steered toward the target, there are two changes in the radiation pattern that lead to the increased imprint of the reservoir in the measured field. First, since the electrical field is transversely polarized, both the total electrical field and the z-component of the E field increase at the target location when the field propagation is steered from the vertical direction to a tilted angle. The z-component of the E field diagnoses changes in the conductivity in the vertical direction (Edwards, 2005), so the secondary field refracted from the reservoir increases. In the synthetic example, this secondary field increases only about 30% (not shown in figure 5.4). Second, when the energy is steered away from the vertical direction, the fields reflected by the sea surface increases while the airwave decreases. Because the reflected field has a longer propagation path in the sea water than the air wave, it attenuates more, and hence the total received field decreases due to airwave reduction. Evidence to support the reasoning of the reducing airewaves is

that the tail part of the background E_x field, which consists mostly of the airwave, decases on both sides of the source no matter whether the field is steered to the right or left. Given that the secondary field from the target increases because of the better illumination, and the background field decrases mainly because of the airwave reduction, the imprint of the reservoir is more pronounced after field steering.

So far we have applied phase shifts to the individual sources to steer the total field to one side of the synthetic source. The attenuation of a diffusive field causes the sources on the opposite side to give a smaller contribution to the synthetic aperture construction because they propagate a greater distance. Because the diffusive field decays exponentially, an exponential weighting term $e^{-c_2\alpha\Delta x_n}$ in equation (5.2) is included to compensate for this energy loss, where c_2 is a constant that controls how much weight each individual sources have. Fan *et al.* (2010a) show that for an homogeneous medium, the best steering is achieved for $c_2 = c_1$. But in the layered model used here we find empirically that the anomaly due to the reservoir is largest when c_2 is 0.1. Figure 5.4(d) shows the fields after including the energy compensation term $e^{-0.1\alpha\Delta x_n}$. This difference is quantified by the ratio of the fields with and without the target and is illustrated by the dashed-dotted line in panel (e).

Why is the optimal value of c_2 different for a homogeneous medium than for the layered model we use here? As explained earlier, there are two reasons that cause the reservoir imprint to be more pronounced: the increase of the secondary field, and the decrease of the background field. The increase of the secondary field is optimal when $c_1 = c_2$, but the decrease of the background field is more complicated for a variety of reasons. The first reason, as state above, is the reduction of the airwave due to the change of the incident angle. The second reason is the interference between different arrivals, which makes the resulting interference of these arrivals depend in a complicated way on the radiation pattern of the synthetic source. There are many different paths for the energy travel from the source to the receivers, as figure 5.5 illustrates. Energy can propagate directly from the source to the receiver, be carried in the airwave, be reflected and refracted from the sea floor,

or be refracted back from the shallow depth (like a diving wave). There is constructive and destructive interference between these arrivals. When the field is steered, destructive interference can occur in the background field (the dip around x =2 km in figure 5.4(c)(d)). This dip in the background field creates a window through which the secondary target field can be better detected. As the amplitude of each arrivals varies, the amplitude weighing (by parameter c_2) of individual sources becomes critical because destructive interference only occurs when the interfering fields are of a comparable strength.

Further research is needed to identify the individual arrivals, to better understand the mechanism of the destructive interference, and optimally design the amplitude weighting for each source. For example, what is the best combination of c_1 and c_2? Is the exponential weighting function best at creating the interference window? In practice, one can numerically search the optimal values of c_1 and c_2 for the particular model used. A large number of c_1 and c_2 pairs can be used in the creation of the synthetic aperture source, and one can numerically search the pairs of c_1 and c_2 that give the largest anomaly. This is equivalent to sweeping the field steering from zero to ninety degrees while changing the weighting of the individual sources. Because the CSEM data set is relatively small, the computational cost of this parameter search is low. Note that one does not need to acquire new field data to carry out this parameter search. It only requires processing of existing data.

The above example shows that the synthetic aperture technique dramatically increases the difference in electrical field response between the models with and without the reservoir by a factor of 30. Note that this is achieved without altering the data acquisition. If noise is added in the above example, the main observation still holds as the coherent fields from the source are still steered. The signal to noise ratio is enhanced because the coherent field increases faster than the noise does when a big synthetic source is constructed. However, the anomaly ratio may not be as big as the example's factor of 30 because the noise is not coherent and can not be steered.

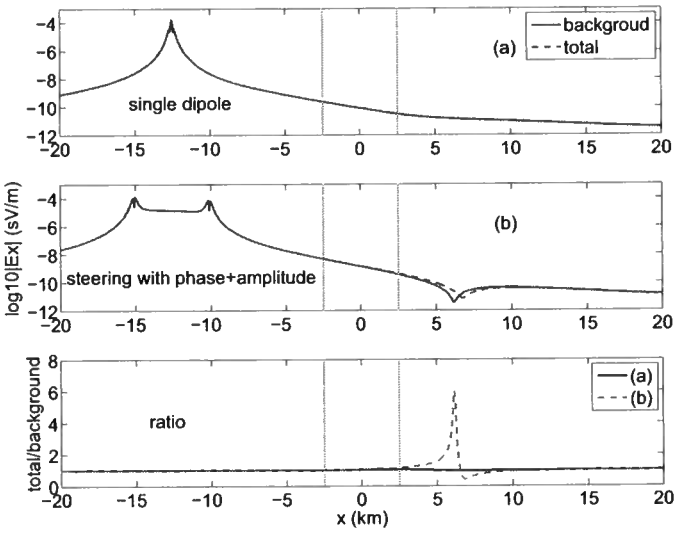

Figure 5.6. Panel (a) and (b) show the inline electrical field with the reservoir (red dashed lines) and without the reservoir (black solid lines) for two different sources; a single dipole source (panel (a)) and a 5 km synthetic source obtained from field steering toward the reservoir by the phase shift and the amplitude compensation (panel (b)). Bottom panel shows the ratio between the fields with and without the reservoir. The two curves in the bottom panel represent the ratios from each of the panels above.

5.3.2 Deep Target

We have shown that the imprint of the shallow target (1 km below the sea floor) dramatically increases after applying field steering. It is logical to think that field steering could help detect deeper targets. The current deepest reservoir that CSEM can detect is about 3 km. This limitation in depth penetration of CESM makes this technique currently not suitable for most of the deep reservoirs. In the following example, we show that by applying field steering to the current CSEM data, a deeper reservoir (4 km below the sea floor) can be clearly detected.

In the following numerical example, a hydrocarbon reservoir with a resistivity of 100 Ωm is centered at the origin with horizontal extent of 8 km in the x and y directions and

a thickness of 100 m. The reservoir is 4 km below the sea floor. The source and receiver parameters are the same as used in the above example. For a better penetration, we choose a lower source frequency of 0.01 Hz. The measured E_x fields (single dipole) are shown in figure 5.6(a). No difference can be seen between the field with the reservoir (solid line) and the field without the reservoir (dashed line). The ratio of these two fields is shown as the solid line in the bottom panel. The vertical lines in each panel represent the edges of the reservoir in the horizontal direction. In fact, no anomaly is visible no matter where the source is located. Figure 5.6(b) shows the field from a 5 km long synthetic source with the field steered toward the right. A clear anomaly is present both in the measured field (figure 5.6(b)) and the ratio (figure 5.6(c)). In this case, multiple c_1 and c_2 pairs are tested, with the optimal pair found to be $c_1 = 3.4$ and $c_2 = 0.1$.

As described above, c_1 can be related to the incident angle by $c_1 = \sin\theta$ when $c_1 < 1$, but what happens if c_1 becomes larger than one? We first answer this question for wave propagation. For mathematical simplicity, we analyze a 2-D wave field in a homogeneous medium with $k_x^2 + k_z^2 = \omega^2/v^2$, where v is the wave velocity. With field steering, the horizontal wavenumber becomes $k_x = c_1\omega/v$, making the vertical wavenumber $k_z = \pm\sqrt{\omega^2/v^2 - c_1^2\omega^2/v^2}$. When c_1 is less than one, it is related to the steering angle by $c_1 = \sin\theta$ and $k_z = \omega\cos\theta/v$. When c_1 is bigger than one, k_z is imaginary and the total field is evanescent. For a diffusive field in a homogeneous medium, $k_x^2 + k_z^2 = i\omega/D$, with D the diffusion constant. With steering, the horizontal wave number is $k_x = c_1\sqrt{i\omega/D}$, while the vertical wavenumber is $k_z = \pm\sqrt{i\omega/D - c_1^2 i\omega/D} = \pm\sqrt{i\omega/D(1-c_1^2)}$. When $c_1 > 1$, k_z is still complex, but the decay rate in the z direction depends on the value of c_1. When $c_1 > 1$, it becomes a amplitude weighting parameter. As stated above, the amplitudes for different arrivals are crucial to create the destructive interference in the field. In this case, both c_1 and c_2 control the amplitude weighting and we find empirically that the combination of $c_1 = 3.4$ and $c_2 = 0.1$ creates this destructive interference window that makes it possible to detect a reservoir at 4 km depth.

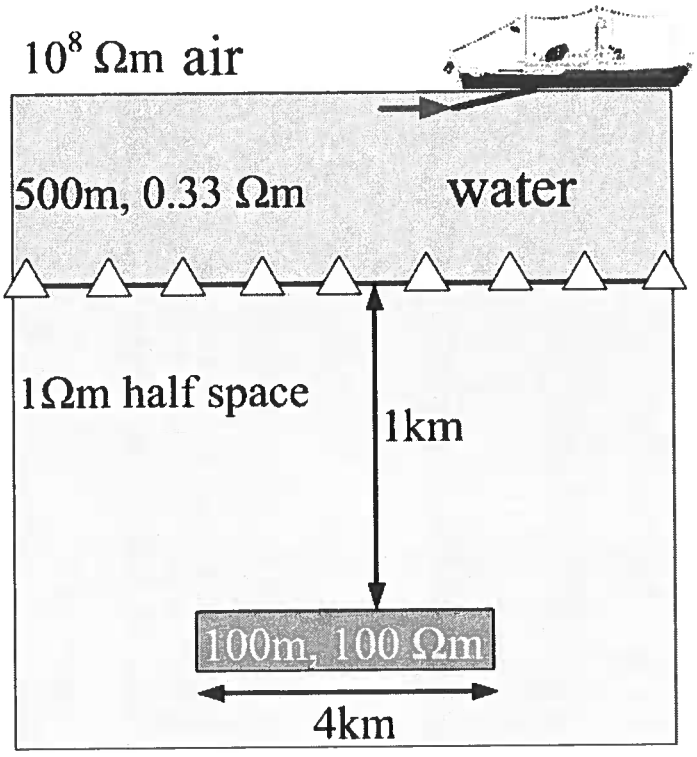

Figure 5.7. The model used in section "Shallow sources and ocean bottom receivers". The source is towed either 10 m or 0 m below the sea surface.

5.3.3 Shallow Sources and Ocean Bottom Receivers

In current CSEM surveys, the source is towed close to the sea floor to minimize the dissipative loss in sea water. Towing a source at depth can be technically challenging and expensive. Since field steering can increase the imprint of the reservoir dramatically, we propose a new acquisition system in which the source is towed close to the sea surface. Note that if the water depth is too big, near-surface towing obviously can not work because all the energy would dissipated in the sea water. But in relatively shallow water, near-surface towing can be applicable considering the increased detectability by applying field steering. In the following example, we use a water depth of 500 m, but this is not a limiting case. Further research is needed to investigate the maximum water depth for a

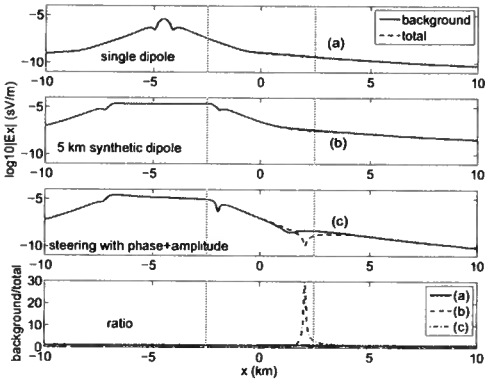

Figure 5.8. Panel (a) through (c) show the inline electrical field with the reservoir (dashed lines) and without the reservoir (solid lines) for three different sources; a single dipole source (panel (a)); a 5 km synthetic source (panel (b)); and a 5 km synthetic source obtained from field steering toward the reservoir by the phase shift and the amplitude compensation (panel (c)). Panel (d) shows the ratio between the fields with and without the reservoir. The three curves in panel (d) represent the ratios from each of the panels above. In this system, the dipole source is towed 10 m below the sea surface and receivers are at the sea floor.

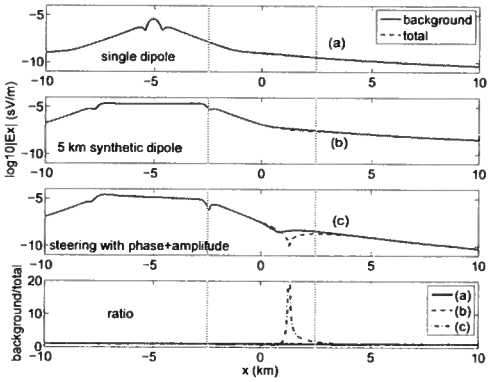

Figure 5.9. Panel (a) through (c) show the inline electrical field with the reservoir (dashed lines) and without the reservoir (solid lines) for three different sources; a single dipole source (panel (a)); a 5 km synthetic source (panel (b)); a 5 km synthetic source obtained from field steering toward the reservoir by the phase shift and the amplitude compensation (panel (c)). Panel (d) shows the ratio between the fields with and without the reservoir. The three curves in panel (d) represent the ratios from each of the panels above. In this system, the dipole source is towed at the sea surface and receivers are at the sea floor.

given target for near-surface towing. A modeling feasibility study can be carried out to test if near-surface towing is appropriate for the given water depth and given target (i.e. size, depth and conductivity) following the method we use below.

The model used in this example is shown in figure 5.7. A hydrocarbon reservoir with the resistivity of 100 Ωm is centered at the origin at a depth of 1 km below the sea floor, a horizontal extent of 4 km in the x and y directions, and a thickness of 100 m. The source is a 100 m dipole source with a 100 A current, towed 10 m below the sea surface, oscillating at a frequency of 0.25 Hz. The receivers are located on the sea floor. In figure 5.8(a), the measured E_x fields from the single dipole show no difference between the field with the reservoir (solid line) and the field without the reservoir (dashed line) because the airwave dominates the measured fields. The ratio of the background and the total field is shown by the solid line in figure 5.8(d). Figure 5.8(b) shows the background and total fields from a 5 km long synthetic source, whose field is steered downward (zero steering). The overall field strength increases but no imprint of the reservoir can be seen. The ratio of the fields is shown by the dashed line in the bottom panel. Next, we steered the field toward the right using $c_1 = 0.7$ and $c_2 = 0.1$. A clear anomaly is then seen in figure 5.8(c), with the ratio of the background field and the total field from panel (c) indicated by the dashed-dotted line in the bottom panel. Note that in this case, the field with the reservoir is smaller than the field without reservoir. The definition of the ratio in the bottom panel is different from those used in the previous examples. Instead of the ratio of the total field and the background field, we show the inverse ratio as the total field is smaller than the background field. In fact, that the total field is smaller than the background field is an indication of the destructive interference between the target field (secondary field) and the airwave.

We have shown the case where the source is towed 10 m below the sea surface. To take this one step further, we also test the extreme case of towing the source at the sea surface. As shown in figure 5.9, towing the source at the sea surface does not result in a significant difference compared with towing the source at 10 m in depth. The above two examples

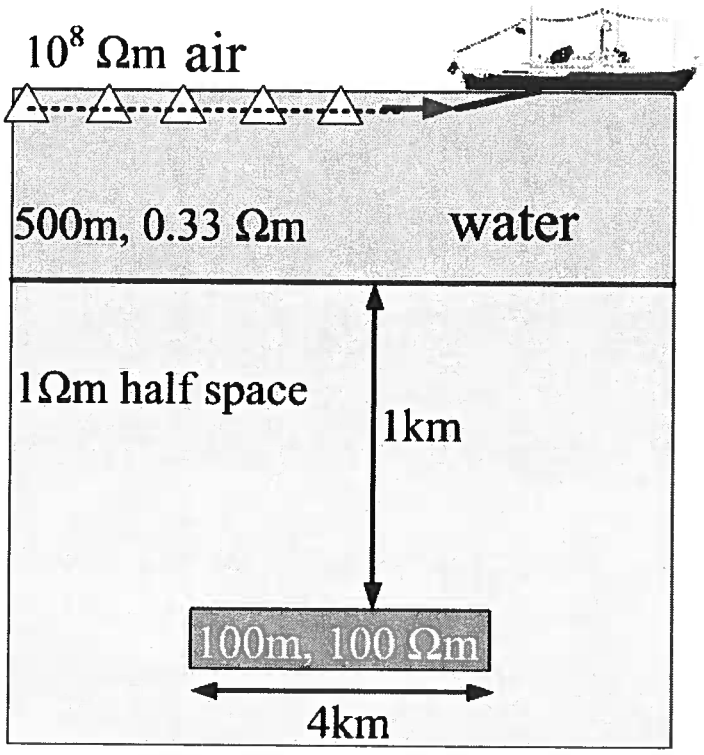

Figure 5.10. The model used in the section "Shallow towing system for the source and receivers". The source and receivers are towed either 10 m or 0 m below the sea surface.

show that by applying field steering, CSEM acquisition can be simplified by towing the source close to or on the sea surface.

5.3.4 Shallow Sources and Receivers

We have shown that by constructing appropriate synthetic aperture, it is possible to tow the source close to the sea surface. In this section, we investigate if it is possible to tow both the source and receivers close to the sea surface. The main reason for locating receivers on the sea floor is to reduce the dissipative loss of the electromagnetic fields. Since we can use field steering to better detect the reservoir, towing receivers close to the sea surface becomes feasible. This new type of acquisition can significantly reduce the survey cost and provide dense receiver locations because the receivers are also continuously moving.

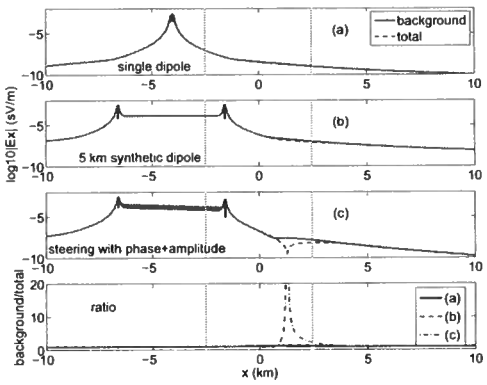

Figure 5.11. Panel (a) through (c) show the inline electrical field with the reservoir (dashed lines) and without the reservoir (solid lines) for three different sources; a single dipole source (panel (a)); a 5 km synthetic source (panel (b)); a 5 km synthetic source obtained from field steering toward the reservoir by the phase shift and the amplitude compensation (panel (c)). Panel (d) shows the ratio between the fields with and without the reservoir. The three curves in panel (d) represent the ratios from each of the panels above. In this system, both the dipole source and receivers are 10 m below the sea surface.

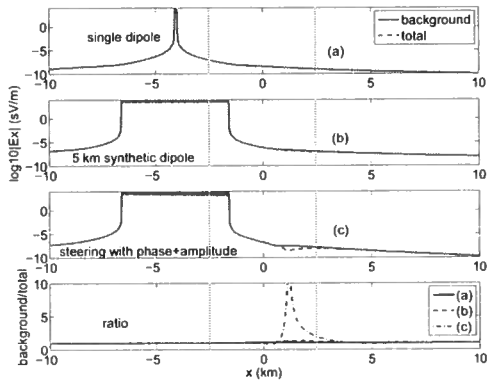

Figure 5.12. Panel (a) through (c) show the inline electrical field with the reservoir (dashed lines) and without the reservoir (solid lines) for three different sources; a single dipole source (panel (a)); a 5 km synthetic source (panel (b)); a 5 km synthetic source obtained from field steering toward the reservoir by the phase shift and the amplitude compensation (panel (c)). Panel (d) shows the ratio between the fields with and without the reservoir. The three curves in panel (d) represent the ratios from each of the panels above. In this system, both the dipole source and receivers are at the sea surface.

The dense receiver spacing is crucial for many techniques used in CSEM such as CSEM migration (Zhdanov *et al.*, 1995, 1996; Zhdanov & Traynin, 1997), up down decomposition and CSEM interferometry (Wapenaar *et al.*, 2008; Fan *et al.*, 2009; Hunziker *et al.*, 2009, 2010). Edwards (2005) described the concept of an ocean bottom source-and-receiver towing system to densely distribute receivers. The-near surface source-and-receiver towing system is shown in figure 5.10. The model and source parameters are exactly the same as those used in the above section. The only difference is that the receivers are towed together with the source at the same depth, instead of sitting on the sea floor.

As in the last section, we show two examples: towing the source and receivers 10 m below the sea surface (figure 5.11) and towing them on the sea surface (figure 5.12). Neither the single source fields (figure 5.11(a), figure 5.12(a)) nor the zero steering fields (figure 5.11(b), figure 5.12(b)) show a clear imprint of the reservoir. For the steered field shown in figure 5.11(c) and figure 5.12(c), constructed with $c_1 = 0.7$ and $c_2 = 0.1$, the imprint of the reservoir is clearly visible. The corresponding ratios of the background fields and total fields are shown in figure 5.11(d) and figure 5.12(d).

These two examples show that the near surface source-and-receiver towing system can be used to detect hydrocarbon reservoirs by constructing an appropriate synthetic aperture source. As described in the section above, this new acquisition can only be applicable when the water is not too deep. While the examples shown here give a proof of concept, further research is needed to investigate the feasibility of using near surface source-and-receiver towing system for a given model (i.e. the relationship between the water depth and target information, the near-surface background noise and streaming noise).

5.3.5 Real Data Example

So far we have applied field steering to simple synthetic models. Next, we apply field steering to real data. In real data, the field 'without' the reservoir is defined as the measured field at a reference site under which there is no reservoir. Figure 5.13(a) shows the inline electrical

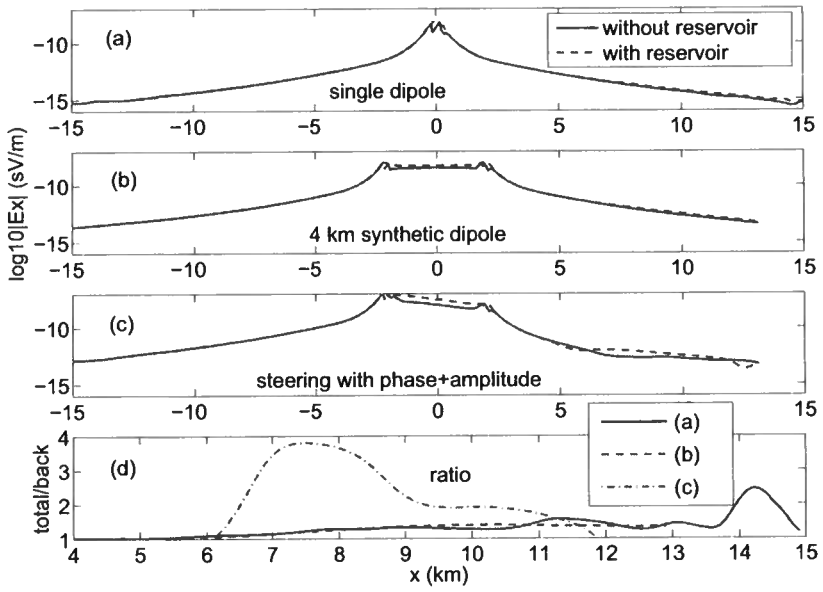

Figure 5.13. Panel (a) through (c) show the inline electrical field with the reservoir (red dashed lines) and without the reservoir (black solid lines) for three different sources; a single dipole source (panel (a)); a 4km synthetic source (panel (b)); a 4 km synthetic source obtained from field steering toward the reservoir by the phase shift and the amplitude compensation (panel (c)). Panel (d) shows the ratio between the fields with and without the reservoir. The three curves in panel (d) represent the ratios from each of the panels above. Note that the horizontal axis in panel (d) is different from that in the other panels.

fields both with (dashed) and without (solid) the reservoir. There is a slight difference in the measured fields between $x = 6$ km to $x = 10$ km, where the reservoir imprint is located. The reservoir is known to be located between $x = 3$ km and $x = 6$ km. The corresponding ratio of the two fields is shown by the solid curve in panel (d). The anomaly in the field near the reservoir is approximately 20%. Beyond offsets of 10 km, the ratio oscillates as the field reaches the noise level and is no longer reliable. Note that on the negtive offset side, no difference in the measured field is observed because there is no reservoir on this side. This consistency of the measured field is an indication that the background geology

is relatively uniform in that area.

Next, we construct a 4 km synthetic aperture source with no field steering. The fields with and without the reservoir are shown by the dashed and solid curves in figure 5.13(b), respectively. The corresponding ratio is the dashed curve in panel (d). Because the longer dipole source has a better signal to noise ratio, both the E_x field and the ratio are smoother than those from an individual source. The overall difference between the responses, however, does not change.

We next steer the fields toward the reservoir using a phase shift ($c_1 = 0.8$) and amplitude weighting ($c_2 = 0.6$). Figure 5.13(c) shows that the difference in the field between the models with and without the reservoir has significantly increased after we apply the field steering. The corresponding ratio is shown by the dashed-dotted line in panel (d). The imprint of the reservoir is much more pronounced in panel (c) than those in panel (a) and (b). Note that the response at negative offsets does not show any difference in the field both before and after the field steering. This is because there is no reservoir for negative offsets. The consistency on the negative offset side, where there is no reservoir, confirms that field steering is only sensitive to the presence of the reservoir. In this example, the choice of c_1 and c_2 is slightly different from the synthetic examples we showed above. This is because the model configurations in this real data example and the synthetic examples is different. This field example shows that synthetic aperture techniques can improve the detectability of a reservoir with field data.

5.4 Synthetic Vertical Source

As we state in the shallow target synthetic example, the z component of the E field is sensitive to the changes in the conductivity in the vertical direction (Edwards, 2005). Therefore, it is not a surprise that a vertical oriented dipole source is most efficient to detect the horizontal reservoirs because the electrical field lines from a vertical source have a large z-component (Mogilatov & Balashov, 1996; Holten *et al.*, 2009). But in practice, there are many reasons that make it difficult to use a vertical dipole as a source. First, to

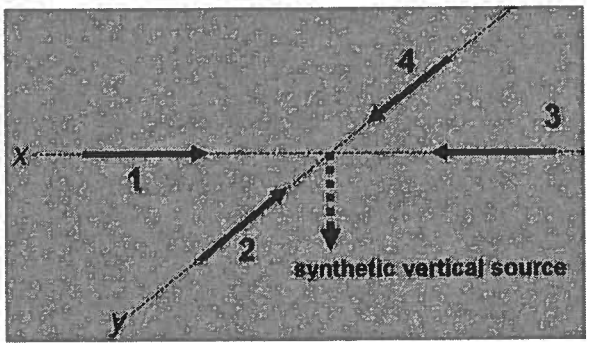

Figure 5.14. Synthetic vertical source (dashed arrow) construction by using two pairs of orthogonal dipoles (solid arrows).

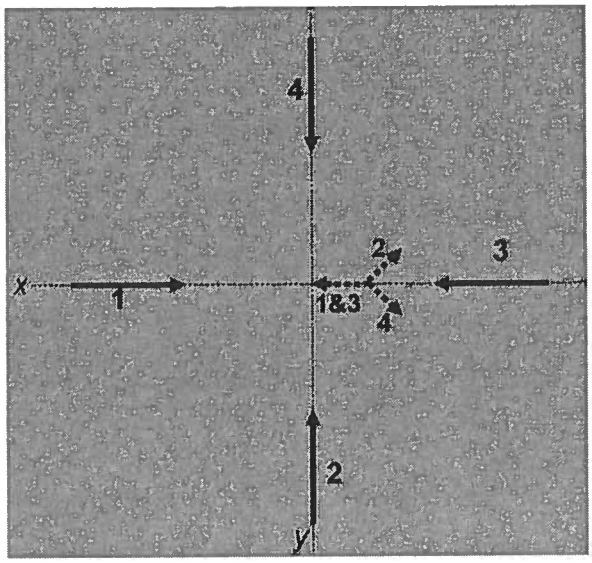

Figure 5.15. Field cancellation from four dipoles.

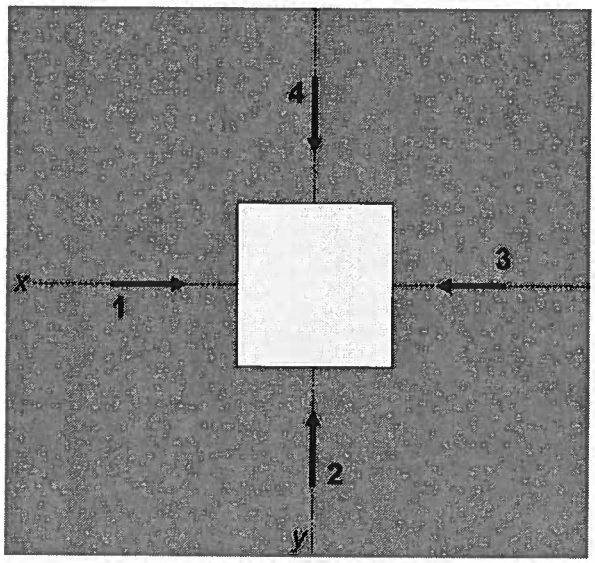

Figure 5.16. Map view of the reservoir (block in the center) and four dipoles.

maintain the vertical position of the 100 m long dipole is technically challenging. Second, the survey time, as well as the cost, can dramatically increase because of the difficulty in moving a vertical source.

We present a method to build vertical sources synthetically by adding orthogonally distributed horizontal dipole pairs, as illustrated in figure 5.14. With the dipoles (solid arrows 1 through 4 in figure 5.14) pointing at each other, the electrical field lines in the center of the area are vertical, as the horizontal components of the field cancel each other and the vertical components constructively interfere. These vertical field lines are effectively equivalent to the field lines from a vertical dipole source, as denoted by the dashed arrow in figure 5.14. A similar setup has been described by Srnka & Carazzone (2003) and a physical setup with 8 dipoles has been used by Helwig *et al.* (2010). The main difference with our method is that we construct the long dipoles synthetically, and have the freedom to adjust the field strength and steering angle as shown below. Figure 5.15 is a map view of the four dipoles, and shows how dipole 2 and 4 help to reduce the horizontal component of the total

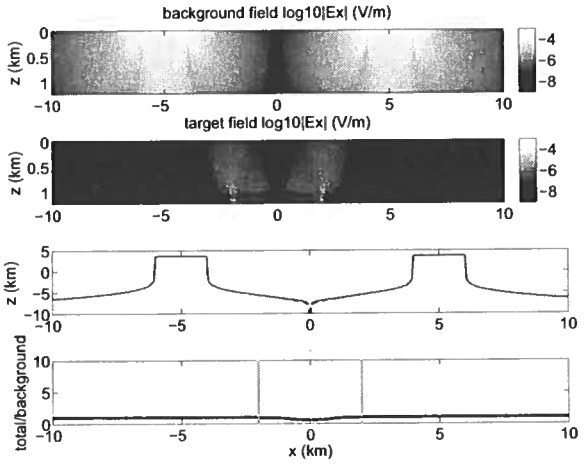

Figure 5.17. From top to bottom, first panel: the cross section in x-z plane of the background E_x field; second panel: the cross section of the target E_x field; third panel: the background (solid) and total field (dashed) at the surface level along x-axis; bottom panel: the ratio of the total field and the background field at the surface level.

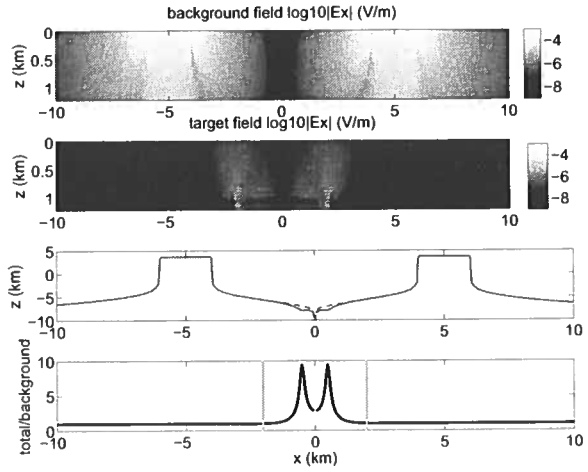

Figure 5.18. From top to bottom, first panel: the cross section in x-z plane of the background E_x field; second panel: the cross section of the target E_x field; third panel: the background (solid) and total field (dashed) at the surface level along x-axis; bottom panel: the ratio of the total field and the background field at the surface level.

field at a location on the x-axis.

As an example, we examine a location on the right side of x-axis, close to dipole 3. The horizontal components of the electrical field from dipole 1 and 3 in opposite directions and because at that location the field from dipole 3 is stronger than that of dipole 1, the remaining horizontal field (dashed arrows in figure 5.15) from dipole 1 and 3 points to the left. The horizontal fields from dipole 2 and 4 point toward dipole 3 as shown in figure 5.15. The destructive combination of these fields reduces the total background field at this point. In contrast to the horizontal background fields from four dipoles, which interfere destructively, the target horizontal fields from these dipoles reinforce each other.

In the following example, we apply the synthetic vertical dipole to a land acquisition system. A 100 m thick reservoir (resistivity of 100 Ωm) with a horizontal extension of 4 km in both x and y directions, is located 1 km below the surface. The subsurface is a half space with a resistivity of 2 Ωm. Figure 5.16 is a map view of the reservoir position (block in the center) and the 4-dipoles system. Each dipole is 2 km long and centers of the two opposite dipoles are 10 km apart. There are several ways one can build this transmitter distribution. The first way is to use four 2 km long physical dipoles, as shown in figure 5.16. The second is to use a single 2 km long dipole and move it to four different positions as shown in figure 5.16. However, the best way is to first construct a 2 km long dipole synthetically by adding small dipoles (200 m long in our example) as shown in the above examples. Then we move the 2 km synthetic dipole to four different positions as shown in figure 5.16. In this way, we build the whole four-dipole system by moving around a single small dipole around. From a practical point of view, a dipole 200 m long is much cheaper and easier to move than a 2 km long dipole. This also gives more freedom to construct the long dipoles, as we show below.

The first panel of figure 5.17 shows the cross section of the background E_x field in the (x,z)-plane from the four-dipole system. The field vanishes at $x = 0$ because the cancellation of the fields from the four dipoles. The second panel of figure 5.17 is the cross section of

the target E_x field. Note that the amplitude of this secondary field is comparable to the background field in the center area because the synthetic vertical source excites the target well. The third panel shows the measured field at the surface level. The solid line is the background field and the dashed line is the total field (with the presence of the reservoir). The ratio of the above fields (with and without the reservoir) at the surface level is shown in the bottom panel. Although we have added two pairs of orthogonal dipoles, the effective vertical source seems imperfect. In the first panel of figure 5.17, the background E_x field is only zero at $x = 0$ but becomes bigger than the target field immediately away from the center point. Therefore, the anomaly in the bottom panel is relatively small. As we learned from figure 5.15, the cancellation of the fields at a certain point depends on the field strength from each dipole at that point. In other words, the total fields at that point only vanishes when the total field from dipoles 2 and 4 has the same strength as the field from dipoles 1 and 3 (figure 5.15). Simply adding the two pairs of dipoles does not guarantee the perfect field cancellation.

In order to adjust the strength of the fields from each dipole and make the field lines in the center area more vertical, we apply the field steering to each long dipole. The field steering can not be achieved if a physical 2 km long dipole is used. In our example, each 2 km long dipole is constructed by ten spatially distributed small dipoles that are 200 m long. These ten spatially distributed dipoles can be obtained by moving one dipole to ten different locations. The field from each 2 km long dipole can be steered using the method we proposed in the previous sections. Here, we steer the field of each dipole toward the center of the dipole array (toward the reservoir). Dipoles 1 and 3 are steered by the same steering parameter c_1 (one to the right and one to the left), which may be different from the steering parameter for dipoles 2 and 4. No amplitude weighting parameter c_2 is used in this example. Figure 5.18 shows the field in the same pattern as figure 5.17 in the case where dipoles 1 and 3 are steered with $c_1 = 0.5$ and dipoles 2 and 4 are steered with $c_1 = 1$. Compared with the case without steering (figure 5.17), the first panel of figure 5.18 suggests

that the background E_x field in the center part becomes much smaller. This implies that the field lines in the center part become more vertical and a better synthetic vertical source is constructed. Therefore, the difference of the measured field at the surface level for the models with and without the reservoir is more pronounced in the third panel. The large anomaly in the bottom panel of figure 5.18 shows a clear imprint of the reservoir.

The above example demonstrates that a synthetic vertical source can be constructed by adding two pairs of dipoles and using field steering to adjust the strength of each dipole. In the synthetic modeling study, we find that there are multiple pairs of steering parameters (besides $c_1 = 0.5$ for dipoles 1 and 3 and $c_1 = 1$ for dipoles 2 and 4) which can give a large anomaly in the measured field. The key is to adjust the fields from each dipole in such a way that the horizontal fields from each dipole interferes destructively as illustrated in figure 5.15. Besides the field steering, other parameters affect the strength from each source. Examples include the size of each dipole, the distance between each dipoles and the conductivity of the subsurface. Further research is needed to optimize the construction of a synthetic vertical source. We only use two pairs of dipole sources in the above example, but it is possible to use more pairs of the dipoles to better force the field lines go vertically, such as the 8-dipole system used by Helwig *et al.* (2010). Since we use a synthetic aperture, more pairs of dipoles can be easily constructed by moving the small dipole source to new locations.

We have shown an application of the synthetic vertical source for a land system. In the marine case, constructing a synthetic vertical source is even easier. A cross-line sailing direction can be added over the target area and the dipoles of the opposite orientation can be obtained simply by adding a negative sign to the measured fields. Effectively the source configuration as shown in figure 5.14 is maintained by constructing synthetic orthogonal dipoles. The position and the size of the long synthetic dipole source can also be adjusted by changing the number and positions of the small dipoles.

5.5 Discussion and Conclusion

We have seen that the detectability of hydrocarbon can be significantly increased by applying the synthetic aperture concept to CSEM data. This means that more challenging reservoirs can be detected, and new acquisition systems of CSEM become applicable, such as near-surface towing systems. The diffusive nature of electromagnetic fields in the conductive subsurface makes those fields decay rapidly in space, and as a consequence the target field, which carries useful information of the reservoir, is normally buried in the background field. Interpreting the presence of a hydrocarbon reservoir can thus be challenging. This difficulty makes the current CSEM system only applicable to a small range of reservoir types, specifically those in deep water, with a large size, shallow in depth and significant resistivity contrast to the surrounding subsurface. The best way to increase the detectability of reservoirs using CSEM is to increase the target field, and at the same time reduce the background field.

Using the synthetic aperture technique, large synthetic sources can be constructed by adding the response to small sources in such a way that the total field from this synthetic source excites a large target field and a small background field for particular offsets. By doing so, significant reservoir anomalies can be found in measured fields. These anomalies not only help interpret the presence of the reservoir, but also increase the accuracy and speed of a CSEM inversion. In this chapter, we show applications for field steering and creating synthetic vertical sources by adding small horizontal dipoles, but this is does not suggest that these are the only or the best ways of applying the synthetic aperture technique.

Besides the horizontal electrical dipoles used here, we could also use magnetic dipoles (or equivalently electrical loops) as building blocks. We have steered the field by applying a linear phase shift in the source array. Focusing the field by applying quadratic phase shifts, could increase the secondary field from the target. A 2-D source array would not only allow for steering the field in the inline direction, but also for steering in the crossline direction. We have demonstrated construction of synthetic aperture sources, but one can also construct

synthetic aperture receivers. There are many opportunities to further enhance the use of a synthetic aperture source in CSEM, and one may learn these processes from synthetic aperture techniques used in the radar and sonar communities.

Chapter 6

Discussion and future work

6.1 Summary of Improvements in CSEM when Using the "Virtual Source" Techniques.

Diffusive low frequency electromagnetics (CSEM) has been used in the oil industry for hydrocarbon exploration. Because CSEM measures the resistivity of the subsurface, the content of fluids in porous rocks can be interpreted. The diffusive nature of the electromagnetic field, however, makes the field decay rapidly in space. Consequently, the secondary field from the reservoir, which carries the information of the target, is significantly smaller than background fields (e.g. the direct field and airwave). It is challenging to interpret the presence of reservoirs in measured data and it is difficult to invert the subsurface resistivity based on the small anomaly in the field. Therefore, only a limited class of reservoirs can be detected by current CSEM surveys; reservoirs need to be shallow, large in horizontal extension, located under deep sea water and have a large resistivity contract with the background medium.

In this dissertation, I have applied two "virtual source" methods to diffusive electromagnetic fields, namely multi-dimensional-deconvolution interferometry and the synthetic aperture technique. Both methods significantly reduce background fields and consequently increase the imprint of reservoirs in measured fields. Multi-dimensional-deconvolution interferometry takes advantage of the up-down decomposition of electromagnetic fields and calculates the reflection response from subsurface between receivers. As we show in Chapter 3,

the gain in the increased sensitivity of reservoirs is mainly from the up-down decomposition. High wave number components in the electromagnetic fields requires receivers to be densely distributed in order to accurately up-down decompose the field in the wave number domain. For a 100 m dipole in a survey over an area of 20 km by 20 km, 160000 receivers (50 m between receivers) are used to decompose fields in the numerical example in Chapter 3. This unrealistically large number makes it unpractical to use multi-dimensional-deconvolution interferometry in field. I investigate the feasibility of applying the 2-D up-down decomposition to the receivers that are located in a line. The decomposed fields are not exactly the same as those from a 3-D up-down decomposition. However, 2-D decomposed upgoing fields still show enhanced imprints of reservoirs. One can also apply the 2-D decomposition in the CSEM inversion to increase the inversion sensitivity of reservoirs, as long as one applies the same process to measured data and numerically modeled data. I also applied synthetic aperture technique to create a large source that emits smoothly varying fields in space. Amplitude tapering is critical to remove the high wave number components. In Chapter 3 I use a Hann window function squared to increase the receiver spacing from 50 m to 1 km.

Besides its advantages in interferometry, the synthetic aperture technique is the second "virtual source" method in this dissertation. Large synthetic sources (or virtual sources) with different radiation patterns can be constructed by adding small sources in different ways. The synthetic aperture technique is a wave based method that has been developed in radar community. Because of a common belief that one can not apply synthetic aperture technique to diffusive fields, this application had not been represented previously. I analyze the similarities between the frequency-domain formulations of wave propagation and diffusion. A diffusive field can be viewed as a highly dispersive damped wave with frequency-dependent attenuation. Therefore, it is appropriate to apply the synthetic aperture technique to diffusive fields, taking dispersion and attenuation into account. In particular, I show that diffusive fields can be steered and focused in both the time domain and the frequency domain.

When applying field steering to CSEM data, both the numerical examples and field data show that the detectability of reservoirs significantly increases by forming a synthetic aperture source. The increased detectability is caused by the enhanced target field and the reduced background field. I show that the two main components in the decreased background field are the airwave reduction and the destructive interference between different arrivals. Both the phase shift and amplitude weighting in field steering are important to reduce the airwave and cause different arrivals to destructively interfere each other. The increased detectability allows one to detect more challenging reservoirs and use near surface towing systems in acquisition. Synthetic aperture applications in CSEM go beyond field steering. I also show an example of creating synthetic vertical source by adding orthogonal dipole pairs. The synthetic vertical source is more sensitive to horizontally extended reservoirs than traditional horizontal dipoles.

6.2 Key Contributions of This Dissertation to Interferometry and Controlled Source Electromagnetics

In Chapter 1, I find that for a strongly heterogeneous medium, one source is not sufficient to accurately reconstruct the Green's function. It is commonly known that equipartioning is a necessary condition in the Green's function reconstruction (Weaver & Lobkis, 2001; Malcolm *et al.*, 2004; Campillo & Paul, 2003; Shapiro *et al.*, 2005; Roux *et al.*, 2005). So one might think a single source may be sufficient to reconstruct the Green's function for strongly heterogeneous media because the heterogeneities make the energy equipartitioned. Our modeling study and analytical derivation show that denser source distribution is required to accurately reconstruct the full Green's function for a strongly heterogeneous medium than that for a homogeneous medium. The part of the Green's function, which corresponds to the direct arrival, does benefit from heterogeneities.

I first show the application of multi-dimensional-deconvolution interferometry to a 3-D CSEM model. I analyzed the receiver distribution that is required for this technique and showed that it required an unrealistically dense array of receivers. In order to solve the

dense receiver requirement, I introduce the synthetic aperture concept to CSEM.

The application of the wave-based synthetic aperture technique to diffusive fields is new. Even though there is a common belief that diffusive fields can not be steered or focused because of the lack of directionality, I show the feasibility of steering and focusing diffusive fields in both the frequency domain and time domain, The ability of CSEM to detect more challenging reservoirs significantly increases after diffusive electromagnetic fields are steered. I propose new acquisition systems for CSEM surveys as a result of the increased detectability.

6.3 Future Work and Suggestions

While the dissertation has introduced several new concepts to diffusive fields, it also leads to many new research questions.

In Chapter 3, I increase the required receiver spacing from 50 m to 1 km in the inline direction for a 2-D up-down decomposition, with a weighted synthetic source 10 km long. Recently, 3-D CSEM acquisitions become more and more popular. The crossline wave number k_y is crucial to accuratly decompose the field in 3-D. Therefore, the up-down decomposition requires a 3-D synthetic aperture that emits smoothly varying fields. Further research is needed on how to construct a synthetic aperture source in the crossline direction. What kind of sailing paths are required to optimally constrcut 3-D synthetic sources? What other physical sources (building blocks) can one use to emit fields that are smoother in space?

In the upgoing or downgoing fields shown in Chapter 3, there are clear destructive interferences that cause dips in fields (e.g. figure 3.9). What can one learn from these patterns of destructive interference? How do they relate to the reservoir parameters such as the depth, size and resistivity? With different boundary conditions, I obtain different upgoing and downgoing fields (e.g. e.g. figures 3.8 and 3.9). What information can one extract from the difference in the decomposed fields from different boundary conditions? For example, do we get the field traveling along the sea floor? The gain of multi-dimensional-

deconvolution interferometry is mainly from decomposed upgoing fields. Theoretically the reflection response R only shows the response from the subsurface and is not affected by any heterogeneities above the receivers. In contrast, the upgoing fields can still be influenced by heterogeneities in sea water. So in what cases does the reflection response R show clear advantages over the upgoing field alone?

In chapter 4 and 5 I have shown the advantages of using field steering in CSEM. Further research is needed to investigate how focusing can help to concentrate energy at the target. How can one combine the focusing and steering to further increase the detectability? So far, I construct 2-D synthetic apertures, how do 3-D synthetic apertures help to detect the 3-D features of reservoirs? To monitor changes of a target, a physical 3-D source array can be build. Then different synthetic aperture sources can be constructed by using these individual sources in the array. Fields can continuously sweep in different angles to monitor changes in the subsurface. In this dissertation I only use horizontal dipoles as the building blocks for synthetic aperture sources. What can one gain using other types of sources such as loop systems? We know that in land surveys, it is difficult to inject the current from a dipole into the subsurface if the near-surface is resistive. In this case, electromagnetic fields from loop systems are more effective to probe deep target. Destructive interference of different arrivals is observed when fields are steered. This destructive interference in the background field creates a window in which the target field can be observed. Further research is needed to quantify the strength of the different arrivals that contribute to the total signal. In this way, one can design better synthetic aperture sources to optimize the destructive interference in background fields. Research on the connection between destructive interference and retrieved reservoir information (depth, size and resistivity) will provide better resolution of the target.

There are many sophisticated processing techniques used in synthetic aperture radar. Applications of the synthetic aperture technique to CSEM would be significantly extended if one could use various synthetic aperture radar techniques to CSEM.

References

Aguttes, J. P., Sombrin, J., Conde, E., Chaubet, M., Sebbag, I., & Bousquet, P. 2000. Radar "sail" satellite concept and design. *Acta Astronautica*, **46**, 565–576.

Amundsen, L., Løseth, L., Mittet, R., Ellingsrud, S., & Ursin, B. 2006. Decomposition of electromagnetic fields into upgoing and downgoing components. *Geophysics*, **71**, G211–G233.

Andréis, D., & MacGregor, L. 2008. Controlled-source electromagnetic sounding in shallow water: Principles and applications. *Geophysics*, **73**, F21–F32.

Bakulin, A., & Calvert, R. 2004. Virtual source: new method for imaging and 4D below complex overburden. *SEG Technical Program Expanded Abstracts*, **23**, 2477–2480.

Bakulin, A., & Calvert, R. 2006. The virtual source method: Theory and case study. *Geophysics*, **71**, SI139–SI150.

Barber, B. C. 1985. Theory of digital imaging from orbital synthetic-aperture radar. *Int. J. Remote Sens.*, **6**(7), 1009–1057.

Basser, P. J., Mattiello, J., & LeBihan, D. 1994. MR diffusion tensor spectroscopy and imaging. *Biophysical. J.*, **66**, 259–267.

Bellettini, A., & Pinto, M. A. 2002. Theretical accuracy of synthetic aperture sonar micronavigation using a displaced phase-center antenna. *IEEE J. Oceanic Eng.*, **27**(4), 780–789.

Berson, M., Roncina, A., & Pourcelota, L. 1981. Compound scanning with an electrically steered beam. *Ultrasonic Imaging*, **3**, 303–308.

Boas, D. A., O'Leary, M. A., Chance, B., & Yodh, A. G. 1993. Scattering and wevelength transduction of diffuse photon density waves. *Phys. Rev. E.*, **47**, R2999–R3002.

Boas, D. A., O'Leary, M. A., Chance, B., & Yodh, A. G. 1994. Scattering of diffuse photon density waves by spherical inhomogeneities within turbid media: Analytic solution and applications. *Proc. Natl. Acad. Sci.*, **91**, 4887–4791.

Bourdet, D. 2002. *Well Test Analysis (Handbook of Petroleum Exploration and Production)*. 1 edn. Elsevier Science.

Calvert, R., Bakulin, A., & Joners, T. C. 2004. Virtual Sources, a new way to remove overburden problems. *Expanded abstracts of the 2004 EAEG-meeting*, 2477–2480.

Campillo, M., & Paul, A. 2003. Long-Range Correlations in the Diffuse Seismic Coda. *Science*, **299**, 547–549.

Claerbout, J. 1968. Synthesis of a layered medium from its acoustic transmission response. *Geophysics*, **33**, 264–269.

Constable, S., & Srnka, L. J. 2007. An introduction to marine controlled-source electromagnetic methods for hydrocarbon exploration. *Geophysics*, **72**, WA3–WA12.

Curtis, A., Gerstoft, P., Sato, H., Snieder, R., & Wapenaar, K. 2006. Seismic interferometry-turning noise into signal. *The Leading Edge*, **25**, 1082–1092.

Cutrona, L. J. 1975. Comparison of sonar system performance achievable using synthetic-aperture techniques with the performance achievable by more conventional means. *J. Acoust. Soc. Am.*, **58**(2), 336–348.

Darnet, M., Choo, M. C. K., Plessix, R. E., Rosenquist, M. L., Yip-Cheong, K., Sims, E., & Voon, J. W. K. 2007. Detecting hydrocarbon reservoirs from CSEM data in complex setting: Application to deepwater Sabah, Malaysia. *Geophysics*, **72**, WA97–WA103.

Derode, A., Larose, E., Campillo, M., & Fink, M. 2003. How to estimate the Green's function of a heterogeneous medium between two passive sensors? Application to acoustic waves. *Appl. Phys. Lett.*, **83**, 3054–3056.

Edwards, N. 2005. Marine Controlled Source Electromagnetics: Principles, Methodologies, Future Commercial Applications. *Surveys in Geophysics*, **26**(6), 675–700.

Ellingsrud, S., Eidesmo, T., Johansen, S., Sinha, M. C., MacGregor, L. M., & Constable, S. 2002. Remote sensing of hydrocarbon layers by seabed logging (SBL): results from a cruise offshore Angola. *The Leading Edge*, **21**(10), 972–982.

Fan, Y., & Snieder, R. 2009. Required source distribution for interferometry of waves and diffusive fields. *Geophys. J. Int.*, **179**, 1232–1244.

Fan, Y., Snieder, R., & Singer, J. 2009. 3-D Controlled Source Electromagnetic (CSEM) interferometry by multi-dimensional deconvolution. *SEG Expanded Abstracts*, **28**, 779.

Fan, Y., Snieder, R., Slob, E., Hunziker, J., & Singer, J. 2010a. Can diffusive fields be steered and focused? *Phys. Rev. Lett.*, in revision.

Fan, Y., Snieder, R., Slob, E., Hunziker, J., Singer, J., Sheiman, J., & Rosenquist, M. 2010b. Synthetic aperture controlled source electromagnetics. *Geophys. Res. Lett.*, **37**, L13305.

Filatov, V. V. 1984. Construction of focusing transformations of transient electromagnet fields. *Geologiya i Geofizika*, **25**, 85–89.

Gershenson, M. 1999. Time focusing of electromagnetic sounding in conductive media using similarities between wave and diffusion propagation. *in Heyman et al. ed. Ultra-Wideband Short-Pulse Electromagnetics 4*, 449–456.

Godin, O. A. 2006. Recovering the Acoustic Green's Function from Ambient Noise Cross Correlation in an Inhomogeneous Moving Medium. *Phys. Rev. Lett.*, **97**, 054301–4.

Grimbergen, J. L. T., Dessing, F. J., & Wapenaar, K. 1998. Modal expansion of one-way operators in laterally varying media. *Geophysics*, **63**, 995–1005.

Groenenboom, J., & Snieder, R. 1995. Attenuation, Dispersion and Anisotropy by Multiple Scattering of Transmitted Waves Through Distributions of Scatterers. *J. Acoust. Soc. Am.*, **98**, 3482–3492.

Helwig, S. L., Mogilatov, V. S., & Balashov, B. P. 2010. Enhanced sensitivity in land EM by using an unconventional source. *EGM 2010 International Workshop.*

Holten, T., y, E. G. Flekkø, Singer, B., Blixt, E. M., Hanssen, A., & Måløy, K. J. 2009. Vertical source, vertical receiver, electromagnetic technique for offshore hydrocarbon exploration. *First Break*, **27**, 89–93.

Hoversten, G. M., Newman, G. A., Geier, N., & Flanagan, G. 2006. 3D modeling of a deepwater EM exploration survey. *Geophysics*, **71**, G239–G248.

Hunziker, J., Slob, E., & Wapenaar, K. 2009. Controlled source electromagnetic interferometry by multidimensional deconvolution: spatial sampling aspects in sea bed logging. *71st EAGE Conference and Exhibition, Expanded Abstracts*, 278–285.

Hunziker, J., Fan, Y., Slob, E., Wapenaar, K., & Snieder, R. 2010. Solving Spatial Sampling Problems in 2D-CSEM Interferometry using Elongated Sources. *72st EAGE Conference and Exhibition, Expanded Abstracts*, 278–285.

Isaev, G. A., & Filatov, V. V. 1981. Physicomathematical principles of visualization of nonstationary electromagnetic fields. *Geologiya i Geofizika*, **22**, 89–95.

Ishimaru, A. 1997. *wave propagation and scattering in random media.* IEEE Press, Piscataway, NJ and Oxford University Press, NY.

Knuttel, A., Schmitt, J., Barnes, R., & Knutson, J. 1993. Acousto-optic scanning and interfering photon density waves for precise localization of an absorbing (or fluorescent) body in a turbid medium. *Rev. Sci. Instrum.*, **64**, 638–644.

Korobov, A. I., Izosimova, M. Y., & Toschov, S. A. 2010. Development of ultrasound focusing discrete array for air-coupled ultrasound generation. *Physics Procedia*, **3**, 201–207.

Koyama, T., Tamai, K., & Togashi, K. 2006. Current status of body MR imaging : fast MR imaging and diffusion-weighted imaging. *Int. J. Clin. Oncol.*, **11**, 278–285.

Kunetz, G. 1972. Processing and interpretation of magnetotelluric sounding. *Geophysics*, **37**, 1005–1021.

Kutasov, I. M., Eppelbaum, L. V., & Kagan, M. 2008. Interference well testing - variable fluid flow rate. *J. Geophys. Eng.*, **5**, 86–91.

Kwon, M. J., & Snieder, R. 2010. Uncertainty analysis for the integration of seismic and CSEM data. *Geophys. Prosp.*, In press.

Larose, E., Montaldo, G., Derode, A., & Campillo, M. 2006. Passive imaging of localized reflectors and interfaces in open media. *Appl. Phys. Lett.*, **88**, 104103.

Lee, K. H., Liu, G., & Morrison, H. F. 1989. A new approach to modeling the electromagnetic response of conductive media. *Geophysics*, **58**, 1180–1192.

Lien, M., & Mannseth, T. 2008. Sensitivity study of marine CSEM data for reservoir production monitoring. *Geophysics*, **73**, F151.

Liu, Wei, & Weiss, Stephan. 2009. Beam steering for wideband arrays. *Signal Processing*, **89**(5), 941–945.

Lobkis, O. I., & Weaver, R. L. 2001. On the emergence of the Green's function in the correlations of a diffuse field. *J. Acoust. Soc. Am.*, **110**, 3011–3017.

Lu, J., Zou, H., & Greenleaf, J. F. 1994. Biomedical ultrasound beam forming. *Ultrasound in Medicine & Biology*, **20**(5), 403–428.

Lu, M., Wan, M., Xu, F., Wang, X., & Chang, X. 2006. Design and experiment of 256-element ultrasound phased array for noninvasive focused ultrasound surgery. *Ultrasonics*, **44**, e325–e330.

MacGregor, L., & Sinha, M. 2000. Use of marine controlled-source electromagnetic sounding for sub-basalt exploration. *Geophysical Prospecting*, **48**(6), 1091–1106.

Malcolm, A. E., Scales, J. A., & van Tiggelen, B. A. 2004. Extracting the Green function from diffuse, equipartitioned waves. *Phys. Rev. E.*, **70**, 015601.

Mandelis, A. 1984. Frequency-domain photopyroelectric spectroscopy of condensed phases (PPES): A new, simple and powerful spectroscopic technique. *Chem. Phys. Lett.*, **108**, 388.

Mandelis, A. 2000. Diffusion Waves and their Uses. *Phys. Today*, **53**(8), 29.

Mandelis, A. 2001. *Diffusion-Wave Fields: Mathematical Methods and Green Functions.* 1 edn. New York: Springer.

Mehrer, H. 2007. *Diffusion in Solids - Fundamentals, Methods, Materials, Diffusion-Controlled Processes.* Springer Berlin Heidelberg New York.

Mehta, K., & Snieder, R. 2008. Acquisition geometry requirements for generating virtual-source data. *The Leading Edge*, **27**, 620–629.

Mehta, K., Bakulin, A., Sheiman, J., Calvert, R., & Snieder, R. 2007. Improving the virtual source method by wavefield separation. *Geophysics*, **72**, V79–V86.

Miyazawa, M., Snieder, R., & Venkataraman, A. 2008. Application of seismic interferometry to extract P and S wave propagation and observation of shear wave splitting from noise data at Cold Lake, Canada. *Geophysics*, **73**, D35–D40.

Mogilatov, V., & Balashov, B. 1996. A new method of geoelectrical prospecting by vertical electric current soundings. *Jornal of applied geophysics*, **36**, 31–41.

Mori, S., & Barkar, P. B. 1999. Diffusion magnetic resonance imaging: its principle and applications. *Anat. Rec.*, **257**, 102–109.

O'Leary, M. A., Boas, D. A., Chance, B., & Yodh, A. G. 1992. Refraction of diffuse photon density waves. *Phys. Rev. Lett.*, **69**, 2658–2662.

Ralston, T. S., Marks, D. L., Scott, Carney P., & Boppart, S. A. 2007. Interferometric synthetic aperture microscopy. *Nature Physics*, **3**, 129–134.

Rickett, J., & Claerbout, J. 1999. Acoustic daylight imaging via spectral factorization: Helioseismology and reservoir monitoring. *The Leading Edge*, **18**, 957–960.

Riyait, V. S., Lawlor, M. A., Adams, A. E., Hinton, O., & Sharif, B. 1995. Real-time synthetic aperture sonar imaging using a parallel architecture. *Image Processing, IEEE Transactions on*, **4**(7), 1010–1019.

Roux, P., Sabra, K. G., Kuperman, W. A., & Roux, A. 2005. Ambient noise cross correlation in free space: Theoretical approach. *J. Acoust. Soc. Am.*, **117**, 79–84.

Sabra, K. G., Gerstoft, P., Roux, P., Kuperman, W. A., & Fehler, M. C. 2005a. Extracting time-domain Green's function estimates from ambient seismic noise. *Geophys. Res. Lett.*, **32**, L03310.

Sabra, K. G., Gerstoft, P., Roux, P., Kuperman, W. A., & Fehler, M. C. 2005b. Surface wave tomography from microseisms in Southern California. *Geophys. Res. Lett.*, **32**, L14311.

Sánchez-Sesma, F. J., & Campillo, M. 2006. Retrieval of the Green's funciton from cross correlation: The canonical elastic problem. *Bull. Seismol. Soc. Am.*, **96**, 1182–1191.

Sánchez-Sesma, F. J., Pérez-Ruiz, J. A., Campillo, M., & Luzón, F. 2006. Elastodynamic 2D Green function retrieval from cross-correlation: Canonical inclusion problem. *Geophys. Res. Lett.*, **33**, L13305.

Schmitt, J. M., Knuttel, A., & Knutson, J. R. 1992. Interference of diffusive light waves. *J. Opt. Soc. Am.*, **9**(10), 1832–1843.

Schmitt, J. M., Knuttel, A., & Bonner, R. F. 1993. Measurement of optical properties of biological tissues by low-coherence reflectometry. *Appl. Opt.*, **32**(30), 6032–6042.

Scholl, C., & Edwards, R. N. 2007. Marine downhole to seafloor dipole-dipole electromagnetic methods and the resolution of resistive targets. *Geophysics*, **72**, WA39–WA49.

Schuster, G. T., Yu, J., Sheng, J., & Rickett, J. 2004. Interferometric/daylight seismic imaging. *Geophys. J. Int.*, **157**, 838–852.

Shapiro, N. M., Campillo, M., Stehly, L., & Ritzwoller, M. H. 2005. High-Resolution Surface-Wave Tomography from Ambient Seismic Noise. *Science*, **307**, 1615–1618.

Sheng, P. 1990. *Scattering and Localization of Classical Waves in Random Media.* World Scientific, Singapore.

Slob, E., Draganov, D., & Wapenaar, K. 2007. Interferometric electromagnetic Green's functions representations using propagation invariants. *Geophys. J. Int.*, **169**, 60–80.

Snieder, R. 2004. Extracting the Green's function from the correlation of coda waves: A derivation based on stationary phase. *Phys. Rev. E*, **69**, 046610.

Snieder, R. 2006a. *A Guided Tour of Mathematical Methods For the Physical Sciences.* 2 edn. Cambridge University Press.

Snieder, R. 2006b. Retrieving the Green's function of the diffusion equation from the response to a random forcing. *Phys. Rev. E*, **74**, 046620.

Snieder, R. 2007. Extracting the Green's function of attenuating heterogeneous acoustic media from uncorrelated waves. *J. Acoust. Soc. Am.*, **121**, 2537–2643.

Snieder, R., & Şafak, E. 2006. Extracting the Building Response Using Seismic Interferometry: Theory and Application to the Millikan Library in Pasadena, California. *Bull. Seismol. Soc. Am.*, **96**, 586–598.

Snieder, R., Sheiman, J., & Calvert, R. 2006. Equivalence of the virtual-source method and wave-field deconvolution in seismic interferometry. *Phys. Rev. E*, **73**, 066620.

Snieder, R., Wapenaar, K., & Wegler, U. 2007. Unified Green's function retrieval by cross-correlation; connection with energy principles. *Phys. Rev. E.*, **75**, 036103.

Snieder, R., Miyazawa, M., Slob, E., Vasconcelos, I., & Wapenaar, K. 2009. A comparison of strategies for seismic interferometry. *Surveys in Geophysics*, **30**, 503–523.

Song, Tai K., & Park, Song B. 1990. A new digital phased array system for dynamic focusing and steering with reduced sampling rate. *Ultrasonic Imaging*, **12**, 1–16.

Srnka, Leonard J., & Carazzone, James J. 2003. Method of imaging subsurface formations using a virtual source array. *United States Patent Application Publication*, No: US 2003/0050759 A1.

Stehly, L., Campillo, M., & Shapiro, N. M. 2006. A study of seismic noise from its long-range correlation properties. *J. Geophys. Res.*, **111**, B10306.

van Manen, D., Robertsson, J. O. A., & Curtis, A. 2005. Modeling of Wave Propagation in Inhomogeneous Media. *Phys. Rev. Lett.*, **94**, 164301.

van Wijk, K. 2006. On estimating the impulse response between receivers in a controlled ultrasonic experiment. *Geophysics*, **71**, SI79–SI84.

Vasconcelos, I., & Snieder, R. 2008a. Interferometry by deconvolution, Part 1 - Theory for acoustic waves and numerical examples. *Geophysics*, **73**, S115–S128.

Vasconcelos, I., & Snieder, R. 2008b. Interferometry by deconvolution, Part 2 - elastic waves and application to drill-bit seismic imaging. *Geophysics*, **73**, S129–S141.

Vasconcelos, I., Snieder, R., & Hornby, B. 2007. Target-oriented interferometry — Imaging with internal multiples from subsalt VSP data. *SEG Technical Program Expanded Abstracts*, **26**, 3069–3073.

Wang, C., & Mandelis, A. 1999. Purely thermal-wave photopyroelectric interferometry. *J. Appl. Phys.*, **85**(12), 8366–8377.

Wang, W., Cai, J., & Peng, Q. 2009. Conceptual design of near-space synthetic aperture radar for high-resolution and wide-swath imagingstar. *Aerospace Science and Technology*, **13**, 340–347.

Wapenaar, K. 2004. Retrieving the Elastodynamic Green's Function of an Arbitrary Inhomogeneous Medium by Cross Correlation. *Phys. Rev. Lett.*, **93**, 254301–4.

Wapenaar, K. 2006a. Green's function retrieval by cross-correlation in case of one-sided illumination. *Geophys. Res. Lett.*, **33**, L19304.

Wapenaar, K. 2006b. Non-reciprocal Green's function retrieval by cross correlation. *J. Acoust. Soc. Am.*, **120**, EL7–EL13.

Wapenaar, K., Fokkema, J., & Snieder, R. 2005. Retrieving the Green's function in an open system by cross-correlation : a comparison of approaches. *J. Acoustic. Soc. Am.*, **118**, 2783–2786.

Wapenaar, K., Slob, E., & Snieder, R. 2006. Unified Green's Function Retrieval by Cross Correlation. *Phys. Rev. Lett.*, **97**, 234301.

Wapenaar, K., Slob, E., & Snieder, R. 2008. Seismic and electromagnetic controlled-source interferometry in dissipative media. *Geophys. Prosp.*, **56**, 419–434.

Ward, S. H., & Hohmann, G. W. 1987. Electromagnetic theory for geophysical applications. *in Misac N. Nabighian ed. Electromagnetic Methods in Applied Geophysics*, 131–167.

Weaver, R. L. 2005. Information from seismic noise. *Science*, **307**, 1568–1569.

Weaver, R. L. 2008. Ward identities and the retrieval of Green's functions in the correlations of a diffuse field. *Wave Motion*, **45**, 596–604.

Weaver, R. L., & Lobkis, O. I. 2001. Ultrasonics without a Source: Thermal Fluctuation Correlations at MHz Frequencies. *Phys. Rev. Lett.*, **87**, 134301.

Weaver, R. L., & Lobkis, O. I. 2004. Diffuse fields in open systems and the emergence of the Green's function. *J. Acoust. Soc. Am.*, **116**, 2731–2734.

Weaver, R. L., & Lobkis, O. I. 2005. Fluctuations in diffuse field–field correlations and the emergence of the Green's function in open systems. *J. Acoust. Soc. Am.*, **117**, 3432–3439.

Wooh, S., & Shi, Y. 1998. Influence of phased array element size on beam steering behavior. *Ultrasonics*, **36**(6), 737–749.

Wooh, S., & Shi, Y. 1999. Optimum beam steering of linear phased arrays. *Wave Motion*, **29**(3), 245–265.

Yodh, A., & Chance, B. 1995. Spectroscopy and imaging with diffusing light. *Phys. Today*, **48**, 34–40.

Zhdanov, M. S., & Traynin, P. 1997. Migration versus inversion in electromagnetic imaging technique. *Journal of Geomagnetism and Geoelectricity*, **49**, 1415–1437.

Zhdanov, M. S., Traynin, P., & Portniaguine, O. 1995. Resistivity imaging by time domain electromagnetic migration (TDEMM). *Exploration Geophysics*, **25**, 186–194.

Zhdanov, M. S., Traynin, P., & Booker, J. R. 1996. Underground imaging by frequency domain electromagnetic migration. *Geophysics*, **61**, 666–682.

Zhou, X., Chang, N., & Li, S. 2009. Applications of SAR Interferometry in Earth and Environmental Science Research. *Sensors*, **9**(3), 1876–1912.